AN EXPERIMENTAL STUDY
OF A
TURBULENT VORTEX RING

Thesis by

Ari Glezer

In Partial Fulfillment of the Requirements
for the Degree of
Doctor of Philosophy

California Institute of Technology
Pasadena, California

1981
(Submitted May 29, 1981)

This work is dedicated to my parents,

Sara and Shlomo Glezer

I am greatly indebted to Professors Donald Coles and Hans W. Liepmann for a lighthouse that never went dark as I sailed through troubled times.

ACKNOWLEDGMENT

The research described in this thesis was supported by the National Science Foundation under Grants ENG 75-03694 and ENG 77-23541. During the period from September 1975 to September 1976 the author was the recipient of a Tel-Aviv University Fellowship.

ABSTRACT

An apparatus has been constructed to study the formation and dynamics of vortex rings. The rings are formed in water by a momentary jet discharge downward into a glass tank from an orifice in a submerged plate. The necessary impulse is provided by a pressurized reservoir and is controlled by a fast programmable solenoid valve.

A particular turbulent vortex ring with a relatively thin core was chosen for detailed study. The velocity field of this ring was measured at numerous locations in the tank, using a two-channel laser-Doppler velocimeter with digital tracking electronics. Beam-splitting and frequency-shifting were accomplished by two partially-overlapping radial phase gratings driven by hysteresis-synchronous motors.

The main aim of the research was to verify the similarity properties of the turbulent vortex ring and to determine mean particle paths and mean vorticity contours in the appropriate non-steady similarity coordinates $x/t^{\frac{1}{4}}$, $r/t^{\frac{1}{4}}$. Some novel pattern-recognition techniques were developed to overcome the problem of dispersion in the trajectories of individual vortices.

TABLE OF CONTENTS

Table of Contents cont'd.

I. INTRODUCTION

This thesis is a contribution to the literature of coherent structure in turbulent flow. The structure chosen for experimental study, the turbulent vortex ring, has an extensive but not very instructive literature. No previous investigation has fully exploited the concept of similarity, nor have experimental data been obtained to resolve important structural questions about entrainment and turbulence production. In a recent survey of available information about six different kinds of coherent structure -- the puff in a pipe, the spot in a boundary layer, the spiral turbulence, the vortex ring, the mixing layer, the vortex street -- Coles (1981) identified the vortex ring as a structure badly in need of study by contemporary experimental methods.

A large part of the literature on vortex rings deals with laminar rings, with emphasis on the formation process and on an elegant instability in which azimuthal waves can appear on a thin vortex core. There is also a body of work on interactions between laminar vortex rings. These interactions range from leap-frogging to processes involving fusion, fission, and other phenomena best described as collisions. Another large part of the literature deals with effects of buoyant forces. A thermal, whose momentum is continuously changing, is not the same structure as a vortex ring, whose momentum is generated impulsively. Nevertheless, these motions are often treated together, and the concept of similarity is in fact further advanced for buoyant flows. Finally, a part of the literature deals with effects of modulation on jet flow, ranging from control of coalescence in mixing layers at one extreme to slow pulsations leading to large-scale vorticity concentrations resembling vortex rings at the other. All of these phenomena lie outside the scope of the present research.

A vortex ring can be defined as an approximately spheroidal volume of fluid having internal azimuthal vorticity. The streamlines of the internal flow can be thought of as closed curves to the same degree that the flow can be thought of as steady in a translating coordinate system. The azimuthal vorticity (better, the ratio vorticity/radius) may be more or less uniformly distributed, in which case the structure is sometimes called a puff (the use of this term for two different structures is unfortunate, but probably immutable), or the vorticity may be concentrated in a thin toroidal core, in which case the term vortex ring is more accurate. The distinction is not important for many purposes, including the discussion of similarity in Sections II and VI of this paper. However, the presence of distributed mean vorticity in a turbulent puff is usually associated in experimental work with use of a screen or grid at the exit of the generating device, and in numerical work with use of an eddy viscosity of the conventional kind. The resulting structure may be a turbulent vortex ring according to the definition just given, but it also lies generally outside the scope of the present research.

As a practical experimental matter, the only instrument capable of resolving the motion in a turbulent vortex ring is the laser-Doppler velocimeter with frequency bias. Such an instrument was not available at the beginning of the work, and had to be designed and constructed as part of the research. The functions of beam-splitting and frequency shifting were combined in a single component, a rotating radial grating. This technique is not new. However, a substantial new element in the present design is the use of two overlapping radial gratings to produce a two-channel system in which channel separation is accomplished by electronic filtering of the signal from a single detector. Other contributions include the design of a tracking processor based on a digital phase-lock-loop circuit, and the development of methods for removing optical noise generated by imperfections in the gratings, thereby improving the signal-to-noise ratio. The design of this velocimeter is described in Section IV .

Vortex rings are almost invariably formed by a brief discharge of fluid from an orifice. In previous work, the geometry of the various vortex generators has tended to vary arbitrarily from one experiment to another, with important consequences for certain parameters of the motion. In the present research, as reported in Section III, some time was spent in devising and demonstrating the value of a particularly simple piston-cylinder geometry. The geometry in question is different from previous geometries, but may eventually be attractive as a standard.

Even given an efficient vortex-ring generator, accurate instrumentation, and adequate means for collecting, recording, and processing data, a formidable obstacle to successful experimental study of the turbulent vortex ring is dispersion in the path followed by successive rings from the generating device to the point of observation. Any description of the flow in terms of ensemble-averaged quantities is likely to lack resolution and to misrepresent the physical processes actually involved. Elaborate and novel methods therefore had to be developed to overcome the problem of dispersion, as described in Section VII.

The object of the research from the beginning was to determine mean particle paths, and eventually entrainment, by exploiting the fact that the property of similarity reduces the Lagrangian particle-path equations to an autonomous system. These particle-path equations are integrated graphically in Section VIII. The spirit of the analysis, and some of the procedure, follow the precedents set by Woodward (1959) for the thermal, by Turner (1964) for a model problem involving the Hill spherical vortex, and by Cantwell, Coles, and Dimotakis (1978) for the turbulent spot in a laminar boundary layer. The topological structure of the turbulent vortex ring in similarity variables is found to consist of two axially-symmetric saddle points at the front and rear of the structure, with turbulence production concentrated at the rear, and a ring focus representing transport of turbulent energy toward the highly rotational core of the vortex ring.

II. PRODUCTION OF TURBULENT VORTEX RINGS

2.1 Dimensional Arguments and Similarity

The sketch depicts an axially-symmetric vortex ring and defines some of the notation. The coordinates are (x, r, θ) and the corresponding mean velocity components are (u, v, w). The quantity I is the initial impulse, or increment of momentum, and is a constant for a given vortex. The quantity c is the celerity and is a function of position. Both of these quantities play an important role in what follows.

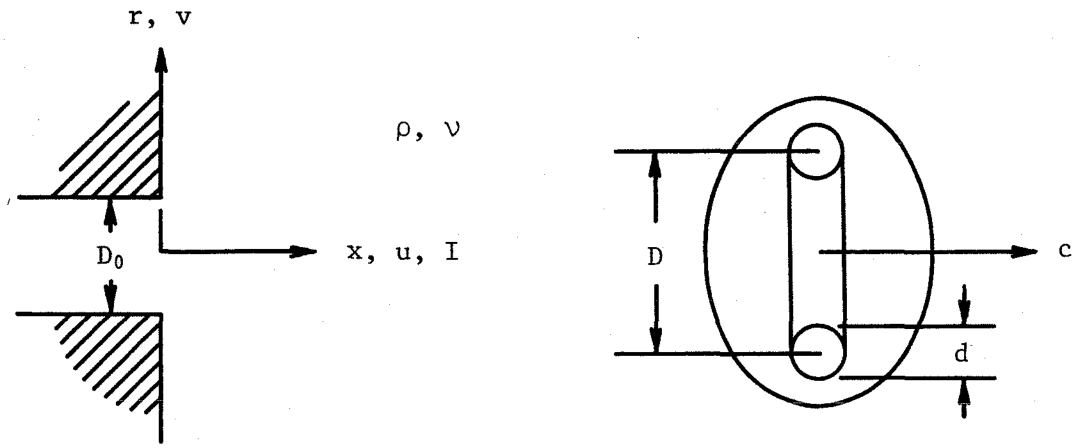

Let the mean motion in such a ring be described in the usual way with the aid of a stream function,

$$u = \frac{1}{r}\frac{\partial\psi}{\partial r}, \qquad v = -\frac{1}{r}\frac{\partial\psi}{\partial x} \tag{1}$$

where the statement

$$\psi = \psi(x, r, t) \tag{2}$$

means no more than "ψ depends on x, r, and t." The explicit form of the dependence does not need to be known in order to discuss the question of similarity.

Provided that the parameters of the problem define characteristic global scales M, L, and T for mass, length and time, Eq. (2) can be converted immediately to dimensionless form;

$$\frac{\psi T}{L^3} = f\left(\frac{x}{L}, \frac{r}{L}, \frac{t}{T}\right) \tag{3}$$

That this conversion is possible for the vortex ring is clear on considering the dimensions of three of the parameters in the sketch; namely, I, ρ, and ν;

$$[I] = \frac{ML}{T}, \quad [\rho] = \frac{M}{L^3}, \quad [\nu] = \frac{L^2}{T} \tag{4}$$

When these expressions are interpreted as simultaneous algebraic equations defining M, L, and T, they imply

$$M = \rho\left(\frac{I}{\rho\nu}\right)^{3/2}, \quad L = \left(\frac{I}{\rho\nu}\right)^{\frac{1}{2}}, \quad T = \frac{I}{\rho\nu^2} \tag{5}$$

According to the sketch, the problem contains at least one additional length scale, the orifice diameter D_0. The ratio of the two length scales defines an important dimensionless parameter,

$$J = \frac{I}{\rho\nu A} \tag{6}$$

where

$$A = \frac{\pi}{4} D_0{}^2 \tag{7}$$

is the area of the orifice. <u>This parameter J will be interpreted here mainly as a Reynolds number whose chief function is to allow various vortex-ring flows to be ordered according to their strength</u>.

When L and T are defined by Eqs. (5), the dimensionless form of the stream function (3) becomes

$$\psi\left(\frac{\rho}{I\nu}\right)^{\frac{1}{2}} = f\left\{x\left(\frac{\rho\nu}{I}\right)^{\frac{1}{2}},\ r\left(\frac{\rho\nu}{I}\right)^{\frac{1}{2}},\ \frac{t\rho\nu^2}{I}\ ;\ J\right\} \tag{8}$$

in which the ordering parameter J is displayed along with the three arguments of the function f.

If the flow is laminar, Eq. (8) is apparently the end of the road as far as a similarity formulation is concerned, even when the flow is assumed not to depend on the length D_0. All three independent variables are required to describe the motion. This property may be weakened when the flow is turbulent, because it may then be permissible, at least in some local region, to neglect the dependence of the flow on the viscosity ν. Thus choose any two of the dimensionless independent variables, say $x(\rho\nu/I)^{\frac{1}{2}}$ and $r(\rho\nu/I)^{\frac{1}{2}}$. Multiply these, and $\psi(\rho/I\nu)^{\frac{1}{2}}$, by appropriate powers of the third variable, say $t\rho\nu^2/I$, so as to eliminate the viscosity. Whatever variables are chosen, the result is always of the form*

$$\psi t^{\frac{1}{4}}\left(\frac{\rho}{I}\right)^{3/4} = g\left\{x\left(\frac{\rho}{tI}\right)^{\frac{1}{4}},\ r\left(\frac{\rho}{tI}\right)^{\frac{1}{4}};\ J\right\} \tag{9}$$

Hence the number of dimensionless independent variables is reduced from three to two by the requirement that neither ν nor D_0 should appear in the formulation (except in the ordering parameter J, where both

---

*The same form is obtained if the characteristic scale L is taken originally to be D_0 rather than $(I/\rho\nu)^{\frac{1}{2}}$, and D_0 is then eliminated rather than ν.

appear). Such a reduction is of the essence of a successful similarity argument.

The non-steady similarity formulation (9) for the turbulent vortex ring has been invented and re-invented several times. Contributions by Turner (1957), Grigg and Stewart (1963), Richards (1965), Johnson (1970), and Maxworthy (1974) all argue from an elementary application of the principle of conservation of momentum. The papers by Grigg and Stewart and by Richards, in particular, concentrate on the turbulent thermal; i.e., on a structure driven by buoyant forces. Such structures are characterized by very strong mixing and by alternative similarity laws which involve the initial buoyant force as main parameter rather than the initial impulse. The associated impulsively driven structure is the puff (see the Introduction). In more recent papers the emphasis has remained on the puff, but the arguments have shifted to similarity considerations for the non-steady Reynolds equations with time-dependent eddy viscosity. A paper by Lugovtsov (1970), for example, is cited by Kaplanskii and Epshtein (1976), who carried out numerical calculations for both puffs and thermals. A similar approach was taken by Kovasznay and Lee (1974) in a discussion of fundamental solutions of the Stokes approximation to the Reynolds equations. A recent paper by Cantwell (1979) uses an abbreviated form of the present argument. Several of these authors have pointed out that the turbulent vortex ring is not only self-similar but also conical, in the sense that x and r have the same dependence on t.

2.2 Generation Conditions

Photographs of real laminar and turbulent vortex rings from the present experiments are shown in Fig. 1. There is no question that the two states are profoundly different. It is therefore remarkable that the literature of the subject contains no useful discussion of the conditions which determine whether a given vortex-ring generator will produce a laminar ring or a turbulent one, or perhaps a laminar ring which undergoes instability and transition to turbulence within the range of observation.

The experimental evidence suggests that it is necessary to assign some degree of structure to the parameter J by looking at details of the generation process. This process has so far been represented only in the abstract; i.e., by the impulse I and by the area A (or the diameter D_0). Several levels of structure, and several additional parameters, may be required if it is desired to take into account the geometry of a particular apparatus and the use of a particular method to set the fluid into motion.

In a real experiment, the vortex ring is invariably formed by a programmed discharge of fluid over some short but finite time interval. The most elementary representation of this process is a uniform cylindrical-slug model, in which a cylindrical volume of fluid moves at constant velocity U_0 for a time T_0 through a circular orifice of diameter D_0. The slug length L_0 is evidently the product U_0T_0.

In practice, this uniform cylindrical-slug model will not suffice, partly because of effects of geometry and partly for other reasons. In experiments by Sallet and Widmayer (1974) and by Didden (1977), for example, the exit velocity U_0 was not constant, but varied with time according to some specified program. In such cases a mean velocity (with respect to time) can first be defined as

$$\overline{U}_0 = \frac{1}{T_0}\int_0^{T_0} U_0(t)dt \tag{10}$$

where $U_0(t)$ is assumed for the present to be uniform over the orifice area. The equivalent slug length is now

$$L_0 = \int_0^{T_0} U_0(t)dt = \overline{U}_0 T_0 \tag{11}$$

and the impulse (the momentum associated with the discharge) is

$$I = \rho A \int_0^{T_0} U_0{}^2(t)dt = \rho A\, \overline{U_0{}^2}\, T_0 \tag{12}$$

To ease the notation, define a velocity-program factor P as

$$P = \int_0^1 \left(\frac{U_0}{\overline{U}_0}\right)^2 d\,\frac{t}{T_0} = \frac{\overline{U_0{}^2}}{\overline{U}_0{}^2} \tag{13}$$

whereupon (12) can be written

$$I = \rho AP\overline{U}_0{}^2 T_0 = \rho AP\overline{U}_0 L_0 = \rho AP\,\frac{L_0{}^2}{T_0} \tag{14}$$

The ordering parameter J defined by Eq. (6) thus emerges as a particular Reynolds number,

$$J = P\,\frac{\overline{U}_0 L_0}{\nu} \tag{15}$$

To recapitulate: at a structural approximation which takes into account variations of U_0 with time but ignores variations of U_0 over the orifice cross section, two new dimensionless parameters (other than J) are necessary to describe the generation process. Recall from Eq. (6) that the dimensional quantities which enter into J are ρ, ν, I, and D_0. The new dimensional quantities introduced by the non-uniform slug model are $\overline{U}_0$, L_0, and T_0. However, Eqs. (11) and (14) provide two constraints on these three new quantities, so that only one, say L_0, can be specified independently when ρ, ν, I, D_0, and P are given. The dimensionless parameters of the generation process to this approximation are therefore J, P, and L_0/D_0.

To illustrate the point, the characteristic mass, length, and time defined by Eqs. (5) can be made dimensionless with the corresponding slug quantities and written as

$$\frac{M}{\rho A L_0} = J^{3/2}\left(\frac{\sqrt{\pi}}{2}\;\frac{D_0}{L_0}\right), \quad \frac{L}{L_0} = J^{\frac{1}{2}}\left(\frac{\sqrt{\pi}}{2}\;\frac{D_0}{L_0}\right), \quad \frac{T}{T_0} = \frac{J^2}{P}\left(\frac{\sqrt{\pi}}{2}\;\frac{D_0}{L_0}\right)^2 \qquad (16)$$

2.3 Circulation

A derived quantity which is important for vortex dynamics is the initial circulation Γ_0 (in a half-plane through the axis of symmetry) associated with the generation process. In this plane the rate of vorticity flux from the edge of the orifice has the magnitude

$U_0^2/2$*, so that

$$\Gamma_0 = \int_0^{T_0} \frac{U_0^2(t)}{2} dt = \frac{\overline{U_0^2} T_0}{2} \tag{17}$$

or, in view of Eq. (11),

$$\Gamma_0 = P \frac{\overline{U}_0^2 T_0}{2} = P \frac{\overline{U}_0 L_0}{2} = P \frac{L_0^2}{2T_0} \tag{18}$$

Comparison with Eq. (15) then gives

$$J = 2 \frac{\Gamma_0}{\nu} \tag{19}$$

It is inherent in the definitions (10) and (13) that $P \geq 1$. For given values of $\overline{U}_0$ and T_0 (or $\overline{U}_0$ and L_0, or L_0 and T_0), therefore, _any departure from a constant-velocity program acts to increase the circulation and the momentum of a vortex ring_. This conclusion was first stated (implicitly) in a valuable contribution by Didden (1977) who generated laminar rings having identical values for D_0, $\overline{U}_0$, L_0, and T_0, but having different velocity programs (square wave, ramp, haversine). Didden also listed the corresponding program factors P; these are 1, 4/3, 3/2, respectively. Didden's data for $L_0/D_0 = 1.4$ from his Fig. 16 are reproduced in non-dimensional form in Fig. 2(a). The circulation Γ was inferred from LDV

---

*Use a boundary-layer approximation to evaluate the flux of vorticity across the plane of the orifice; thus, neglecting signs,

$$\frac{d}{dt}\int \vec{\Omega}\, dV \cdot \vec{i}_\theta = \int (\vec{\Omega} \cdot \vec{i}_\theta)(\vec{u} \cdot \vec{n}) dA = \int \frac{\partial u}{\partial r} u\, dr = \int \frac{\partial (u^2/2)}{\partial r} dr .$$

measurements of velocity on the axis of symmetry at a single station located three diameters from the orifice. This circulation (for fixed D_0, L_0, and ν, and for a given velocity program) is proportional to $\overline{U}_0$, as expected. In Fig. 2(b) the same data are replotted according to Eq. (18) and are brought nearly into coincidence.

The effect on circulation of changing L_0, other things being equal, was recorded by Didden in his Fig. 18, and these measurements are also included in Fig. 2(b). The data for the longest stroke, $L_0/D_0 = 2.2$, are perhaps consistent with the data for $L_0/D_0 = 1.4$, but the data for the shortest stroke, $L_0/D_0 = 0.6$, are not. These discrepancies were accounted for by LDV measurements reported by Didden in a second paper (1979). In all of his experiments, the vortex rings were formed at the free end of a round pipe, with all other walls well removed. Didden found two opposing effects which were both important at small times. First, the flux of vorticity into the nascent vortex ring was initially larger than expected because the emerging fluid turned sharply outward near the corner. The local velocity at the edge of the internal boundary layer was therefore increased substantially above the piston velocity U_0. Second, vorticity of opposite sign was generated in the boundary layer formed on the outer pipe wall through the influence of the induced velocity field of the growing vortex. The first effect dominated over the second one. Didden also measured a third and relatively small effect which increased the vorticity flux at large rather than small times. Because of the growing displacement thickness of the internal boundary layers, the fluid velocity over the central part of the cavity flow eventually became significantly larger than the piston velocity.

At least for large Reynolds numbers, it should be possible to make a net estimate of the first two effects by taking $d\Gamma/dt$ as the difference in $u^2/2$ across the two boundary layers, which is to say as the discontinuity in $u^2/2$ for the corresponding inviscid flow. It seems likely that both effects would be reduced, especially the second one, if the vortex ring were generated at an orifice formed by the intersection of a cylindrical cavity with a plane wall (as in the present experiments) rather than at the end of a cylindrical pipe. On the other hand, the first effect would undoubtedly be increased if the vortex were formed at a circular hole in a thin plane wall. All of these geometries have been used by various experimenters.

Didden's results in his first paper also establish that his two ramp programs, although oppositely skewed, produced vortices having identical circulations for identical values of $\overline{U}_0$. The vortices do have slightly different diameters and celerities, according to Didden's Table 1. Thus some aspects of vortex behavior must depend not only on J, P, and L_0/D_0, as argued here, but also on higher moments of the vorticity-generating function $U_0^{\,2}(t)$. Nevertheless, at least for these laminar experiments, <u>the circulation at the end of the rollup process is determined for practical purposes by the total</u>

vorticity flux, regardless of the distribution of this vorticity flux over time. This remarkable result holds despite the fact that the measured circulation Γ in Fig. 2(b) is typically 30 to 40 percent larger than Γ_0 from Eq. (11), for reasons already set forth.

2.4 A Tentative Transition Map

It has already been argued that, for given P, the two parameters $\Gamma_0/\nu \sim J$ and L_0/D_0 might under some conditions be sufficient to define the behavior of a particular vortex ring, not only during its formation but throughout its lifetime. As part of the present experiments, a limited flow-visualization survey was carried out to test this conjecture. The piston apparatus described in Section 3.3 below was used, for the sake of its simple geometry. Two primitive parameters, the piston stroke L_0 and the (constant) piston velocity U_0, were varied systematically for two orifice diameters, $D_0 = 1.90$ cm (3/4 inch) and $D_0 = 2.54$ cm (1 inch). The piston stroke was varied by changing the piston length, the sum length plus stroke being fixed. The piston velocity was varied by changing the pressure in the reservoir shown in Fig. 6(b) below. The main dependent variable of the experiments was the valve opening time T_0, which was carefully adjusted in each case until the piston stopped in the flush position.

A guide in organizing the survey was the fact that a large pressure drop occurs across the valve in the vortex generator. If the flow through the valve passage is turbulent and the pressure drop is large enough so that the flow rate is nearly independent of exit pressure, this pressure drop p should be a rough measure of the square of the local velocity V through the valve; $p \sim V^2$. Continuity requires $U_0 D_0{}^2 \sim VA'$, where A' is the area of the valve passage. Hence

$$p \sim U_0{}^2 D_0{}^4 \qquad (20)$$

When this relationship is used to eliminate the velocity U_0 in favor of p in the definitions (11) and (18) given earlier, the qualitative estimates are obtained

$$\frac{\Gamma_0}{\nu} \sim \frac{T_0 p}{D_0{}^4} \ , \qquad \frac{L_0}{D_0} \sim \frac{T_0 p^{\frac{1}{2}}}{D_0{}^3} \qquad (21)$$

To maintain constant values for Γ_0/ν and L_0/D_0, therefore, both the reservoir pressure and the valve opening time should vary approximately like $D_0{}^2$. These estimates were very useful for planning purposes.

The results of the survey are shown in dimensional form for the two orifice diameters in Figs. 3(a) and 3(b). The abscissa is the reservoir pressure; the ordinate is the opening time for the valve. The crosses represent conditions under which vortex rings remained laminar for at least part of the available range of observation in the tank (about 30 to 40 diameters). The filled circles represent vortices which became turbulent essentially as soon as they were formed. For a particular piston, and thus a particular L_0/D_0, the data paths for the higher pressures and longer strokes agree well with the relation $T_0 \sim p^{-\frac{1}{2}}$ implied by the second of Eqs. (21).

The same data are shown in dimensionless form in Fig. 4. Measured values of the parameters L_0 and T_0 were used, together with the condition $P = 1$, in calculating Γ_0/ν from Eq. (18). There is a reasonably well-defined boundary separating vortex rings which are turbulent when formed from rings which are not, although this boundary does not seem to correspond to any simple relation between the parameters Γ_0/ν and L_0/D_0.

On the supposition that Fig. 4 may be a useful first approximation to a transition map for vortex rings, the experiments of some other investigators have been located on the same map in Fig. 5. Various vortex-ring generators were used, and it is not always possible to recover the parameters of the non-uniform slug model from the published data. Even when this is possible, there is no assurance that the criterion applied in the case of the present data (turbulence essentially from the beginning of the motion) is always relevant. Nevertheless, the transition line in the figure is consistent with the experience of other investigators, particularly Sallet and Widmayer (1974). The puff has to be viewed as an exceptional flow, very susceptible to turbulence. One remaining anomaly is that there was no difficulty during the present experiments in producing single laminar vortex rings over the range $0.3 < L_0/D_0 < 6.2$. Working with another geometry but in the same range of Γ_0/ν, Didden (1977) and Liess (1978) found that their apparatus formed multiple rings for $L_0/D_0 > 2.4$. The role of geometry therefore needs more study.

III. EXPERIMENTAL APPARATUS

The experiments were carried out in water contained in a glass tank one meter on a side. Vortex rings were generated at a circular orifice in a ceiling plate suspended just below the free water surface, as indicated schematically in Fig. 6(a). The rings moved vertically downward in the tank. The flow could be illuminated and viewed from the four sides but not from the top or bottom.

3.1 The Pressurized Reservoir

Although two quite different vortex generators were used during the experiments, the impulse necessary to produce the vortex rings came in both cases from a momentary discharge of water from the pressurized reservoir shown above the tank in Fig. 6(a). The flow out of the reservoir was controlled by a fast annular-outlet solenoid valve (Moog model 53-123A)* energized by a solid-state relay. This valve could open or close in an interval as short as 6 msec. The stainless-steel reservoir, 15 cm (6 inches) in diameter by 61 cm (24 inches) long, could be pressurized by nitrogen up to 2100 kPa (300 psi). Water in the reservoir was normally replenished without relieving the pressure by using a hand pump (VSL Corporation model 100-9 S S). The water-supply line was fitted with a 50 μm filter. When the reservoir was vented to atmosphere, water could also be replenished from a reserve supply in a separate tank pressurized to about 100 kPa (15 psi).

---

*Two of these valves were obtained through the courtesy of Dr. Raymond Goldstein of the Jet Propulsion Laboratory.

The water level in the pressurized reservoir was monitored by a sonic level gauge developed for this purpose. This gauge was a circular piezoelectric transducer (resonant frequency 1.9 MHz) coated to match the acoustical impedance of the surrounding water. The transducer was pulsed at 1 kHz. The reflected acoustical wave from the water surface was received by the same device. An electronic circuit measured the elapsed time, which was linearly proportional to the depth.

The reservoir pressure was held constant by a pressure regulator (Veriflo model 1R502B580) selected for fast response at low flow rates. A needle valve on the low-pressure side of the regulator vented a small amount of nitrogen continuously to atmosphere, thus avoiding complete shutoff and shortening the response time of the pressure-regulating system. An accumulator connected to the upper end of the reservoir prevented pressure drop in excess of about 7 kPa (1 psi) during discharge.

3.2 The First Vortex Generator

In the original vortex generator, water moved directly from the pressurized reservoir through the valve, through a calming section fitted with baffles, through a converging nozzle, and into the tank, as indicated in Fig. 6(a). The baffles were made of teflon-coated open-pore aluminum foam (Duocel, manufactured by Energy Research and Generation Inc.).

The command circuitry for the solenoid valve could provide a single pulse of a specified duration (triggered either manually or by an auxiliary TTL signal), or a continuous pulse train at a specified duty cycle and frequency, or a burst of a preset number of such pulses (up to 16), or a continuous string of such bursts with a specified repetition rate. The frequency of vortex-ring production was limited only by the time constant of the fast solenoid valve. Under most conditions, the total volume of fluid leaving the nozzle was small compared to the volume of the calming section. Two nozzles were provided, with orifice diameters of 1.90 cm (3/4 inch) and 2.54 cm (1 inch). The jet velocity at maximum reservoir pressure could reach 1.5 m/sec.

The apparatus just described was particularly useful for visual study of interactions of multiple vortex rings. It was in fact used for this purpose, although the results are not reported here because of their highly qualitative nature. Flow visualization was aided by the fact that dye could be added directly to the water in the pressurized reservoir. For quantitative work with laser-Doppler instrumentation, however, it was a disadvantage that the reservoir fluid had to be seeded with particles to match the seeding density in the tank (with suitable precautions taken against particle settling in the pressurized reservoir) and that these particles had to pass through the fast solenoid valve. A more important disadvantage in practice was the sporadic appearance of small bubbles in the water below the valve. The source of these bubbles was dissolved air and/or high-pressure nitrogen coming out of solution when the local pressure decreased abruptly during flow through the valve. These bubbles tended to accumulate in the baffles, and their compressibility caused the velocity at the nozzle exit to oscillate with unpredictable frequency and amplitude about a mean value. Finally, this original generator also had the disadvantage of non-standard, almost arbitrary geometry which is characteristic of apparatus used by other experimenters (see the discussion in Section 2.3).

To solve the bubble problem, the apparatus was modified to separate the nitrogen in the reservoir from the water by means of a rolling diaphragm (Bellofram model ABC 5-400-850-600-FCJ) guided by a loose piston. The water-level indicator remained in place, and an alarm was added to notify the experimenter if the water dropped below a preset level, to guard against accidental rupture of the diaphragm. A pressure transducer (Wyanco model P2-1251) monitored the pressure on the water side of the diaphragm. Plumbing was also provided to remove any air which might be trapped below the diaphragm.

3.3 The Second Vortex Generator

Quantitative measurements of the flow field were made using a second generator, designed so as to be easily interchangeable with the first one. The baffles and contraction were replaced by a combination of a cylinder and a free piston, as shown schematically in Fig. 6(b). The piston stroke was made variable by changing the piston length, and the valve opening time was always chosen so that the piston stopped flush with the ceiling at the end of the stroke. Thus at the beginning of the generation process the geometric *configuration was a simple cylindrical cavity in a plane wall. At the end of the generation process the wall became an uninterrupted plane.* This scheme made the geometry almost trivial; it eliminated any strong secondary flow at the end of the stroke; and it simplified the influence of the image system for the vortex ring during and after formation.

The fast solenoid valve opened into the space at the top of the cylinder, and the piston was energized by admitting water from the pressurized reservoir. The extension pieces used to change the length of the piston were made of lucite, with a specific gravity only slightly larger than that of water. The operating cycle was fully automated and was triggered by a signal to the fast solenoid valve. At the beginning of the stroke the piston rested against the outlet of the valve with very little free volume. At the completion of the stroke, after a built-in delay, a solenoid valve was opened to connect a small peristaltic pump (Master-flex Model C 7014) to the space above the piston. The pump slowly raised the piston to its original rest position while water from the glass tank filled the space below the piston. A pressure transducer on the pump line sensed the drop of pressure when the piston stopped. The pump was then shut off, and a relief valve was opened briefly to equalize the pressure behind the piston with that of a small water reservoir at atmospheric pressure. The problem of bubbles was further ameliorated by this scheme, since most of the fluid between the valve and the piston was removed after every cycle. Oscillations of the piston were suppressed by mounting two silicon-rubber O-rings on the piston to provide some damping. Seeding for LDV measurements was unnecessary because the fluid in the cylindrical cavity was seeded fluid from the glass tank.

3.4 Flow Visualization

The lip of the cylinder in the second vortex generator was fitted with nine small orifices for dye injection, as indicated in Fig. 6(b). These were manifolded together and connected through a solenoid valve to a dye reservoir. During the time that the piston was being pulled up, water entering the cavity from below was mixed with a concentrated dye solution flowing under gravity. The valve to the dye reservoir was closed when the piston reached its upper rest position.

The dye used for flow visualization (B-1-G-1, manufactured by 7K Color Company) comes in powder form and is highly soluble in water. In solution, at the concentration normally used in the experiments, the specific gravity is 0.995. The dye is easily bleached, using chlorine, with virtually no visible residue. The bleaching rate can be adjusted by controlling the concentration of chlorine in the tank. It was found that a chlorine level of 50-100 ppm was optimal from several points of view. Good photographs were obtained at an acceptable repetition rate, and the seeded working fluid in the tank remained completely free of organic contamination such as algae for long periods of time.

IV. INSTRUMENTATION

4.1 The LDV System

A two-channel tracking laser-Doppler velocimeter (LDV) was fabricated especially for this experiment, using the optical arrangement sketched in Fig. 7. The helium-neon laser (Spectra Physics model 124) has a power output of 15 mW. A lens (FL = 45.0 cm) on the laser focuses the output beam in the common plane* of two partially overlapping radial phase gratings, at a point where the grating lines cross at right angles. The grating line density at this point is nominally 42 lines/mm. The gratings produce a regular square pattern of diverging diffracted beams, with much of the energy concentrated in the four first-order beams (see the Appendix). Two of these beams lie in a vertical plane and two lie in a horizontal plane.

The four first-order beams are at once isolated by a mask. They are made parallel by a fixed primary lens (FL = 66.0 cm) which is mounted with its focal point in the grating plane. A movable secondary lens (FL = 62.9 cm) then causes the four beams to focus and cross within the glass tank. The angle $\theta/2$ between each beam and the optical axis is 2.356 degrees in air, giving a fringe spacing in the horizontal and vertical directions of $\frac{1}{2}\lambda/\sin \frac{1}{2}\theta = 7.69$ μm and a conversion factor of 1.299 kHz per cm/sec. Depending on circumstances, the velocity component normal to the optical axis can be measured in

---

*The term "common plane" is an approximation; the two grating planes are normally separated by a gap of a small fraction of a millimeter to provide clearance for rotation.

the plane defined by any two of the four beams. For measurements close to the ceiling of the tank, for example, only three beams were used, as described in Section 4.3 below.

The glass tank is normally filled with distilled water treated with chlorine (10 ppm) and is seeded with latex particles (styrene divinylbenzene 6PIC, manufactured by Dow Diagnostics) having a nominal diameter of 5.7 μm. These particles have a specific gravity of 1.024 and a settling velocity in water of about 0.1 cm/hour. The water in the tank therefore has to be stirred occasionally to maintain a uniform particle distribution. Seeding concentration during the present measurements was about 2 x 10^4 particles/cm^3, with an average of approximately 10 particles in the focal volume.

The transmitting optics are mounted on an optical bench (Oriel model 112). This bench is supported by a massive x-y traverse mechanism which allows the entire system, and with it the focal volume, to be traversed in a plane normal to the optical axis. On the optical bench, the secondary focusing lens is mounted on a separate traverse mechanism (Velmex model A4015) which allows the focal volume to be traversed along the optical axis as well.

The LDV system has so far been operated only in the forward dual-scatter mode. The receiving optics are carried by a substantial x-y-z traverse mechanism (Velmex 4000 series) mounted on a heavy tripod. The two main components are a collecting lens (FL = 8.7 cm) and a silicon avalanche photodiode (Texas Instruments model TIED 83) which is coupled with a low-noise, high-speed transimpedance amplifier (Texas Instruments model TIEF 132). The photodiode has an active area 0.25 mm in diameter and thus serves as its own pinhole. The position of the photodiode can be adjusted independently of the collecting lens by a miniature x-y-z traverse mechanism (NRC model 450). Alignment of the LDV system at each new measurement position is a simple and relatively rapid operation. The transmitting optics are moved to the desired position, the displacements are matched on the main x-y-z traverse of the receiving optics, and final fine adjustments to optimize the LDV signal are made by means of the miniature x-y-z traverse.

4.2 The Diffraction Gratings

The use of radial diffraction gratings to perform the functions of beam splitting and frequency shifting is not new (e.g., Stevenson, 1970). Neither is the use of bleached or etched phase gratings rather than amplitude gratings to increase the relative intensity of the first-order diffracted beams (e.g., Wigley, 1974; Oldengarm et al., 1976). What is new in the present system is the use of two identical overlapping gratings to produce a compact two-component LDV system in which channel separation is achieved by filtering electronically the signal from a single detector. Also new is the use of digital techniques to remove deterministic noise generated by non-uniform rotation rate and non-uniform line spacing. This latter feature is described in Section 4.5 below.

The optical principles required for design of etched phase gratings are discussed in the Appendix. When both gratings are designed for maximum efficiency in the first-order diffracted beams (i.e., $s/d = 1/2$ and $2(n - 1)\ g/\lambda = 1$, in the notation of the Appendix), all even orders, including zero order, should be absent, and the energy in each of the first-order beams produced by a single grating should be approximately 41 percent of the incident energy.

The grating discs were manufactured by Teledyne Gurley, who cooperated with the author in the development. An existing 16,384-line master was used. The substrate material is optical quality glass. The discs are 13.84 cm (5.45 inches) in diameter and approximately 0.6 cm thick. The discs were ground and polished to be flat and of uniform thickness to within one wave length per cm. The line pattern etched in the glass forms a track with an inner radius of 5.66 cm (2.23 inches) and an outer radius of 6.82 cm (2.69 inches). The track is concentric with the outside diameter to 25 μm (0.001 inch) or better. To maximize the intensity in the first-order beams, the land width s was specified to be half the line pitch d, and the depth of etching was calculated for the known index of refraction (C-1 glass; $n = 1.5235$). It was found that this etching depth was difficult to control, and several samples had to be made before the result was satisfactory. A scanning-electron-microscope photograph* of a cut through one early sample is shown in Fig. 8. The final product has a

---

*This photograph was obtained through the courtesy of Mr. Kenneth Evans of the Jet Propulsion Laboratory.

value of s/d less than 0.50 and an etching depth which exceeds the specified dimension. As a result, the energy in each of the first-order beams for a single grating is reduced to approximately 15 percent of the incident energy. There is also some loss of intensity because the gratings, and most of the other optical surfaces as well, are not anti-reflection coated. Nevertheless, the available laser power of 15 mW is quite sufficient to provide a satisfactory Doppler signal at the detector. Weak even-order beams are present in the pattern; the zero-order beam in particular is very useful for aligning the optical system.

4.3 Frequency Shifting

Each of the grating discs is attached to a stainless-steel hub and mounted on the shaft of a hysteresis-synchronous motor (Beau model 40H-36, 40H-96). The motors face each other in a special box structure, as shown in Fig. 9, with the discs partially overlapping and the etched tracks also facing one another. Runout and wobble are less than 10 μm (0.0005 inch). The motors have three selectable synchronous speeds (1800-900-450 rpm for one motor; 1200-600-300 rpm for the other) when powered by the 60-Hz line.

The fact that the grating lines are radial rather than rectilinear is not a serious defect in practice. If the disc rotates with angular velocity Ω and the incident beam is at radius R from the center of rotation, the frequency shift $f^{(m)}$ in the diffracted beam of order m (see the Appendix) is

$$f^{(m)} = \frac{m}{d} \Omega R \tag{22}$$

where d, the line pitch, is related to the total number of lines N by

$$d = \frac{2\pi R}{N} \tag{23}$$

Finally, therefore,

$$f^{(m)} = \frac{1}{2\pi} m N \Omega \tag{24}$$

The frequency shift in each order thus depends only on the total number of lines on the disc and on the angular velocity of the disc; it does not depend on the radius R or on the wave length of the incident light.

If the two gratings rotate independently of each other, each of the diffracted beams undergoes two successive frequency shifts; thus

$$f_1{}^{(m)} + f_2{}^{(n)} = \frac{1}{2\pi} (m_1 N_1 \Omega_1 + n_2 N_2 \Omega_2) \tag{25}$$

Various modes of operation suggest themselves. In the standard mode used for the bulk of the present measurements, as illustrated in Fig. 10, typical bias frequencies (Doppler frequencies for a particle at rest) for the first-order beams in the vertical and horizontal planes are

$$\begin{aligned} F_1 &= 2f_1 - 2f_2 \\ F_2 &= 2f_1 + 2f_2 \end{aligned} \tag{26}$$

In principle and in practice, the separation between F_1 and F_2 can be made sufficiently large so that a single detector can sense the

Doppler signal from both channels simultaneously, and the two signals can be subsequently be separated electronically by band-pass filtering. The numerical values of f_1 and f_2 can be varied by changing Ω_1, Ω_2 and the direction of rotation of the gratings. Note that reversing the direction of rotation of one grating interchanges the two channels, because $|2f_1 + 2f_2|$ becomes $|-2f_1 + 2f_2|$ and $|2f_1 - 2f_2|$ becomes $|-2f_1 - 2f_2|$. This property can be useful if the mean values and/or the dynamic ranges of the two velocity signals are not initially known.

The four-beam geometry also provides unwanted velocity information in directions along the perimeter of the pattern in Fig. 10, with bias frequencies $2f_1$ and $2f_2$. Careful choice of f_1 and f_2 enables enough separation between the four bias frequencies sensed at the photodetector $(2f_1 + 2f_2,\ 2f_1 - 2f_2,\ 2f_1, 2f_2)$ to suppress the undesired signals.

For measurements close to a wall, or as a check on system accuracy, three of the four beams in Fig. 10 are sufficient to determine the two velocity components. In the notation of the adjacent sketch, let v be the velocity component parallel to the wall and let u' be the velocity component along one diagonal at an angle of 45 degrees to the wall. The angle θ between the two beams equidistant from the wall differs from the angle θ' between the beams along the chosen diagonal. Let R and R' be the Doppler constants (in cm/sec per kHz, say) for v and u' respectively.

Evidently,

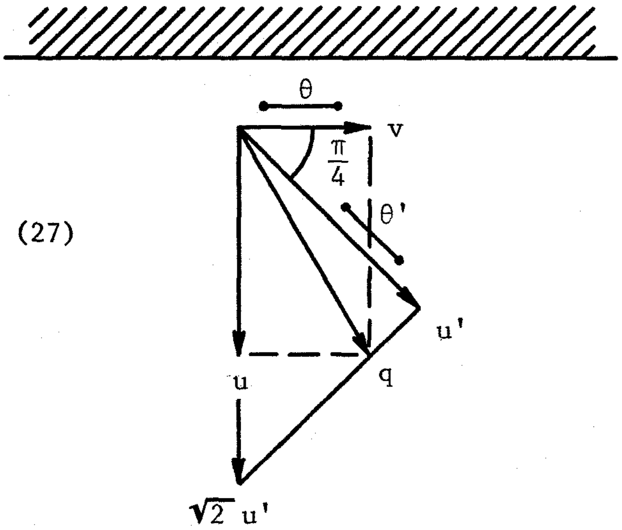

$$\frac{R}{R'} = \frac{\sin\frac{\theta'}{2}}{\sin\frac{\theta}{2}} = \frac{1}{\sqrt{2}} \qquad (27)$$

Let $\nu = v/R$ and $\nu' = u'/R'$ be the residual Doppler frequencies after subtraction of the bias frequencies. It follows from the sketch that

$$v = R\nu$$
$$u = \sqrt{2}\,u' - v \doteq \sqrt{2}\,R'\nu' - R\nu = R(2\nu' - \nu) \qquad (28)$$

4.4 The Tracking LDV Processor

A two-channel digital processor was designed and fabricated to convert the raw Doppler signals into a form suitable for input to the data-acquisition system. The analog Doppler signal has variations in amplitude and phase as well as frequency. In the present processor, a TTL pulse train which retains the frequency and phase information is triggered by zero crossings of the Doppler signal. Each zero crossing is validated by an amplitude test of the input signal. Because the validating circuit has to be reset after each pulse by detection of a negative and a positive threshold crossing of the input signal before the next pulse can be triggered, only one TTL pulse is generated for each zero crossing. The TTL version of the input signal is fed to a digital phase-lock loop (PLL)(Motorola MC 14046) which has identical lock-in and capture ranges, good harmonic rejection, and an adequate frequency range (up to 2.5 MHz). The PLL does not respond to momentary high-frequency phase noise originating when a particle enters or leaves the test volume. The response of the loop to a step in input frequency was examined, and the natural frequency and damping factor were tuned to ensure optimal dynamic response to sudden large changes in velocity.

A high-speed counter section (Advanced Micro Devices AM 93516) samples the Doppler frequency at the voltage-controlled oscillator of the PLL by counting pulses from a 60-MHz crystal clock for a specified number of Doppler cycles. This number can be set externally for each channel from the front panel. The counting operation begins on command from an external pacer, normally set to a frequency of 1 kHz, and is carried out simultaneously on both channels. At the end of the counting operation the two counts are stored in internal registers, a flag is issued to the data-acquisition system, and two words of 16 bits each are multiplexed onto a data-transmission bus. Sampling rates up to 4 kHz can be accommodated, with a velocity resolution of 0.1 cm/sec and a slewing rate of at least 10000 cm/sec per second. All of the counting operations can be controlled manually or remotely and can be cleared/started/stopped upon command. An analog output from the PLL provides a frequency-to-voltage conversion of the input Doppler signal.

Only bits 0-13 in each data word are used for clock data. Bit 14 is used for dropout/overflow indication, and bit 15 is used for channel identification. Occasional dropouts in the analog Doppler signal may occur because of a momentary deficiency of seeding particles in the focal volume. The associated momentary drop of input amplitude is detected by the input circuitry. A delay is triggered; if the input amplitude does not recover within a specified time, the dropout bit (normally false) is set true. The sampling process is not interrupted. When the input amplitude recovers, the dropout bit is cleared after a further delay which is adjusted to match the PLL tracking time constant. The dropout bit is also set true if either of the high-speed (60-MHz) counters overflows.

4.5 Grating Noise

At an early stage of development, a test was carried out with the processor linked to the data-acquisition system at the normal sampling frequency of 1 kHz, and with fluid stationary in the focal volume. Such a test provides useful information about overall system noise originating in the transmitting optics, the test volume, the receiving optics/electronics, and the processor. When the mean bias frequencies for the two channels were examined, agreement with the theoretically predicted frequencies was excellent. However, periodic fluctuations corresponding to apparent velocity excursions (peak-to-peak) of about one cm/sec were present in the signals. These fluctuations were synchronized with the rotation of the gratings. Possible causes might include slight variations in etching depth, slight irregularities in line spacing, slight out-of-plane wobble, or slight variations in motor speed (primarily cogging). As it turned out, four dominant periods were found in the fluctuations. Two of these periods could be associated with each motor; in each case they were the period per revolution and the period per pole.

In the present application, it was a non-trivial problem that the grating rotation was not synchronized with data sampling when the grating motors were driven by the 60-Hz line. This problem was solved by deriving a line frequency for each motor from the same 10-MHz crystal whose output pulse train served (after division by 10^4) as a system pacer or clock. The method was to divide the 1-kHz pacer signal once more by a suitable integer in the range from 14 to 20, depending on the filter settings being used for channel separation. The final pulse frequency, in the range from 50 to 70 Hz for each motor, was transformed to a sine wave and fed to one channel of a high-fidelity stereo power amplifier (SAE model 2200) equipped with step-up transformers to provide the voltage required by the motors.

Figure 11 is a typical record of grating noise, showing an rms level of about 0.7 cm/sec, with several steps in its removal. The sampling rate was 1 kHz and the duration of the record was one second. The four-pole motor was driven at $\sim$ 1071 rpm (in the 8-pole switch position) by a frequency of 1000/14 Hz. The rotation period was 56 msec and the pole period was 7 msec. The six-pole motor was driven at 1250 rpm by a frequency of 1000/16 Hz. The rotation period was 48 msec and the pole period was 8 msec. These four frequencies being precisely known, phase and amplitude could be accurately determined for each component by Fourier analysis. When all four components are subtracted from the original data, the residual fluctuations in the measured frequency correspond to rms velocity fluctuations of about 0.06 cm/sec, as shown in the lowest trace in Fig. 11. These residual fluctuations may be due in part to mechanical vibration of the structure which supports the transmitting optics.

Normal data acquisition always included a preliminary data record, with the fluid essentially stationary in the tank (see Section 5.2 below). This preliminary record was analyzed in the manner just described to find the grating noise signal, which was then subtracted from all subsequent data records. The relative location of the latter records in time was controlled by the computer and was therefore accurately known.

V. THE MAIN EXPERIMENT

5.1 Experimental Conditions

Two-channel LDV measurements were made of the velocity field associated with one particular turbulent vortex ring. The vortex generator was the piston-cylinder apparatus previously sketched in Fig. 6(b) and described in Section III (especially Section 3.3). The operating conditions for the vortex generator were chosen to give a vortex ring well inside the turbulent regime of the transition map in Fig. 4, at a point where dye visualization showed a well-defined and highly repeatable flow structure. To slightly exaggerated accuracy, the kinematic viscosity during the experiment was 0.0100 $\mathrm{cm}^2/\mathrm{sec}$ (20° C). The orifice/piston diameter D_0 was 1.905 cm (3/4 inch) and the piston stroke L_0 was 6.517 cm (2.566 inches). Hence $L_0/D_0 = 3.421$. The reservoir pressure was 2100 kPa (300 psi). The valve opening time was 51.0 msec. Hence $\overline{U}_0 = 127.8$ cm/sec, $I/\rho = 2374\ \mathrm{cm}^4/\mathrm{sec}$, and, from Eq. (18) with $P = 1$, $\Gamma_0/\nu = 41640$. This operating point is denoted by a double circle in Figs. 3(a), 4, and 5.

The motion will be described in a cylindrical polar coordinate system (x, r, θ), with corresponding velocity components (u, v, w). The axial coordinate x increases downward, with the origin in the plane of the orifice. Velocity measurements were made for an ensemble of 100 vortices at each of numerous stations. Most of these stations lay in a plane which was normal to the optical axis of the LDV system, as shown in Fig. 12, and which contained the nominal axis of symmetry of the fluid motion. Major traverses were (a) an axial traverse along the axis of symmetry from $x = 0$ to $x = 50.0$ cm; (b) two radial traverses <u>normal to</u> the optical axis at $x = 35.0$ cm and at $x = 42.5$ cm; and (c) a radial traverse <u>along</u> the optical axis at $x = 42.5$ cm. Some measurements were also made close to the orifice, at $x = 0.1$ cm.

5.2 Data Acquisition

One of several data-acquisition systems in GALCIT, the Solo System, was programmed to control the experiment. The data system operated the vortex-ring generator and its peripheral electronics, acquired and stored data from the LDV processor, and processed and displayed some of the data in real time for monitoring purposes. The main system component is an HP 2100A computer having 64K (65536) bytes of core memory. Peripherals include CRT terminal, cartridge disc, phase-encoded magnetic-tape transport, line printer, plotter, graphics display, and analog-to-digital converter. A general-purpose 16-bit digital I/O channel and an HP IB channel are available. The operating system is the real-time-excecutive system RTE-II.

A 10-MHz crystal-controlled pulse train was used as a master clock for the measurements. Division by 10^4 generated a 1-kHz pulse train called PACER which served as a local time base. The timing of data acquisition is explained in Fig. 13. Running in the background is a global timer called GAMMA whose output is normally false but becomes true for 90 seconds after a trigger pulse is received. This waiting time of 90 seconds is the interval between vortex rings; it was chosen after some preliminary measurements showed that velocity fluctuations in the tank decayed sufficiently during this time to assure minimal interaction between successive rings.

The computer first sets up a direct-memory-access (DMA) channel for transfer of 2500 words, and waits until GAMMA is false. The LDV processor is then cleared and started. Beginning with the next PACER pulse, 1250 pairs of velocity-data words are transferred from the processor to the computer, at a rate of one pair per millisecond, and are written as one record on magnetic tape. At this time the flow has not yet begun; the data in question are needed to determine the phase and amplitude, for each LDV channel, of four dominant frequencies in the grating noise. These frequencies are phase-locked to the PACER signal, as explained in Section 4.5 above. After the last data flag of this transfer, but before the next PACER pulse, the computer starts a local timer called LDLAY, fires a vortex ring at the next PACER pulse, clears the processor, sets GAMMA true, waits for LDLAY msec until a signal arrives from the local timer, and starts the processor. The interval LDLAY is provided to allow the vortex ring to form and to travel through part of the distance from the orifice to the test volume of the LDV before data acquisition begins. During LDLAY, a DMA transfer of 10000 words is set up. After the last data flag of this transfer, four data records of 2500 words each are immediately written on magnetic tape. Data acquisition is thus complete five seconds after the end of LDLAY.

The five data records (12500 words) are next read from magnetic tape back into memory to verify that no writing errors occurred. During the approximately 85 seconds until GAMMA again goes false and the next vortex ring is generated, the amplitude and phase of the four components of grating noise are calculated from the first data record. This noise is subtracted from the remaining raw data. Useful portions of the two velocity traces for the current vortex are plotted on the graphics display and on the system plotter. Under normal conditions a hundred such traces are plotted, one on top of the other for each channel. A typical example at $x = 35$ cm, $r = 0$ is shown in Fig. 14. Dropout statistics and peak velocities (maximum and minimum) for each channel are written on the CRT and on the line printer.

When GAMMA again goes false, after 90 seconds, the sequence just described is repeated for the next vortex ring. The data file on magnetic tape is closed when 100 vortex rings have been observed at a given measurement station. The LDV system is then moved manually to a new measurement station and realigned, the pressurized reservoir is refilled with distilled water, and the experimental cycle is repeated at the new station.

VI. THE APPARENT ORIGIN

6.1 Similarity and Apparent Origin

For experimental purposes, it is sufficient to take the origin for x in the plane of the orifice and the origin for t at the beginning of the generation process. Before the resulting data can be interpreted in similarity variables, however, it is necessary to define and determine an apparent origin (x_0, t_0) in space and time.

According to Eq. (9), the stream function in similarity coordinates, with the apparent origin taken into account, is

$$S = \Psi \left(\frac{\rho}{I}\right)^{3/4} (t - t_0)^{\frac{1}{4}} = S(\xi, \eta) \qquad (29)$$

where the space coordinates in similarity form are

$$\left.\begin{aligned} \xi &= (x - x_0) \left[\frac{\rho}{I(t - t_0)}\right]^{\frac{1}{4}} \\ \eta &= r \left[\frac{\rho}{I(t - t_0)}\right]^{\frac{1}{4}} \end{aligned}\right\} \qquad (30)$$

The velocity components defined by Eqs. (1) become

$$\left.\begin{aligned} U &= u \left(\frac{\rho}{I}\right)^{\frac{1}{4}} (t - t_0)^{3/4} = \frac{1}{\eta} \frac{\partial S}{\partial \eta} \\ V &= v \left(\frac{\rho}{I}\right)^{\frac{1}{4}} (t - t_0)^{3/4} = -\frac{1}{\eta} \frac{\partial S}{\partial \xi} \end{aligned}\right\} \qquad (31)$$

The essence of these relationships is set of simple rules for any point which is fixed in similarity coordinates;

(a) $r \sim (x - x_0)$

(b) $(x - x_0)^4 \sim (t - t_0)$

(c) $u^{-1/3} \sim (t - t_0)^{\frac{1}{4}} \sim (x - x_0)$

The rules just stated have been recognized and applied by several previous students of the turbulent puff or the turbulent vortex ring. For example, motion pictures or probe measurements were used with rule (a) to verify the property of conical growth, and thus to determine x_0, by Grigg and Stewart (1963), Richards (1965), Johnson (1970), and Kovasznay et al. (1973). An alternative method based on rule (c) was also used by Kovasznay et al, who took u to be either the overall celerity* or the peak mean velocity on the axis of symmetry. Once the origin for x is known, rule (b) allows the origin for t to be determined, as in the papers by Grigg and Stewart, Richards, and Johnson. Roughly speaking, for a puff both x_0 and t_0 tend to be positive; i.e., the origin in x is downstream of the orifice, and the origin in time is later than the actual beginning of the motion. For a vortex ring with a thin core the opposite is usually true, as was first noted by Turner (1957).

6.2 Application to the Present Data; First Stage

The rules just outlined were used to determine x_0 and t_0 for the present measurements, using data obtained on the axis of symmetry. However, severe problems with dispersion caused the actual calculation to become quite elaborate. The basic difficulty is that the Reynolds

---

*This method using celerity can also be shown to work well with the data of Sallet and Widmayer (1974), although these authors did not concern themselves with the question of similarity.

number for a turbulent vortex ring decreases continuously, like $(t - t_0)^{-\frac{1}{2}}$, during its lifetime. An important mechanism in this decay process is irregular shedding of vorticity (i.e., smoke or dye) into the wake, as suggested by Fig. 1(b) above and by similar photographs published, for example, by Johnson (1970), Maxworthy (1974), Sallet and Widmayer (1974), Oshima et al. (1977), and Schneider (1980). An important consequence of the irregularity is a substantial dispersion of the trajectories of individual vortex rings in both space and time. The problem has already been illustrated in Fig. 14, which displays the ensemble of raw traces for axial and radial velocities for 100 vortex rings observed at $x = 35$ cm, $r = 0$. The peak in the axial velocity in the upper part of the figure shows considerable scatter both in amplitude and in arrival time. The radial velocity often shows the N-shaped profile which is characteristic of flow off the axis of symmetry. This problem of dispersion has not been faced squarely by any previous investigator, and resolution of the problem was in fact a major preoccupation throughout the present research. The need was to eliminate from a given ensemble all or most of the traces showing anomalous behavior, without biasing or prejudicing the mean properties of the remaining data. A procedure was devised for this purpose, after considerable development, and applied to the various data files on the axis of symmetry.

There were two stages. The first stage was carried out in physical variables. It emphasized the peak velocity u_p and the corresponding arrival time t_p for data on the axis of symmetry, and it led in the usual way to an estimate of x_0 from a plot of $u_p^{-1/3}$ against x, followed by an estimate of t_0 from a plot of $(x - x_0)^4$ against t_p. The second stage, carried out in similarity variables, improved these estimates by forcing the best possible collapse onto a single curve of the various mean traces observed not just at the peak, but over a finite time interval corresponding to passage of the main body of the vortex ring. Important steps in the first stage were:

(a) Data preparation. For each of the 100 vortex rings in a file, the peak axial velocity u_p in the raw data and the corresponding arrival time t_p were first determined by the computer. A time window was set to include all data (in both channels) in an interval of 360 msec centered on t_p; this window included the non-trivial part of the signal from the passing vortex. The bias frequency for each channel was subtracted. Grating noise was removed, using amplitude and phase information computed from the first data record (see Sections 4.5 and 5.2). Occasional gaps caused by momentary dropout of the Doppler signal during data acquisition were filled in by linear interpolation. The data were crudely low-pass filtered; i.e., each data point was replaced by the mean of five symmetric points. The characteristic values u_p, t_p were revised as necessary. The time window was reduced to 191 msec, again centered on t_p for each trace.

(b) Screening on the basis of arrival time. Preliminary values for the mean arrival time $\langle t_p \rangle$ and the deviations $t_p - \langle t_p \rangle$ from this mean were calculated, using data for all 100 vortex rings of the ensemble. Rings with very large deviations were excluded from further consideration, and $<t_p>$ was revised. Each of the surviving traces was shifted in time to make t_p coincide with $<t_p>$, and mean traces $<u(t)>$ and $<v(t)>$ were computed. At this point a preliminary value $<u>_p$ was available for the peak in the mean axial velocity.

(c) Screening on the basis of radial velocity. The original time window of 191 msec was reduced to the smallest common interval. The two velocity traces within this window were rectified and integrated over time, using Simpson's rule. The time integrals for the rectified radial-velocity component were examined, and vortex rings having large numerical values for the integral (i.e., values not negligibly small compared to the corresponding integral for $<u(t)>$) were excluded, on the ground that they were unacceptably far off-axis in a direction normal to the optical axis of the LDV system. The mean axial trace $<u(t)>$ was suitably revised.

(d) Screening on the basis of axial velocity away from the maximum. The axial-velocity trace for each of the remaining vortex rings was compared to the mean in terms of the rms value of the deviation $u(t) - <u(t)>$ over the width of the reduced time window. The rms value was scaled by $<u>_p$. The result, denoted by ε, was minimized for each vortex by a slight additional shift of the velocity traces in time. A revised mean $<u(t)>$ for the axial velocity traces was again constructed, and the process was iterated until there was no further change in the data. A listing of ε, together with a listing of the time integrals for the rectified axial-velocity component, was inspected, and a few vortex rings with large ε were discarded, on the ground that they were unacceptably far off-axis along the optical axis of the LDV system.

The process just described was repeated several times, as necessary, until the population at each measurement station on the axis of symmetry was reduced to approximately 30 vortex rings. The dispersion in trajectory for this population was expected to be small and roughly circular with respect to the geometric axis, although the actual scale of the dispersion was unknown. When the values finally obtained for $<u>_p$ were plotted as $<u>_p^{-1/3}$ against x, as shown in Fig. 15, a straight line visually fitted to the data yielded the preliminary estimate $x_0 = -117$ cm. Since the physical distance from the orifice to the various measurement stations did not exceed 50 cm, the apparent origin in space is evidently quite far upstream from the orifice. When $(x - x_0)^4$ was plotted against $<t_p>$, as shown in Fig. 16, a straight line visually fitted to the data yielded the preliminary estimate $t_0 = -329$ msec. Despite some scatter, the data are well represented by straight lines in Figs. 15 and 16, even quite close to the orifice, and the concept of similarity is therefore strongly supported by the data. To illustrate the situation at the end of this first stage, the final mean trace $<u(t)>$ at $x = 35$ cm, $r = 0$ has been superposed on the raw traces in the upper part of Fig. 14.

6.3 Application to the Present Data; Second Stage

In the second stage of the procedure for finding the apparent origin in the presence of dispersion, a method was sought to improve the fitting operation by taking into account the behavior of the mean axial-velocity traces away from the peak. The mean traces were therefore converted to similarity variables. The strategy was to average the various ensemble-mean profiles $<u>$ from the first-stage operation, each now expressed as $U = <u(t)> (\rho/I)^{\frac{1}{4}}(t - t_0)^{3/4}$, so as to obtain a single optimum profile $\overline{U}$ as a function of the similarity variable $\xi = (x - x_0)(\rho/I)^{\frac{1}{4}} (t - t_0)^{-\frac{1}{4}}$. The strategy was thus similar to the one described under (d) just above, except that the ensemble was now the set of 14 mean signals. Given values for the two parameters x_0 and t_0, each mean axial-velocity profile $<u>$ was transformed into $U(\xi)$, using linear interpolation in t to space the data uniformly in ξ. The average profile $\overline{U}(\xi)$ was computed, and a shift in ξ was imposed* to minimize the rms deviation $\varepsilon = U - \overline{U}$ for each profile over the least common range of definition. The average $\overline{U}$ was recalculated, and the time shifts were revised, until there was no further change.

This procedure was implemented as a search in (x_0, t_0)-space, with the object of minimizing $\overline{\varepsilon}$, the rms value of ε over the ensemble. An important discriminant turned out to be a phenomenon

---

*This shift was always small enough to be interpreted as an equivalent uniform shift in time, without regard to similarity.

resembling an accordion motion in the required time shifts. For given t_0, a poor choice for x_0 could cause early data (i.e., data close to the orifice) to migrate to later times, and later data to migrate to earlier times, or vice versa. For the original estimates $x_0 = -117$ cm, $t_0 = -329$ msec, for example, the shifts were such as to distort the time interval from first to last station by seven percent. When this accordion effect was minimized (with respect to choice of x_0 for given t_0), a sharply defined trajectory in (x_0, t_0)-space emerged. Along this trajectory the residuals $(U - \overline{U})_p$ at the peak were nearly random. The discriminant $\overline{\varepsilon}$ first decreased noticeably as t_0 became more negative, and then became essentially constant at about $t_0 = -400$ msec.

In view of this experience, the origin of coordinates for the similarity variables was finally chosen to be

$$x_0 = -145 \text{ cm}$$

$$t_0 \doteq -440 \text{ msec}$$

The corresponding straight lines are included in Figs. 15 and 16. Because these lines are not fitted to the peak data of the figure, but to the whole experimental record in a neighborhood of the peak data, they may not appear to be the optimum fit that they really are.

The equation of the straight line in Fig. 16 is $(x - x_0)^4 = B(t_p - t_0)$, with $B = 9.262 \times 10^8$ cm^4/sec. The locus of peak axial velocity on the axis of symmetry therefore has the celerity

$$c_p = \left(\frac{dx}{dt}\right)_p = \frac{B}{4(x-x_0)^3} = 39.70 \text{ cm/sec}$$

at $x = 35$ cm (or $x - x_0 = 180$ cm). According to the similarity argument, the corresponding celerity c_0 in the plane of the orifice is larger by a factor $(x - x_0)^3/(- x_0)^3 = 1.913$, so that $c_0 = 75.95$ cm/sec. In Section 5.1 the piston velocity was given as 127.8 cm/sec. A reasonable inference is that entrainment during the formation process substantially increases the initial volume of fluid associated with the ring. In the present instance, the increase is perhaps 70 percent of the cylinder volume.

Finally, in similarity coordinates the celerity of the locus of peak axial velocity is independent of x and has the value

$$C_p = c_p \left(\frac{\rho}{I}\right)^{\frac{1}{4}} (t - t_0)^{3/4} = \frac{1}{4}\left(\frac{B}{I/\rho}\right)^{\frac{1}{4}} = 6.248$$

The various axial-velocity profiles on the centerline are shown in similarity form in Fig. 17. Figure 17(a) refers to the preliminary estimates $x_0 = - 117$ cm, $t_0 = - 329$ msec, and Fig. 17(b) refers to the final estimates $x_0 = - 145$ cm, $t_0 = - 440$ msec. The ordinate in each case is scaled with the peak value $\overline{U}_p$. The quality of the final fit can be judged from the listing of various associated quantities in Tables 1 and 2. Over the fitted range, the peak velocity $\langle u \rangle_p$ in physical coordinates varies by about a factor of two, whereas the scatter in U_p in similarity coordinates for the final fit is about two percent.

VII. PROCESSING OF OFF-AXIS DATA

The procedure by which effects of dispersion were suppressed on the axis of symmetry (see Section 6.2) is not feasible for data off the axis. On the axis, each population was examined independently of the others, and the symmetry of the flow was exploited by retaining only the 30 percent or so of the realizations which showed very little disturbance in the radial component of velocity. Off the axis, each experimental population at a given radius again contains many profiles which properly belong to other measurement stations at other radii. These profiles ought not to be discarded, as they were for the data on the axis. On the other hand, if each population were to be simply averaged, with only superficial shifting and screening, much essential structural detail would be lost through effects of dispersion, especially near the vortex core.

To solve the problem of dispersion, a procedure was developed which scanned the whole of the data, without regard to the radius of the measuring point, and assembled subsidiary populations consisting of traces which closely resembled each other. The procedure processed each of these populations separately and assigned the resulting mean profiles for <u> and <v> to the average radial position. One new element in this procedure was that the technique of pattern recognition became more subtle. Another was that the radial position became a dependent variable whose value was not known until the end of the final screening operation for each population.

7.1 Some Preliminaries

The standard data-preparation process (cf. step (a) of Section 6.2 above) was first applied to all of the data files in the radial traverse at $x = 35$ cm (see Fig. 12). Altogether, 1800 vortex rings were involved. Each ring was assigned an identification number made up of its file number on magnetic tape (representing the radial coordinate of the measurement station) and a serial number from 1 to 100 within the file. Two basic parameters were established for each vortex ring, as indicated in the sketch. These were the peak-to-peak

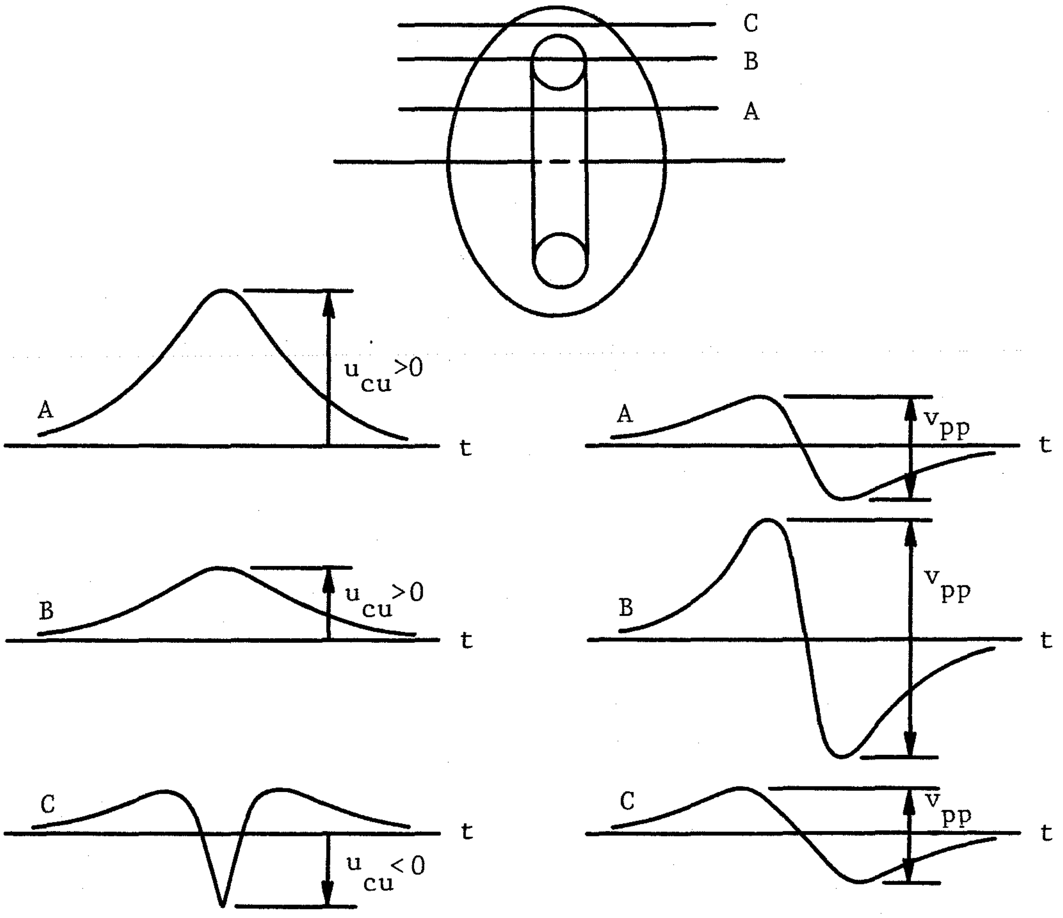

amplitude v_{pp} for the radial velocity and the value u_{cu} of the axial velocity at a particular extremum which was expected to lie very nearly in the plane of the vortex core. The notation v_{pp} is self-explanatory. The notation u_{cu} refers to the fact that the extremum in question is easily identified visually but is not so easily identified by the computer. A program was therefore written to superpose a vertical cursor on a graphics display of each axial-velocity time trace. The cursor was moved in the time coordinate by command from the system console until it coincided with the desired extremum, and the corresponding time t_{cu} was recorded along with u_{cu}. This operation was carried out for each of the 1800 vortex rings in the total population. A screening operation on the basis of the deviation $t_{cu} - \langle t_{cu} \rangle$ in arrival time (cf. step (b) in Section 6.2) was then applied to the 1800 traces as a group, and certain realizations were excluded. Data obtained at the five stations nearest the centerline (stations, 32, 31, 15, 16, 17 in Fig. 12) were next examined for symmetry in terms of the frequency of occurrence of various positive and negative values for v_{pp}. The conclusion was that the real axis of symmetry was not displaced from the geometric axis by more than a small fraction of a millimeter. This displacement was neglected, and data obtained at stations 32 and 31 were set aside. At this point, a population of 1542 realizations remained. Of these, any which showed the first extremum in v to be negative were reflected by inverting the v-traces and assigning the data to the same radius on the opposite side of the axis $r = 0$.

7.2 Generation of the Ensembles

The next step was to order the surviving realizations in terms of u_{cu} and v_{pp}. The expected variation of these parameters with radius is depicted in the upper part of the sketch. Because the functions $r(u_{cu})$ and $r(v_{pp})$ are double-valued in certain ranges of their arguments, it was essential to distinguish different regions of the vortex-ring flow. The method finally used was to ignore the radius and to work in coordinates (u_{cu}, v_{pp}), as indicated in the lower

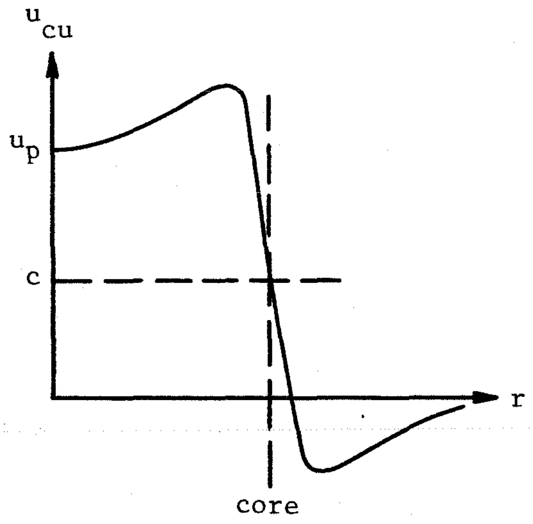

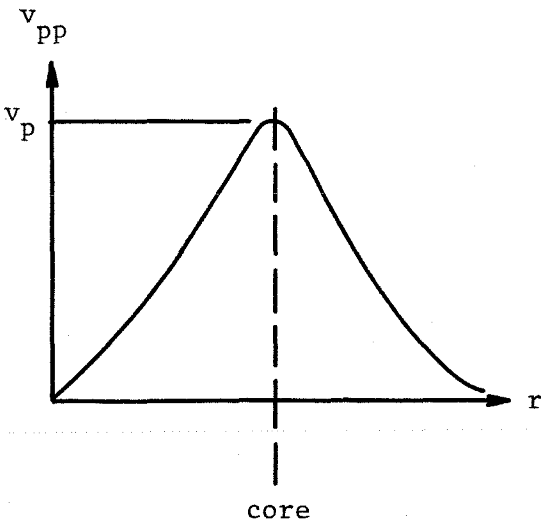

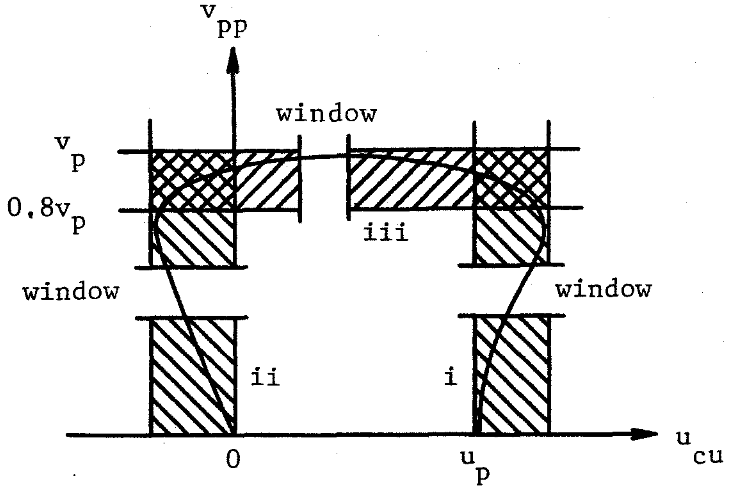

part of the sketch. The available population was divided into three sub-populations along the main segments of the curve; i.e.,

(i) $u_{cu} \geq u_p$; order rings according to v_{pp} (called v'_{pp})
(ii) $u_{cu} \leq 0$; order rings according to v_{pp} (called v''_{pp})
(iii) $v_{pp} \geq 0.8v_p$; order rings according to u_{cu}

Some overlap of population (iii) with populations (i) and (ii) was desirable, and the lower bound of $0.8v_p$ was in fact chosen to guarantee such an overlap.

Distribution functions for some of these populations are shown in Fig. 18. The ordinate is the number of realizations for which the variable is less than or equal to the value on the abscissa. Fig.18(a) shows $N(u_{cu})$ for the entire population of 1542 vortex rings. The plateau region corresponds to the precipitous change in u_{cu} on passing through the vortex core; this region contributes to population (iii). Figs. 18(b) and (c) show $N(v'_{pp})$ and $N(v''_{pp})$ for populations (i) and (ii), with 779 and 722 vortex rings respectively.

7.3 Processing

Consider population (i), which presumably includes only rings which were sampled between the axis of symmetry and the inner edge of the core. By restricting v_{pp} to a relatively narrow range, an ensemble of rings was constructed having at least one component in common. This ensemble was first processed by the usual procedure of calculating $\langle t_{cu} \rangle$, aligning all the traces in time, and computing the average profiles $\langle u \rangle$ and $\langle v \rangle$ for a centered time interval of 191 msec. The processing next concentrated on the component $u(t)$. Each pair of traces was further adjusted in time so as to minimize the rms deviation in $u - \langle u \rangle$ over the least common time interval. The rms deviation in $v - \langle v \rangle$ was also computed. The ten percent of the rings which had the largest deviations for u were discarded, and likewise v; duplicate discards were common. This entire process was repeated once more to improve the mean profiles, except that no more rings were discarded. Finally, both velocity traces for each of the surviving realizations were compared visually to the corresponding mean profiles, using the graphics display, and the results were judged to be entirely satisfactory for both components of velocity.

The same procedure was carried out for population (iii) except that the final time shifts were chosen to minimize the rms deviation in $v - \langle v \rangle$, because of the small amplitude of $\langle u \rangle$ for this population.

In all of this processing, the width of the window in v_{pp} (i.e., the velocity range) was adjustable. It could be enlarged as necessary, up to a specified maximum width, so as to include at least a specified number of trace pairs. This number was normally in the range 50 to 100. The window was advanced in steps smaller than its width, so that most trace pairs were used several times.

The particular rings which finally defined each pair of mean profiles $\langle u \rangle$ and $\langle v \rangle$ were identifiable; i.e., they were associated with known values of the radius r. The mean radius $<r>$ was calculated from these known values and was stored along with a table of identification numbers for later use, because the mean profiles still had to be extended over a larger time interval (see Section 8.1 below).

The third population (iii) was similarly processed, mutatis mutandis, to fill in the region near the vortex core. The ensembles tended to be smaller in this region, because of the general scarcity of data, but they never included less than 35 rings.

Figures 19(a) and 19(b) show the characteristic values $<u_{cu}>$ and $<v_{pp}>$ as a function of radius $<r>$ for the various ensembles constructed by the procedure just described. There are 80 ensembles in all, of which 34, 13, 33 were derived from the populations (i), (ii), (iii), respectively. These data are not primary; they were extracted from the calculations for two secondary purposes. One was to verify that the density of data points was adequate. The other was to expedite the development of curve-fitting procedures which would eventually be required to estimate mean vorticity and to test continuity in the primary data.

7.4 Curve Fitting

The solid lines in Figs. 19(a) and 19(b) were obtained by a piecewise polynomial fit to the data at equally spaced values of the radius r. A third order polynomial was used. A window was centered on the chosen radius and was opened symmetrically to include a fixed number of data points (15 was found to be optimal). The fitted region thus had a variable length, depending on the density of the data points. A lower limit on the number of data points to be included in the window was dictated by occasional gaps in the data. The same procedure was applied a second time to the equally-spaced calculated data, using a smaller window (11 points), to smooth the fitted curve. This second fit played the role of a quite efficient low-pass filter, and greatly reduced the scatter in values obtained for the derivative of the fitted curve.

7.5 Dispersion

A byproduct of the calculations just described was a probability density for radial positions for each ensemble. When these densities are normalized to a standard population and plotted against relative radius (i.e., the distributions are taken to have zero mean), the result is as shown in Fig. 20. The standard deviation of a fitted Gaussian distribution is 0.41 cm. This value presumably measures the dispersion in trajectory at a distance of 35 cm from the orifice. It seems likely that this dispersion could be reduced only with great difficulty. Scrupulous care was already taken to make the generation process very repeatable, and the experiment was certainly not made easier by the decision to wait a relatively long time between vortex rings (see Section 5.2).

The quantitative estimate just made of dispersion suggests that dispersion in a direction normal to the optical plane (i.e., along the optical axis of the LDV system) should not be a source of serious error. The traces recorded and interpreted as radial velocity are actually projections of radial velocity on the optical plane (if the azimuthal velocity is zero). The populations were not large enough to resolve this particular effect of dispersion, but it is expected to be negligible after the enforced elimination of realizations with untypical profiles for either the axial or the radial component of velocity.

VIII. STRUCTURE IN SIMILARITY VARIABLES

8.1 Data Preparation

For each of the 80 ensembles defined by the procedure of Sections 7.2 and 7.3, mean profiles for $<u(t)>$ and $<v(t)>$ were next constructed for a time interval 1533 msec long, starting 400 msec after the trigger pulse which opened the valve (i.e., starting well before the arrival of the vortex at the LDV test volume). Each data trace in an ensemble was filtered to remove grating noise, interpolated to fill dropout gaps, and smoothed. Before the mean was calculated, the individual traces were shifted in time by the same small amounts found earlier to be appropriate for the shorter (191-msec) versions of the data. Finally, the 80 mean profiles were themselves shifted in time (typically by about 5 to 10 msec) to align the cursor times $<t_{cu}>$ with the value measured on the axis of symmetry.*

8.2 The Final Data Array

According to the plan outlined in Section 6.1, the next step in data processing was to transform the mean-velocity data to similarity variables U and V in (ξ, η)-space. The expectation that standard contour-plotting routines would play some role suggested use of a square grid. The associated interpolation and curve-fitting operations were designed to yield not only U and V but also $\partial U/\partial\eta$, $\partial U/\partial\xi$, $\partial V/\partial\eta$, and $\partial V/\partial\xi$.

---

*The data were partially processed without this shift. The result, particularly the check of continuity corresponding to Figs. 23-25 below, was not satisfactory.

The mean-velocity profiles <u> and <v> for each ensemble describe the flow which is observed as t varies for fixed x and r. The data therefore lie along a straight line or ray through the origin in (ξ, η) coordinates, as indicated in the sketch, with time as

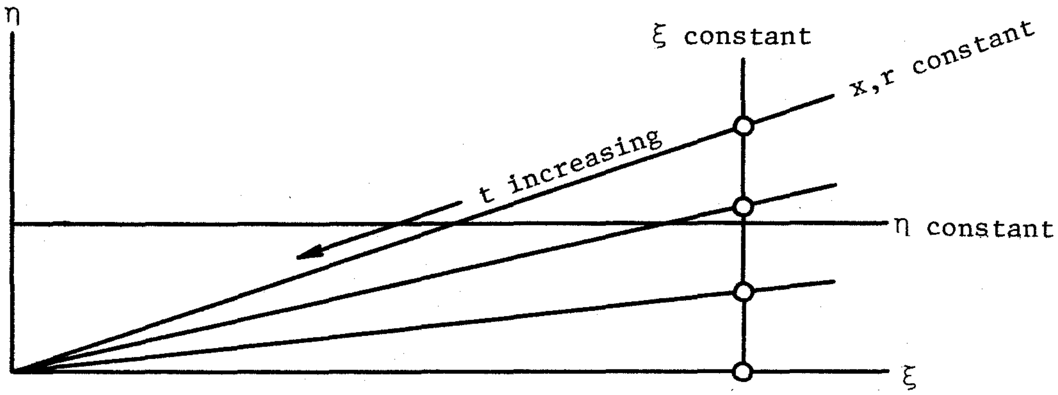

parameter along the ray. To fix the ideas, consider the axial velocity <u(t)> on a given ray. The time corresponding to the intersection of the ray with a particular grid line ξ = constant can be calculated from the first of Eqs. (30);*

$$t = \left(\frac{\rho}{I}\right)\left(\frac{x}{\xi}\right)^4 \qquad (32)$$

Given t, the axial velocity <u> can be interpolated from the file constructed during the data preparation of Section 8.1, and the velocity U can be calculated from the first of Eqs. (31);

$$U = u\left(\frac{\rho}{I}\right)^{\frac{1}{4}} t^{3/4} \qquad (33)$$

The value of η at the intersection is given by $\eta/\xi = r/x$.

---

*Here and in what follows, the apparent origin is suppressed, in order to simplify the notation: i.e., $t - t_0$ is written as t, and $x - x_0$ is written as x. In the same spirit, <u> and <v> are written as u and v, respectively.

When all of the 80 ensembles have been treated in this way, there exists along each grid line ξ = constant a population of 80 values for $U(\eta)$ (cf. Fig. 19(a), where the variable is $<u_{cu}>$). Let these be fitted by a cubic polynomial, in the manner described in Section 7.4, with the fit centered on each of the various grid lines η = constant in turn. The result is a smooth set of values for $U(\eta)$ at the grid intersections, with a set of values for the derivative $\partial U/\partial\eta$ at the same grid intersections as a byproduct.

The same procedure can be carried out for the radial-velocity component $<v>$ to obtain V and $\partial V/\partial\eta$.*

In principle, the procedure could also be used, after interchanging the roles of ξ and η, to obtain $\partial U/\partial\xi$, $\partial V/\partial\xi$, and redundant values for U and V. For a square grid, however, intersections of a ray with the grid lines η = constant are much too widely spaced to be suitable for the fitting operation. The key to proper processing then becomes the fact that the time derivative is nearly equivalent to the ξ-derivative. For example, write

$$u = \left(\frac{I}{\rho}\right)^{\frac{1}{4}} t^{-3/4} U \qquad (34)$$

from which

$$\frac{\partial u}{\partial t} = \left(\frac{I}{\rho}\right)^{\frac{1}{4}} t^{-3/4} \left(\frac{\partial U}{\partial t} - \frac{3}{4}\frac{U}{t}\right) \qquad (35)$$

But

$$\frac{\partial U}{\partial t} = -\frac{1}{4}\left(\frac{\xi}{t}\frac{\partial U}{\partial \xi} + \frac{\eta}{t}\frac{\partial U}{\partial \eta}\right) \qquad (36)$$

---

*But see the footnote on p. 63.

Hence

$$\frac{\partial u}{\partial t} = -\left(\frac{I}{\rho}\right)^{\frac{1}{4}} \frac{t^{-7/4}}{4} \left(3U + \xi \frac{\partial U}{\partial \xi} + \eta \frac{\partial U}{\partial \eta}\right) \tag{37}$$

and finally

$$\frac{\partial U}{\partial \xi} = -4 \frac{t^2}{x} \frac{\partial u}{\partial t} - \frac{\eta}{\xi} \left(\frac{\partial U}{\partial \eta} + 3 \frac{U}{\eta}\right) \tag{38}$$

Because $\partial U/\partial \xi$ and $\partial U/\partial \eta$ are of the same order, while η/ξ is not greater than about 0.02, the right-hand side of the last equation is dominated by the first term. Use can be made of the fact that $u(t)$ is known at equally-spaced points in time, so that the derivative can be calculated from a standard formula. In an obvious notation,

$$\frac{\partial u}{\partial t} = \frac{u(t - 2h) - 8u(t - h) + 8u(t + h) - u(t + 2h)}{12h} \tag{39}$$

This derivative again has to be interpolated in t and fitted on ξ = constant to obtain values for $\partial u/\partial t$ at the grid intersections, whereupon all of the quantities on the right-hand side of Eq. (38) are known, and $\partial U/\partial \xi$ follows.

The same development holds for V, except that Eq. (38) is replaced by

$$\frac{\partial V}{\partial \xi} = -4 \frac{t^2}{x} \frac{\partial v}{\partial t} - \frac{\eta}{\xi} \left(\frac{\partial V}{\partial \eta} + 3 \frac{V}{\eta}\right) \tag{40}$$

Recall that the numerical value of I/ρ was given in Section 5.1 as 2374 cm/sec. The numerical value of x for the present data is 35 + 145 = 180 cm. Given that t is a little less than one second when the vortex-ring core passes the measurement station, the region of greatest interest will lie near $\xi \sim 25$ (cf. Fig. 17).

The six quantities U, V, $\partial U/\partial\eta$, $\partial V/\partial\eta$, $\partial U/\partial\xi$, $\partial V/\partial\xi$ were eventually calculated on a grid defined by $\eta = 0(0.005)0.470$ and $\xi = 24.195(0.005)25.845$. There are 95 grid points in the η-direction and 331 grid points in the ξ-direction, or 31445 grid points in the total array. Not all of these grid points are real, because the flow was not observed outside the triangle in (ξ, η)-space defined by the outermost ray in the sketch. Note that the grid increment of 0.005 in ξ corresponds to a time interval of roughly 1 msec. Such high resolution is essential in and near the vortex core to resolve large gradients in this region. Elsewhere in the flow such high resolution is not essential, but is maintained to accommodate the requirements of the contour-plotting routine.

8.3 Continuity and Vorticity

Contour plots* have been made for the two components of mean velocity, as shown in Figs. 21 and 22, and for several quantities which involve derivatives of the mean velocity. Figures 23 and 24 indicate the magnitude of the two terms $\partial U/\partial\xi$ and $\partial\eta V/\eta\partial\eta$ in the continuity equation in similarity variables;

$$\frac{\partial U}{\partial\xi} + \frac{1}{\eta}\frac{\partial\eta V}{\partial\eta} = 0 \qquad (41)$$

---

*The assistance of Mr. Thomas Rösgen in making these plots is gratefully acknowledged.

Fig. 25 shows the sum, which is close enough to zero to inspire some confidence in values obtained for other quantities involving spatial derivatives.[†]

One such quantity is the azimuthal vorticity ζ, which is defined in cylindrical polar coordinates as

$$\zeta = \frac{\partial v}{\partial x} - \frac{\partial u}{\partial r} \tag{42}$$

In similarity variables this can be written

$$\Omega = \zeta t = \frac{\partial V}{\partial \xi} - \frac{\partial U}{\partial \eta} \tag{43}$$

Contours for the two terms $\partial V/\partial\xi$ and $\partial U/\partial\eta$ are shown in Figs. 26 and 27, and the difference Ω is shown in Fig. 28. The vorticity is strongly concentrated in the core, whose dimension (based on the contour representing half the peak value) is about ten percent of the ring diameter. The vorticity in the near wake is relatively small.

8.4 Particle Paths

The study of particle paths for the purpose of identifying the main structural properties of a turbulent vortex ring, particularly entrainment, was begun by Woodward (1959). The present analysis,

---

[†] There is a small error in the derivative $\partial\eta V/\eta\partial\eta$ close to the axis in Figs. 24 and 25. The program written for the curve-fitting operation described in Section 7.4 was developed and tested for the variable $\langle u\rangle$, and was later applied to $\langle v\rangle$ without thinking. The program used reflection to enforce symmetry, and therefore incorporated the correct conditions $\langle u\rangle = \langle u\rangle_p \neq 0$ and $\partial\langle u\rangle/\partial r = 0$ on the axis. For the $\langle v\rangle$-component, however, the corresponding conditions should be $\langle v\rangle = 0$, $\partial\langle v\rangle/\partial r = -\frac{1}{2}\partial\langle u\rangle/\partial x \neq 0$ on the axis. The error occurs only for relatively small values of r, as is evident in Fig. 19(b), and was not judged to be serious enough to mandate the substantial effort required for correction.

however, will follow the more sophisticated example set by Cantwell et al. (1978) in their work on the turbulent spot. The properties of similarity and axial symmetry make the turbulent vortex ring a good candidate for application of these powerful topological techniques.

Particle paths in unsteady axisymmetric flow are defined by the two simultaneous equations

$$\begin{aligned} \frac{dx}{dt} &= u[x(t), r(t), t] \\ \frac{dr}{dt} &= v[x(t), r(t), t] \end{aligned} \tag{44}$$

The velocity components in similarity coordinates have already been defined by Eqs. (30) - (31) of Section 6.1. From the definitions (30), in particular, it follows that

$$\left.\begin{aligned} \frac{dx}{dt} &= \left(\frac{I}{\rho}\right)^{\frac{1}{4}} t^{\frac{1}{4}} \left(\frac{d\xi}{dt} + \frac{1}{4}\frac{\xi}{t}\right) \\ \frac{dr}{dt} &= \left(\frac{I}{\rho}\right)^{\frac{1}{4}} t^{\frac{1}{4}} \left(\frac{d\eta}{dt} + \frac{1}{4}\frac{\eta}{t}\right) \end{aligned}\right\} \tag{45}$$

Substitution of u and v from Eqs. (31) into Eqs. (44), and some algebra, yield the elegantly simple relationships

$$\left.\begin{aligned} \frac{d\xi}{d\tau} &= U - \frac{\xi}{4} \\ \frac{d\eta}{d\tau} &= V - \frac{\eta}{4} \end{aligned}\right\} \tag{46}$$

where $\tau = \ell n\ t$.

Except for the factor 1/4, which comes from the exponent of t in the definitions of ξ and η, these are the same equations obtained by Cantwell et al. Division of one equation by the other gives an equation

$$\frac{d\eta}{d\xi} = \frac{V(\xi, \eta) - \eta/4}{U(\xi, \eta) - \xi/4} \tag{47}$$

which (at least in principle) can be integrated to find the mean particle paths. Note that Eqs. (46) are autonomous; i.e., the right-hand sides do not depend explicitly on the time. Consequently, while the position of a particle along its trajectory in (ξ, η)-space varies with time, the trajectory itself is independent of time. Equations (46) can be interpreted as a zoom transformation, with the observer receding out of the plane of the flow at a rate which freezes the apparent size of the turbulent structure.

In Fig. 29, short symmetrical line segments have been drawn through the various grid intersections to show the slopes calculated from Eq. (47) (for clarity, only every fourth grid point is used). Critical points are defined by the condition $d\eta/d\xi = 0/0$, and therefore lie at intersections of the two curves $U = \xi/4$, $V = \eta/4$. When these curves are calculated, two saddle points are found at $(\xi, \eta) = 24.847, 0)$ and at $(25.208, 0)$, and two foci are found at $(\xi, \eta) = (25.032, 0.213)$. These critical points are indicated by small filled circles.

In the work by Cantwell et al., particle paths were constructed (i.e., Eq. (47) was integrated) essentially by eye, with the aid of a figure like Fig. 29. In the present work, an attempt has been made to carry out a formal numerical intergration. In principle, a given particle path enters a particular square cell of the grid at a known point on one of the four equal sides. Linear interpolation in $d\eta/d\xi$ between the two nearest grid intersections can be used to determine the approximate slope of the particle path within the cell. As the path leaves one cell it enters another, and the procedure can be repeated. However, this procedure is not easy to implement, and no reliable results have been obtained to date.

IX. DISCUSSION

A major obstacle to experimental study of turbulent vortex rings in inherent in the dynamics of the phenomenon. Irregular shedding of vorticity from the main vortex body into the wake (cf. Fig. 1(b)) causes substantial dispersion in both space and time for the trajectories of individual vortex rings. Quantitative data at various locations downstream of the orifice of a vortex-ring generator have previously been reported, mostly for laminar flow, by Akhmetov and Kisarov (1966)(1), Johnson (1970(2), Sullivan et al. (1973)(3), Sallet and Widmayer (1974)(4), Kovasznay et al. (1974)(5), Didden (1977)(6), and Maxworthy (1977)(7). Whenever the flow in question is turbulent, serious problems with dispersion are either reported explicitly or can be deduced from the nature of the published data. Except for data on celerity and a few estimates of the ratio of core diameter to ring diameter, no useful quantitative information about turbulent structure was obtained in any of the experiments just cited. In most cases, moreover, the results are obscured by effects of probe interference and/or directional ambiguity in the measurements of velocity, whether

---

(1) Laminar ring; HWA data for $u(r, t)$, $v(r, t)$ at $x/D_0 = 5.45$.

(2) Turbulent ring; HWA data for $u(r, t)$ at $x/D_0 = 9, 12, 18$.

(3) Laminar ring; unbiased LDV data for $u(r, t)$, $v(r, t)$ at unspecified station.

(4) Laminar or turbulent ring; HWA data for $u(t)$ at $r = 0$ or $D/2$ at $x/D_0 = 8$ to 60.

(5) Turbulent puff; HWA data for $u(r, t)$ at $x/D_0 = 1$ to 10.

(6) Laminar ring; unbiased LDV data for $u(r, t)$, $v(r, t)$ at $x/D_0 = 3$.

(7) Laminar or turbulent ring; unbiased LDV data for $u(r, t)$, $v(r, t)$ at $x/D_0 = 2.5, 14$.

the instrumentation used was the hot-wire anemometer or the laser-Doppler velocimeter.

One important contribution of the present research is the development of methods for coping with the problem of dispersion. The problem was appreciated from the beginning, and great care was exercised in designing, fabricating, and maintaining the vortex-ring generator. Measurements of $u(t)$ on the axis of symmetry showed acceptable repeatability, as did visual observations of the piston motion, and the fluid-mechanical axis of symmetry was found to be almost identical to the geometric axis of symmetry. The use of laser-Doppler instrumentation with frequency bias eliminated probe interference and directional ambiguity from the measurements of velocity. The real key to solution of the dispersion problem, however, was the simultaneous measurement of $u(t)$ and $v(t)$. The resulting information made possible a two-component technique of pattern recognition which produced the desired mean-velocity data from relatively small ensembles. In a typical such ensemble, data may be included from as many as 8 or 9 of the measuring stations shown in Fig. 12.

Another important contribution is verification of the concept of similarity for the turbulent vortex ring. This concept has been exploited to develop a quantitative picture of the mean flow in non-steady similarity coordinates. At the stage so far reached in the analysis, data are available for the mean velocity field and its gradients on a square grid in similarity coordinates. When particle paths are determined using a powerful topological method first applied to a different problem by Cantwell, Coles and Dimotakis (1978), there are no surprises. What may be surprising is the extremely slow growth rate found for the turbulent vortex ring compared, for example, to the turbulent puff or the turbulent thermal. Another unexpected property of the similarity formulation per se is the requirement that the circulation Γ for a given ring must decrease like $(t - t_0)^{-\frac{1}{2}}$, rather than remain constant. This property needs to be tested and explained before the concept of similarity can be accepted as proved.

A dynamical description of the turbulent vortex-ring has not been achieved in the work so far. This description requires extraction from the raw data of information about turbulence level, turbulence production, and entrainment. Because Fig. 28 shows the mean vorticity to be strongly concentrated near the vortex core and almost zero elsewhere, there is a possibility that turbulence may be incidental rather than central to the dynamics. In any event, an essential element is the location of the laminar-turbulent interface which bounds the body of fluid inside the vortex ring. It may be that the position of this interface relative to the particle paths will show de-entrainment at the rear of the ring, thus accounting for the observed strong discharge of dyed fluid into the wake (cf. Fig. 1(b)). In dealing with turbulence, however, one obstacle to progress is a problem of definition. It is not clear whether variation from ring to ring of the large-scale part of the motion, up to and including what has been called dispersion, should be counted as simple distortion (playing no role in mean transport) or whether it should be counted as part of the turbulence. An example of the problem has already been encountered in Fig. 14. Another observer might or might not consider the mean curve for <u(t)> in this figure to be a good representation of the experimental data.

The photograph in Fig. 30 concludes this discussion by suggesting another important phenomenon in need of investigation. The figure shows a group of eight small vortex rings which were produced in rapid succession by the vortex-ring generator described in Section 3.2 above. The various rings participate in what can only be described as collisions, during which the individual trajectories are deflected through quite large angles. Because the growth rate of a single vortex ring (at least a ring with a thin core) is much slower than the growth rate of a turbulent jet, such interactions may be part of the mechanism of growth and entrainment in jet flows and perhaps other flows as well.

APPENDIX. DESIGN OF THE DIFFRACTION GRATINGS

A diffraction grating imposes on an incident light wave a spatially periodic variation of amplitude or phase or both. The analysis which follows is based on an approximation called Fraunhofer diffraction, which applies when the optical distance from a point in the observation plane to a point in the diffraction plane (the grating) depend linearly on the coordinates of the latter point. An equivalent statement is that both the light source and the observation point must be far from the grating.

Consider a grating plane normal to the optical or z axis. The electromagnetic field $\vec{E}(\vec{r})$ at the observation point $P(\vec{r})$ is described (Klein 1970, p. 333) by the expression

$$\vec{E}(\vec{r}) = \frac{i}{\lambda} \vec{E}(0) \frac{e^{ikR_0'}}{R_0'} \iint_{-\infty}^{\infty} t(x', y')\, e^{-2\pi i(ux' + vy')} dx'dy' \tag{A1}$$

where

$\vec{E}(0)$ is the field incident on the grating,

$\vec{E}(\vec{r})$ is the field at the point of observation,

R_0' is the distance from the grating to the point of observation, and

$t(x', y')$ is the two-dimensional transmission function relating the transmitted field $\vec{E}_t$ to the incident field $\vec{E}_i$; i.e.,

$$\vec{E}_t(\vec{r}\,') = t(\vec{r}\,')\, \vec{E}_i(\vec{r}\,'), \qquad \text{with } \vec{r}\,' = (x', y') \tag{A2}$$

In Eq. (A1), $u = -\alpha/\lambda$ and $v = \beta/\lambda$, where α and β are the direction cosines of the observation point with respect to the origin in the plane of the grating, and λ is the wave length of the incident light.

The transmission function is taken in the form

$$t(\vec{r}') = |t(\vec{r}')| e^{i\psi(\vec{r}')} \tag{A3}$$

Losses caused by reflection and absorption of the incident light are represented by values of $|t(\vec{r}')| < 1$. Phase changes of the incident light are described by $\psi(\vec{r}')$. The integral in Eq. (A1) is the two-dimensional Fourier transform of the transmission function. If the transmission function is (say) a function of x' only, the field at $P(\vec{r}')$ is described by

$$\vec{E}(\vec{r}) = \frac{i}{\lambda} \vec{E}(0) \frac{e^{-ikR_0'}}{R_0'} \delta(\beta)\hat{t}(u) \tag{A4}$$

where

$$\hat{t}(u) = \int_{-\infty}^{\infty} t(x')e^{-2\pi iux'} dx' \tag{A5}$$

The delta function $\delta(\beta)$ emphasizes the fact that the diffraction is one-dimensional and is confined to the plane $\beta = 0$.

The phase grating is characterized by a transmission function

$$t(x') = e^{i\psi(x')} \tag{A6}$$

where the amplitude transmission function is unity and ψ is a periodic function of x'. The grating is a transparent plate with periodically varying thickness $g(x')$. The phase change imposed on the incident light (referred to the case with no plate) is then

$$\psi(x') = \frac{2\pi}{\lambda}(n - 1)g(x') \qquad \text{(A7)}$$

where n is the index of refraction. One useful form of the phase grating is obtained when $g(x')$ is a square wave, as shown in the sketch. This form is realized by etching parallel grooves of specified

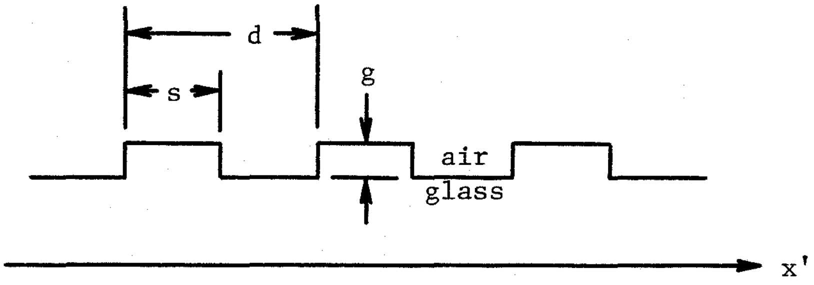

width d-s, depth g and spacing d in a glass substrate. The phase variation is given by

$$\left.\begin{aligned} \psi &= \frac{\pi}{2}M \quad \text{for} \quad -\frac{s}{2} < x' < \frac{s}{2} \\ \psi &= -\frac{\pi}{2}M \quad \text{for} \quad \frac{s}{2} < x' < d - \frac{s}{2} \end{aligned}\right\} \qquad \text{(A8)}$$

where

$$M = 2(n - 1)\frac{g}{\lambda} \qquad \text{(A9)}$$

Note that $t(x') = 1$ when $g = 0$ and also when $n = 1$.

For an infinite grating, $t(x')$ is periodic from $-\infty$ to ∞. The Fourier transform of a periodic function $t(x')$ with period d is

$$\hat{t}(u) = \sum_{m=-\infty}^{\infty} \frac{1}{d}\,\delta(u - \frac{m}{d}) \int_{-d/2}^{d/2} t(x')e^{-2\pi iux'}\,dx' \qquad \text{(A10)}$$

and contains only discrete peaks of order m, as indicated by the delta function. Since u is a direction cosine in normalized form $(u = -\alpha/\lambda)$, the directions $u = m/d$ are discrete directions in the plane $\beta = 0$.

After substitution for $t(x')$ and some algebra, Eq. (A10) becomes

$$\hat{t}(u) = \sum_{m=-\infty}^{\infty} \frac{1}{d}\, \delta\left(u - \frac{m}{d}\right) \left\{ \frac{2i}{\pi u} \sin(\pi u s)\, \sin\left(\frac{\pi}{2} M\right) + \frac{e^{-i\frac{\pi}{2}M}}{\pi u} \sin(\pi u d) \right\} \tag{A11}$$

and the field for a given direction $u = m/d$ is

$$\vec{E}^{(m)}(\vec{r}) = \frac{i}{\lambda}\, \vec{E}(0)\, \frac{e^{-ikR_0'}}{R_0'}\, \delta(\beta)\, \frac{2is}{d} \sin\left(\frac{\pi}{2} M\right) \frac{\sin\left(\frac{\pi m s}{d}\right)}{\frac{\pi m s}{d}} \tag{A12}$$

In particular,

$$\vec{E}^{(0)}(\vec{r}) = \vec{E}(0)\, \frac{e^{-ikR_0'}}{R_0'}\, \delta(\beta)\, \frac{1}{d} \left[s e^{i\frac{\pi}{2}M} + (d - s) e^{-i\frac{\pi}{2}M} \right] \tag{A13}$$

These expressions describe the field associated with the various diffracted orders of the incident light $(m = 0, \pm 1, \pm 2, \ldots)$.

When $t(x') \equiv 1$ (no grating), the field of the incident light at the point of observation will be

$$\vec{E}(\vec{r}) = \frac{i}{\lambda}\, \vec{E}(0)\, \frac{e^{ikR_0'}}{R_0'}\, \delta(\beta)\, \delta(\alpha) \tag{A14}$$

with an intensity

$$I = |\vec{E}(\vec{r})|^2 = \frac{|\vec{E}(0)|^2}{\lambda^2 R_0'^2} \tag{A15}$$

Define the relative intensity (or diffraction efficiency) for the various orders as $\eta^{(m)} = |\vec{E}^{(m)}(\vec{r})|^2/I$; thus

$$\left.\begin{aligned} \eta^{(0)} &= 1 + 2\,\frac{s}{d}\left(\frac{s}{d} - 1\right)(1 - \cos \pi M) \\ \eta^{(m)} &= 2\,\frac{s}{d}\,\sin^2\left(\frac{\pi}{2} M\right) \frac{\sin^2\left(\frac{\pi m s}{d}\right)}{\left(\frac{\pi m s}{d}\right)^2} \end{aligned}\right\} \qquad \text{(A16)}$$

The diffracted orders form angles $\theta^{(m)}$ with respect to the incident beam, where

$$\theta^{(m)} = \text{arc sin}\left(\frac{\lambda}{d}\, m\right) \qquad \text{(A17)}$$

These results agree with results obtained by Sirohi and Blume (1975) and Oldengarm et al. (1976). The expression used for M by Oldengarm et al., however, does not specify zero phase change when $n = 1$.

The relative intensities $\eta^{(m)}$ depend on the grating geometry (s, d, g), the grating material (n), and the wavelength of the incident light (λ). Particular combinations of these parameters can maximize the intensity in some of the diffracted orders or cause some orders to disappear altogether. For example,

(a) $\frac{s}{d} = \frac{1}{2}$, $M = 1$

$\eta^{(0)} = 0$ (no energy in zero order)

$\eta^{(\pm 1)} = 0.405$ (energy concentrated in first order)

$\eta^{(\pm 2)} = \eta^{(\pm 4)} = \ldots = 0$ (no energy in even orders)

(b) $\frac{s}{d} = \frac{1}{4}$, $M = 1$ (or $\frac{s}{d} = \frac{3}{4}$, $M = 3$)

$\eta^{(0)} = 0.25$

$\eta^{(\pm 1)} = 0.202$

$\eta^{(\pm 2)} = 0.101$ (energy concentrated in 2nd order)

If the grating is moving with a constant linear velcoity U in the x' direction, the diffraction pattern does not change. However, the frequency in each of the diffraction directions in increased or decreased by an amount proportional to the diffraction angle and the grating velocity.

In Eq. (A1), change the variable x' to $x'' - Ut$ to obtain, in an obvious notation

$$E_f^{(m)}(\vec{r}) = \frac{i}{\lambda}\vec{E}(0)\frac{e^{-ikR_0'}}{R_0'}\, e^{2\pi iuUt}\iint_{-\infty}^{\infty} t(x'',y')e^{-2\pi i(ux'' + vy')}dx''dy'$$

$$= E^{(m)}(\vec{r})e^{2\pi iuUt} \tag{A18}$$

Hence each component of the diffracted field is multiplied by $e^{2\pi iuUt}$.

Since $u = m/d$, the frequency shift in each diffracted order is

$$f^{(m)} = uU = \frac{m}{d}U \tag{A19}$$

This frequency shift is positive in the direction of motion of the grating (positive orders m).

In this idealized analysis, the grating and the incident light beam are taken to be one-dimensional and infinite in extent. In practice, the light source is a laser beam having a finite diameter and a Guassian distribution of intensity. The number of grating lines encountered by the beam is finite, but can be made relatively large. The function $t(u)$ is then continuous, but still very strongly peaked near $u = m/d$.

REFERENCES

Akhmetov, D.G. and Kisarov, O.P. 1966 *Hydrodynamic structure of a vortex ring*. J. Appl. Mech. Techn. Phys. 7, No. 4, 87-90.

Cantwell, B., Coles, D., and Dimotakis, P. 1978 *Structure and entrainment in the plane of symmetry of a turbulent spot*. J. Fluid Mech. 87, 641-672.

Cantwell, B.J. 1979 *Coherent turbulent structures as critical points in unsteady flow*. Arch. Mechanics 31, 707-721.

Coles, D. 1981 *Prospects for useful research on coherent structure in turbulent shear flow*. To appear in Proc. Indian Nat'l. Acad. Sci.

Didden, N. 1977 *Untersuchung laminarer, instabiler Ringwirbel mittels Laser-Doppler-Anemometrie*. Diss., Univ. Göttingen; also Mitt. MPI und AVA, Göttingen, Nr. 64.

Didden, N. 1979 *On the formation of vortex rings: Rolling-up and production of circulation*. Z. f. angew. Math. u. Phys. 30, 101-116.

Grigg, H.R. and Stewart, R.W. 1963 *Turbulent diffusion in a stratified fluid*. J. Fluid Mech. 15, 174-186.

Johnson, G.M. 1970 *Researches on the propagation and decay of vortex rings*. Aerosp. Res. Labs, Wright-Patterson AFB, Rep. ARL 70-0093.

Kaplanskii, F. and Epshtein, A. 1976 *Dvizhenie i perenos tepla v turbulentnykh vikhrovykh kol'tsakh*. Izv. Akad. Nauk Estonskoi SSR 25 (Fizika-Matematika), 408-417.

Klein, M.V. 1970 "Optics." Wiley, New York.

Kovasznay, L.S.G., Fujita, H., and Lee, R.L. 1973 *Unsteady turbulent puffs*. Adv. Geophys. 18B, 253-263.

Kovasznay, L.S.G. and Lee, R.L. 1974 *Viscous and turbulent vortices*. In: "Omaggio a Carlo Ferrari," Torino, 431-447.

Liess, C. 1978 *Experimentelle Untersuchung des Lebenslaufes von Ringwirbeln*. Max-Planck-Institut für Strömungsforschung, Göttingen, Ber. 1/1978.

Lugovtsov, B.A. 1970 (title unknown) In: "Nekotorye Problemy v Matematiki i Mekhaniki," Leningrad, 182-189.

Maxworthy, T. 1974 Turbulent vortex rings. J. Fluid Mech. 64, 227-239.

Maxworthy, T. 1977 Some experimental studies of vortex rings. J. Fluid Mech. 81, 465-495.

Oldengarm, J., van Krieken, A.H., and Raterink, H.J. 1976 Development of a rotating grating and its use in laser velocimetry. In: "Proc. ISL/AGARD Workshop on Laser Anemometry" (French-German Research Institute, Saint-Louis, Rep. R 117/76), 603-615.

Oshima, K., Kovasznay, L.S.G., and Oshima, Y. 1977 Sound emission from burning puff. In: "Proc Symp. on Structure and Mechanisms of Turbulence," Vol. II (Lecture Notes in Physics, Springer, No. 76), 219-230.

Richards, J.M. 1965 Puff motions in unstratified surroundings. J. Fluid Mech. 21, 97-106.

Sallet, D.W. and Widmayer, R.S. 1974 An experimental investigation of laminar and turbulent vortex rings in air. Z. Flugwiss. 22, 207-215.

Schneider, P. 1980 Sekundärwirbelbildung bei Ringwirbeln und in Freistrahlen. Z. Flugwiss. Weltraumforsch. 4, 307-318.

Sirohi, R.S. and Blume, H. 1975 On the diffraction efficiency of synthetic binary holograms. Optica Acta 22, 943-946.

Stevenson, W.H. 1970 Optical frequency shifting by means of a rotating diffraction grating. Applied Optics 9, 649-652.

Sullivan, J.P., Widnall, S.E., and Ezekiel, S. 1973 Study of vortex rings using a laser Doppler velocimeter. AIAA J. 11, 1384-1389.

Turner, J.S. 1957 Buoyant vortex rings. Proc. Roy. Soc. London A239, 61-75.

Turner, J.S. 1964 The flow into an expanding spherical vortex. J. Fluid Mech. 18, 195-208.

Wigley, E. 1974 The application of radial diffraction gratings to laser anemometry. A.E.R.E. Harwell, Rep. AERE-R-7886.

Woodward, B. 1959 The motion in and around isolated thermals. Quart. J. Roy. Met. Soc. 85, 144-151.

FIGURES

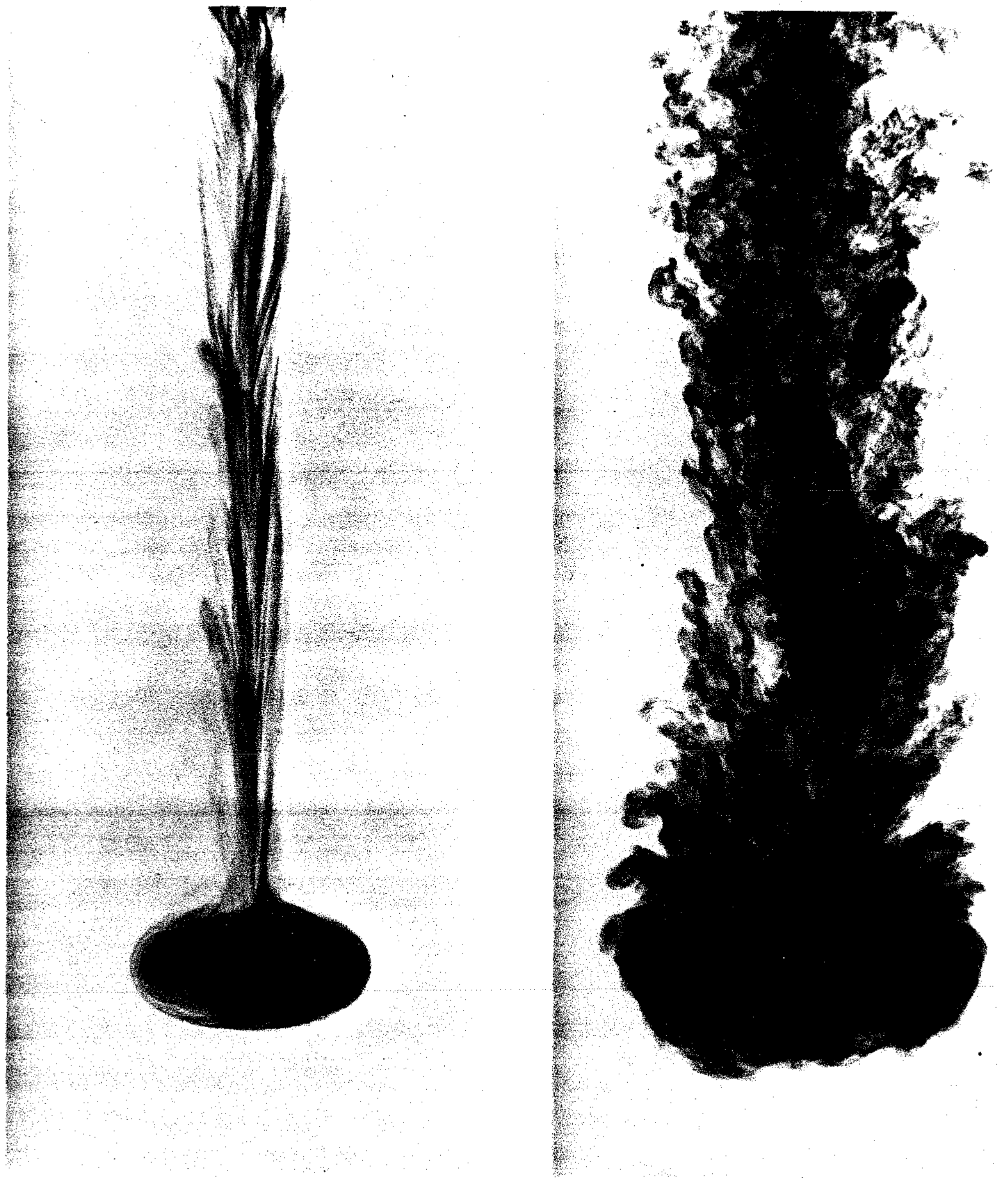

(a) (b)

Figure 1

Photographs, using dye for flow visualization, of
(a) a laminar vortex ring at $\Gamma_0/\nu \sim 7500$, and
(b) a turbulent vortex ring at $\Gamma_0/\nu \sim 27000$.
The vortex-ring generator is the one shown in Fig. 6(a).

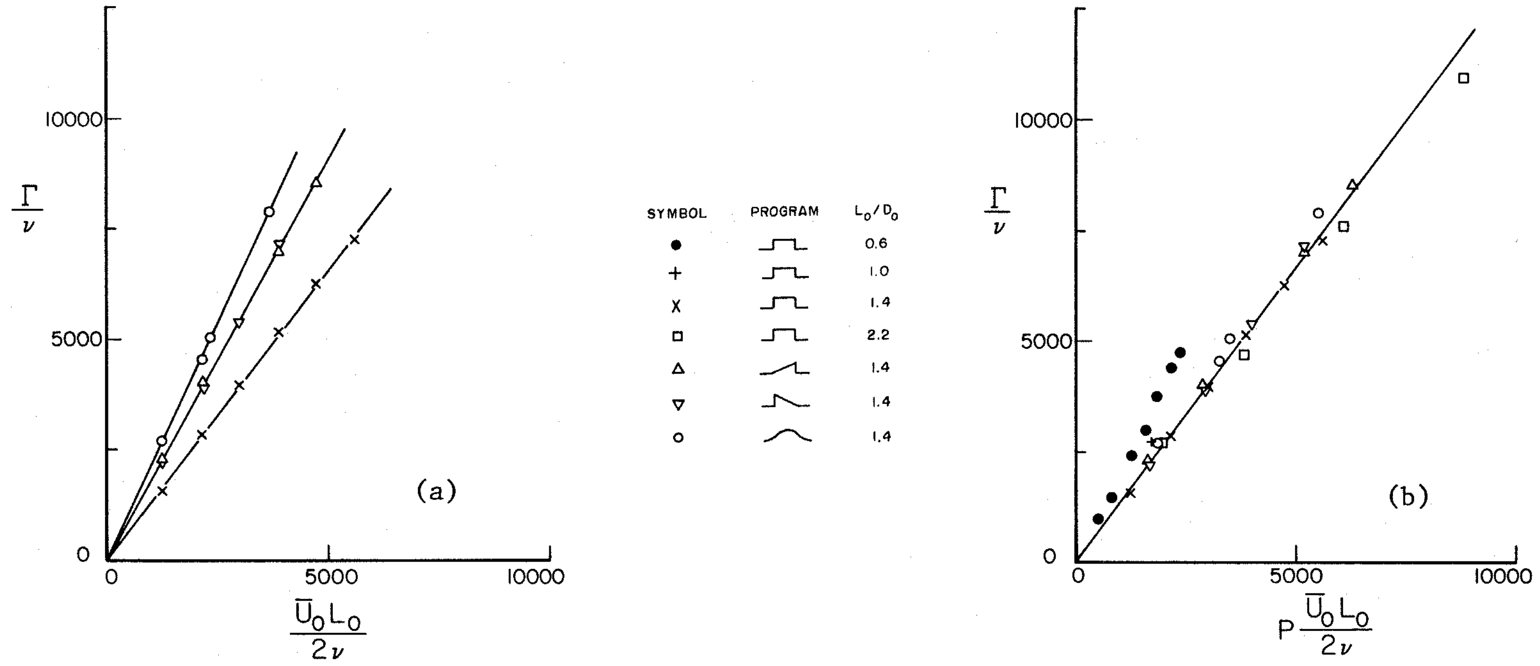

Figure 2

Didden's measurements (1977) of circulation for laminar vortex rings produced with various velocity programs, from his Fig. 16.

(a) The dimensionless raw data.

(b) The same data with the abscissa multiplied by the appropriate velocity-program factor P according to Eq. (18); also data from Didden's Fig. 18.

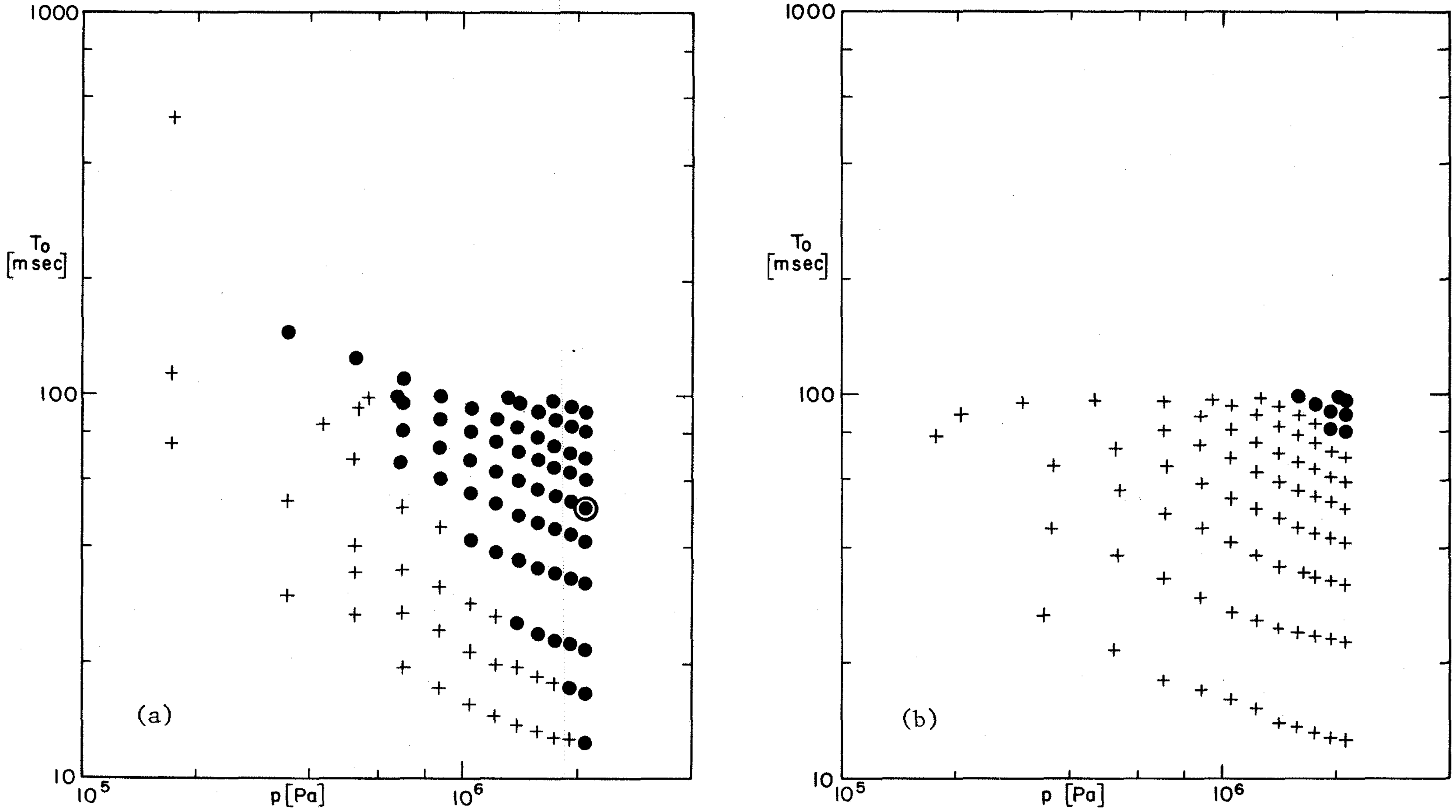

Figure 3

Raw data for the survey of transition carried out with the vortex generator of Fig. 6(b).
(a) D_0 = 1.90 cm (3/4 inch).
(b) D_0 = 2.54 cm (1 inch).
The filled circles indicate vortex rings which were turbulent when formed. The crosses indicate vortex rings which were initially laminar. The double circle shows the operating conditions for the present LDV measurements.

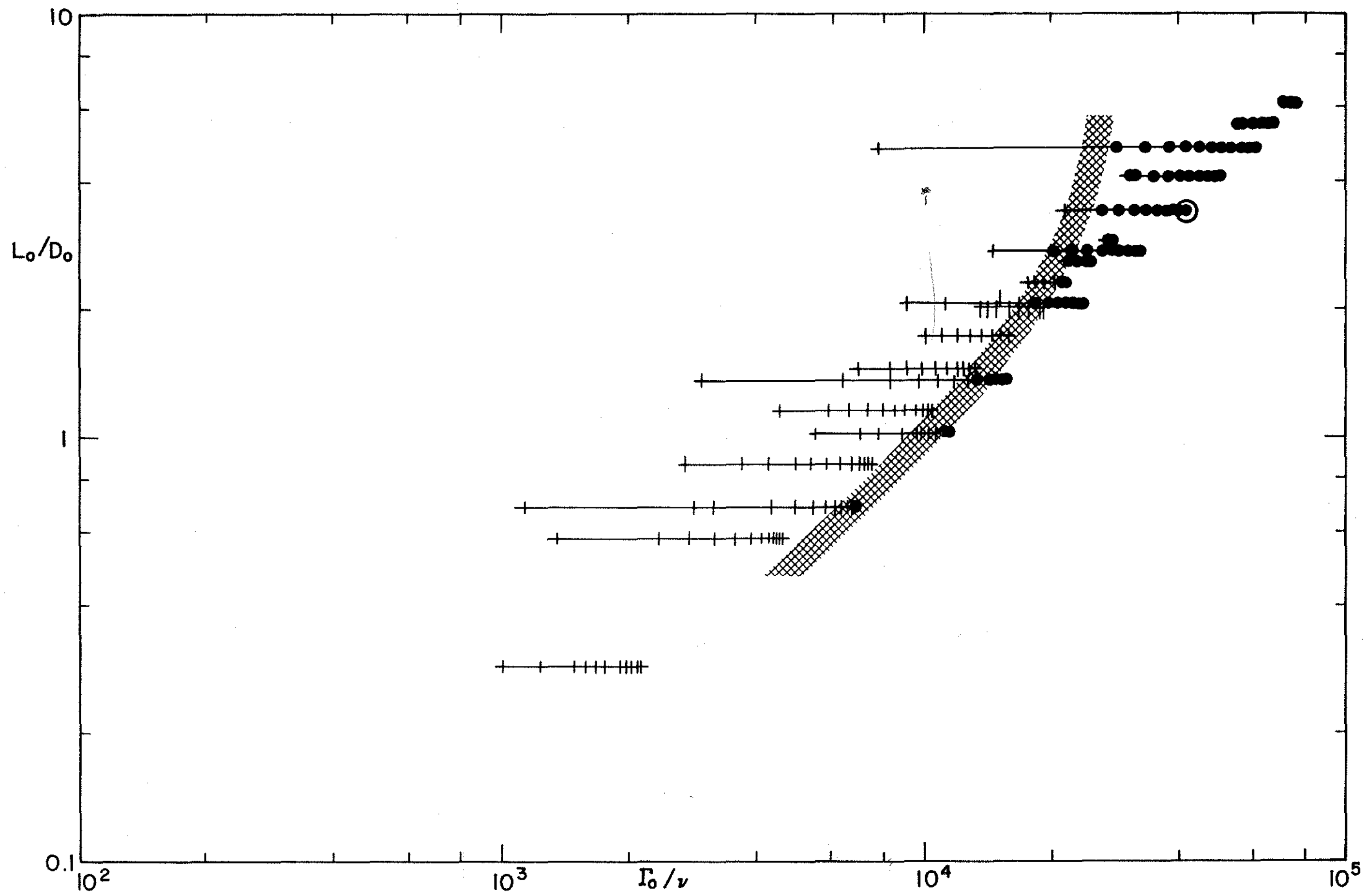

Figure 4

A transition map formed by converting the data of Fig. 3 to the dimensionless variables Γ_0/ν, L_0/D_0 of the similarity argument, assuming $P = 1$. The double circle shows the operating conditions for the present LDV measurements.

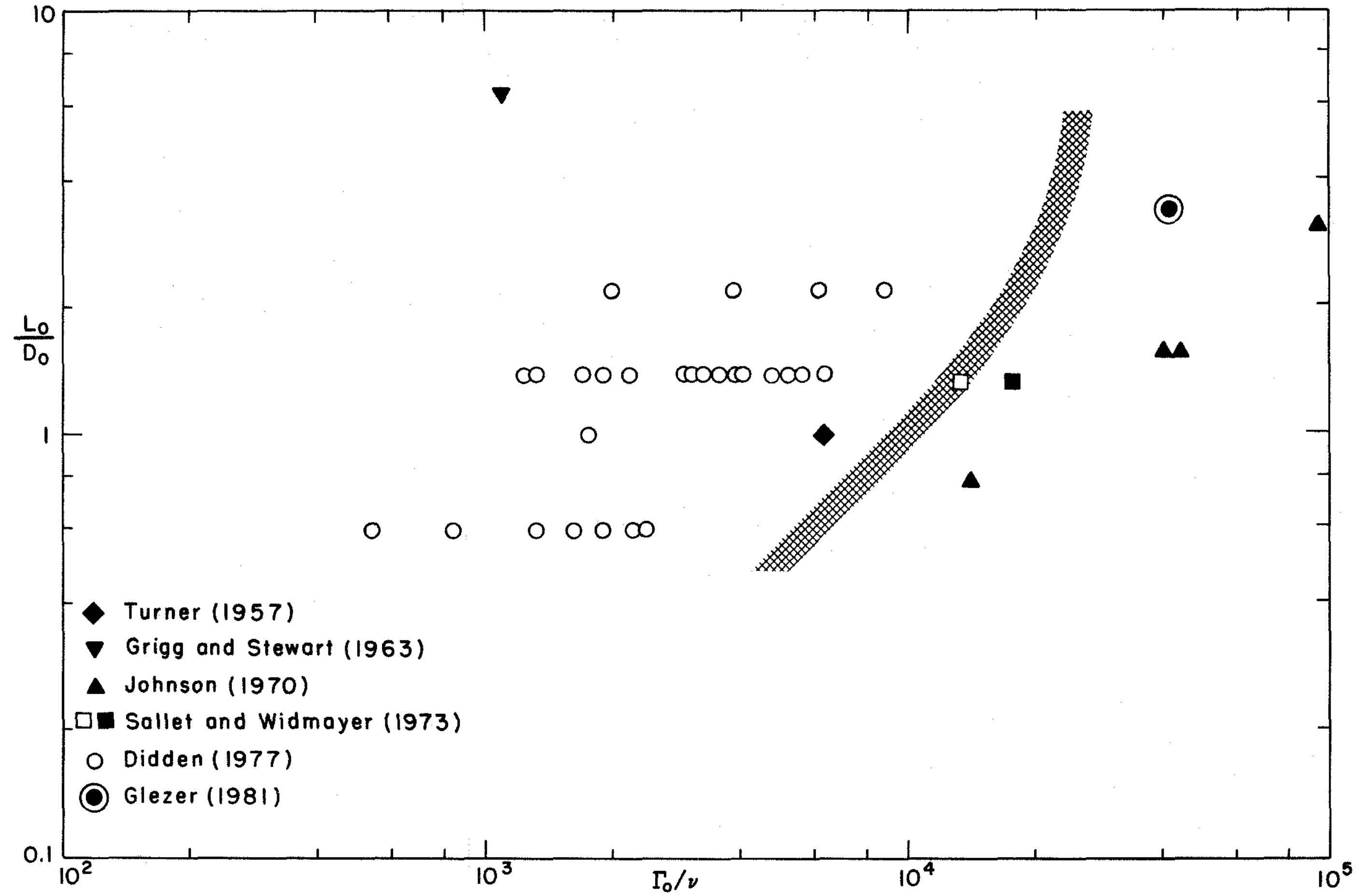

Figure 5

Flow conditions for a number of previous studies of vortex rings in the coordinates of Fig. 4. Open (filled) symbols represent laminar (turbulent) flow. The hatched contour separates initially laminar and initially turbulent vortex rings as observed during the present experiments.

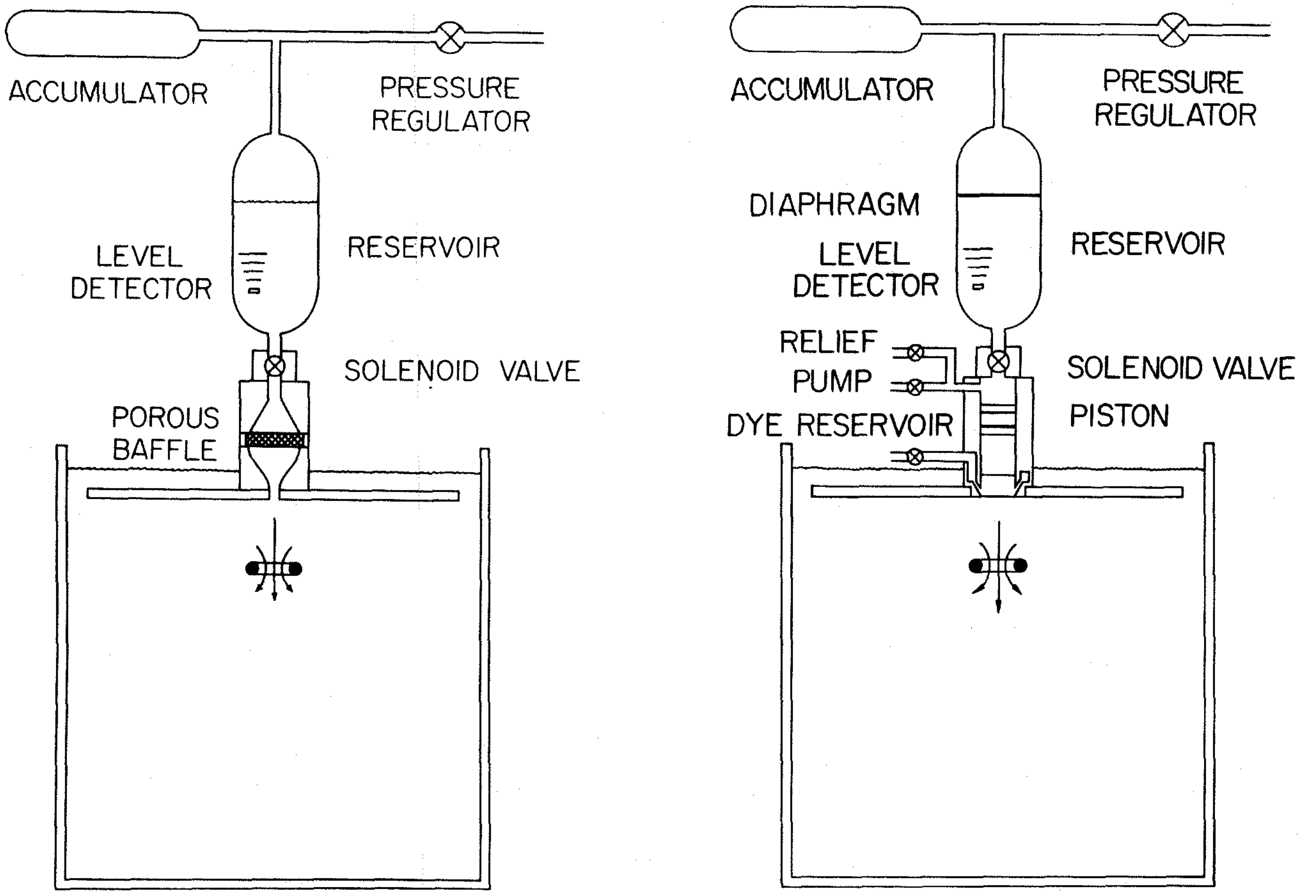

(a) (b)

Figure 6

Schematic diagrams showing the two vortex-ring generators used in the present experiments.

(a) The first vortex-ring generator (used to produce Fig. 1).
(b) The second vortex-ring generator (used to produce Fig. 4).

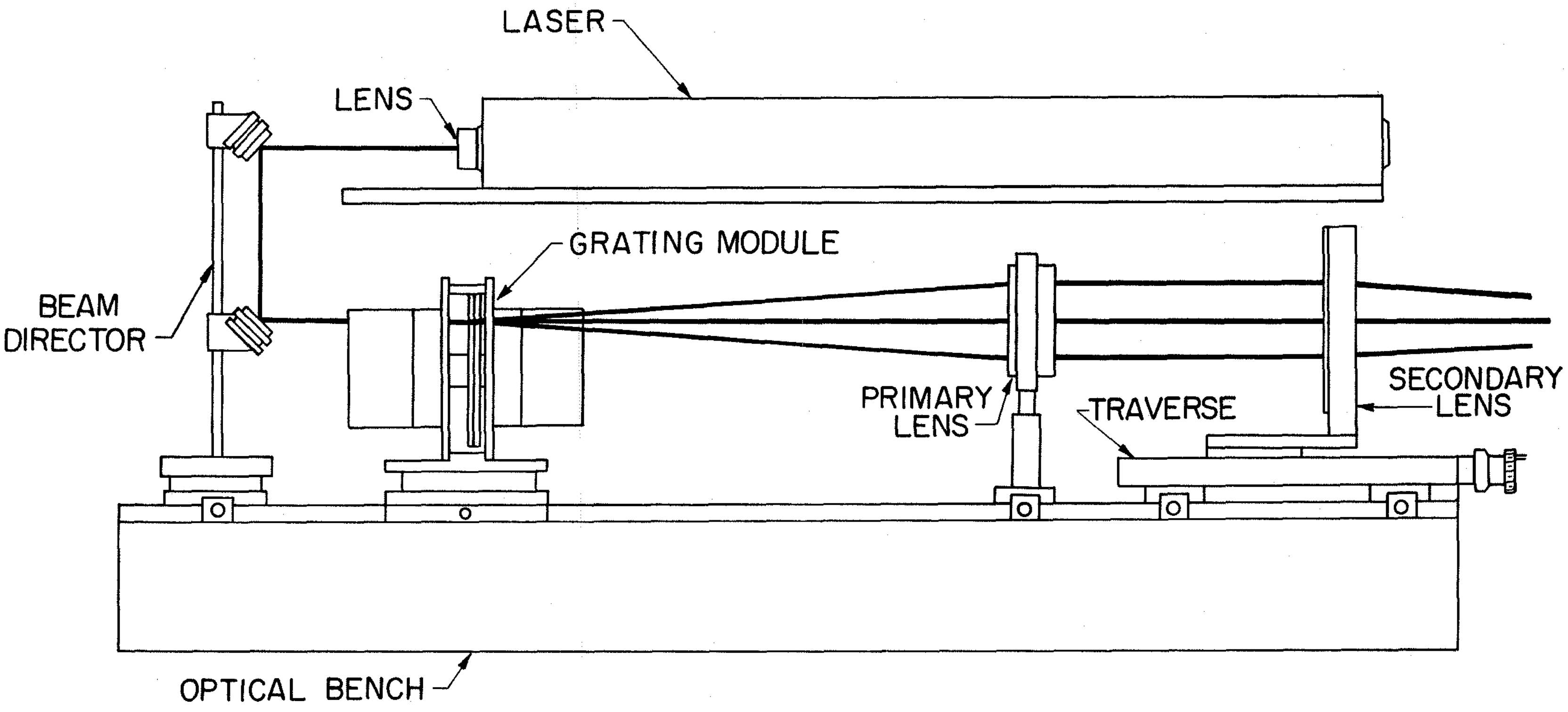

Figure 7

A side view of the two-channel LDV system. The optical bench is 120 cm long. The heavy lines indicate laser beams. The traverse at the right moves the LDV test volume along the optical axis. The distance between the grating module and the primary lens is not to scale.

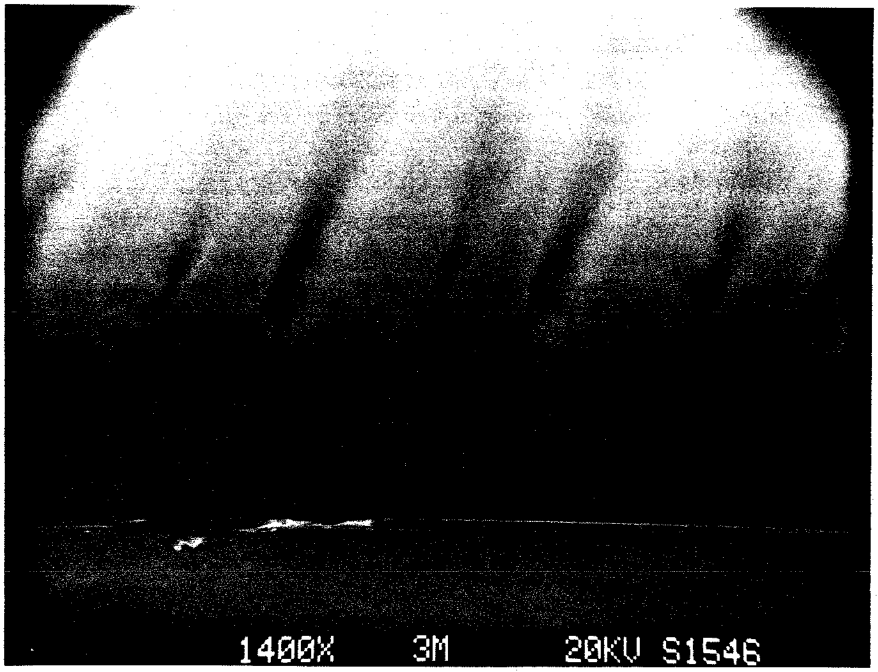

Figure 8

A scanning-electron-microscope photograph showing a cross-section through the etched grating. The magnification is 1400 times. The pitch of the grating is about 24 μm.

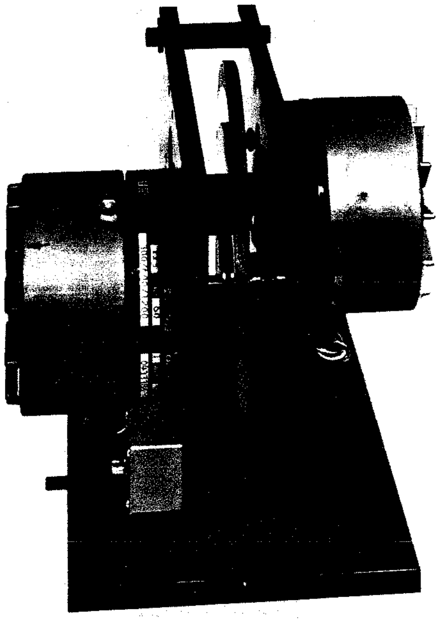

Figure 9

A photograph showing the grating module. The grating discs are 13.8 cm (5.45 inches) in diameter. The center-to-center distance between the two motors is adjustable.

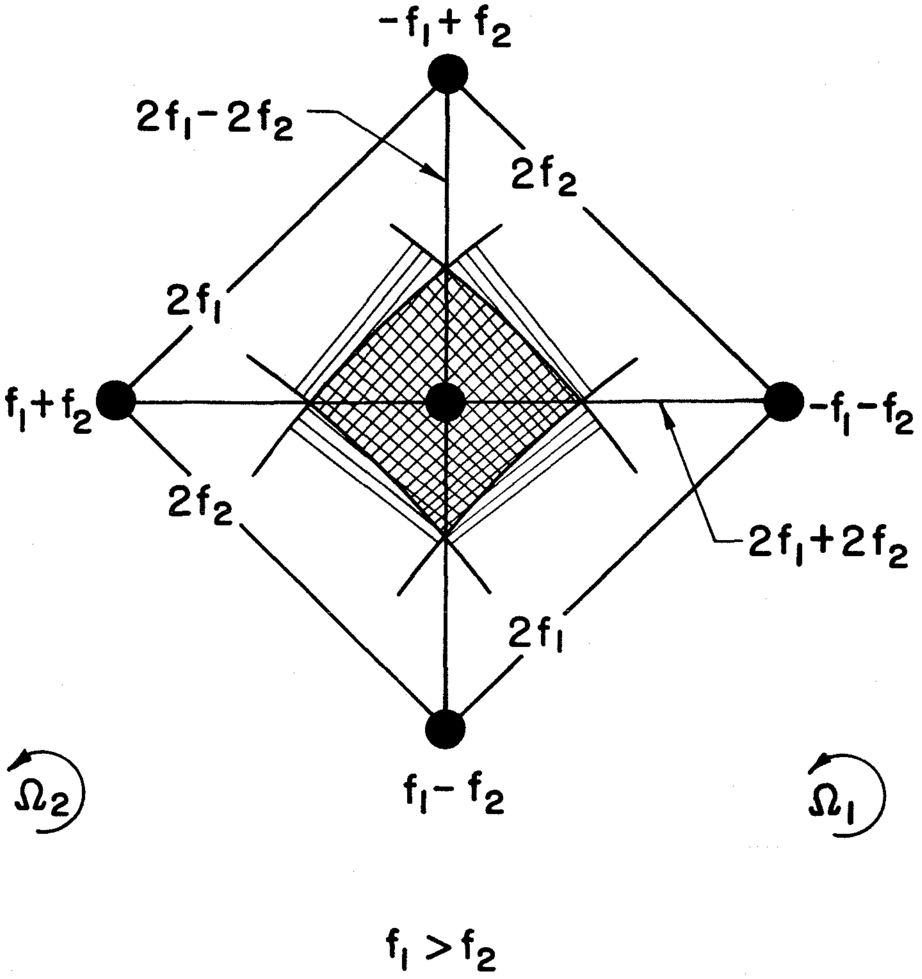

Figure 10

The beam geometry, showing interactions of the various bias frequencies for the standard two-channel LDV system with both gratings rotating.

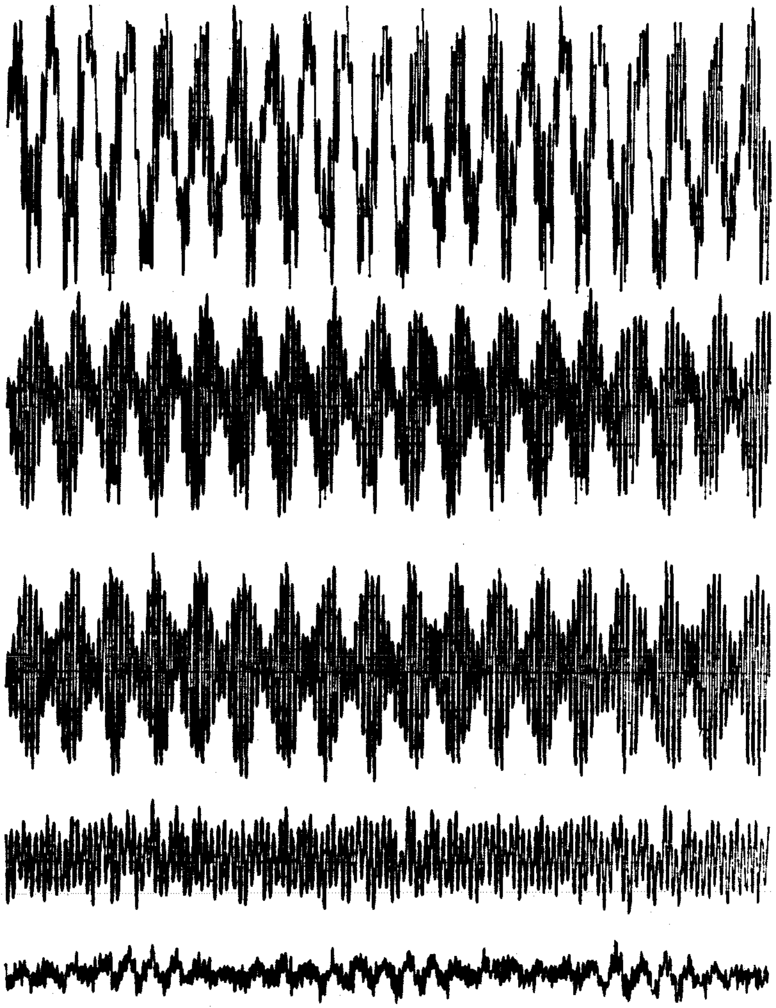

Figure 11

Grating noise and its removal, as practiced during the main experiment.

Top trace: original signal.
2nd trace: 48-msec period removed.
3rd trace: 56-msec period removed.
4th trace: 7-msec period removed.
5th trace: 8-msec period removed.

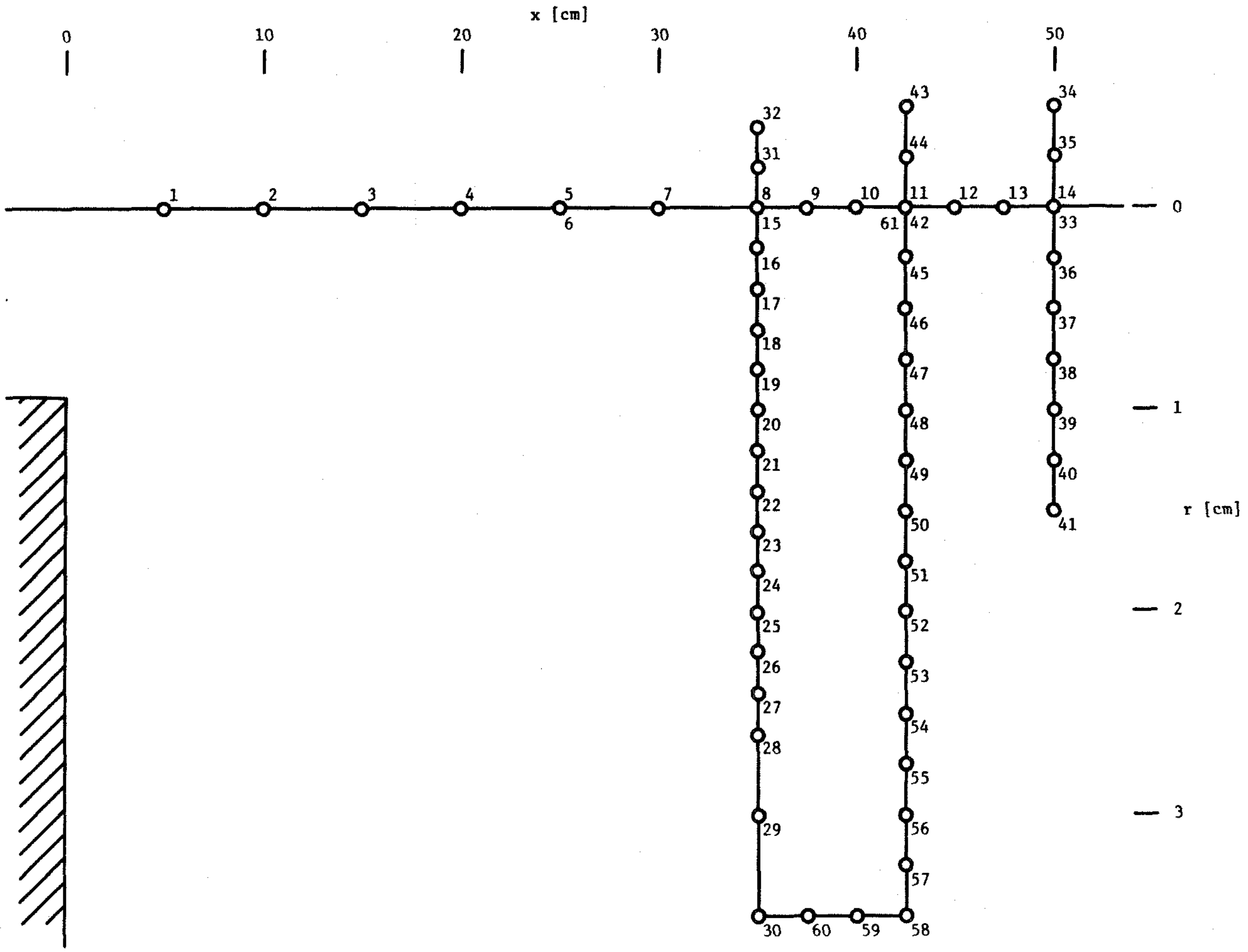

Figure 12

The location of positions where data were obtained for an ensemble of 100 vortex rings during the main experiment. The figures are file numbers. There are two double points and one triple point on the axis of symmetry.

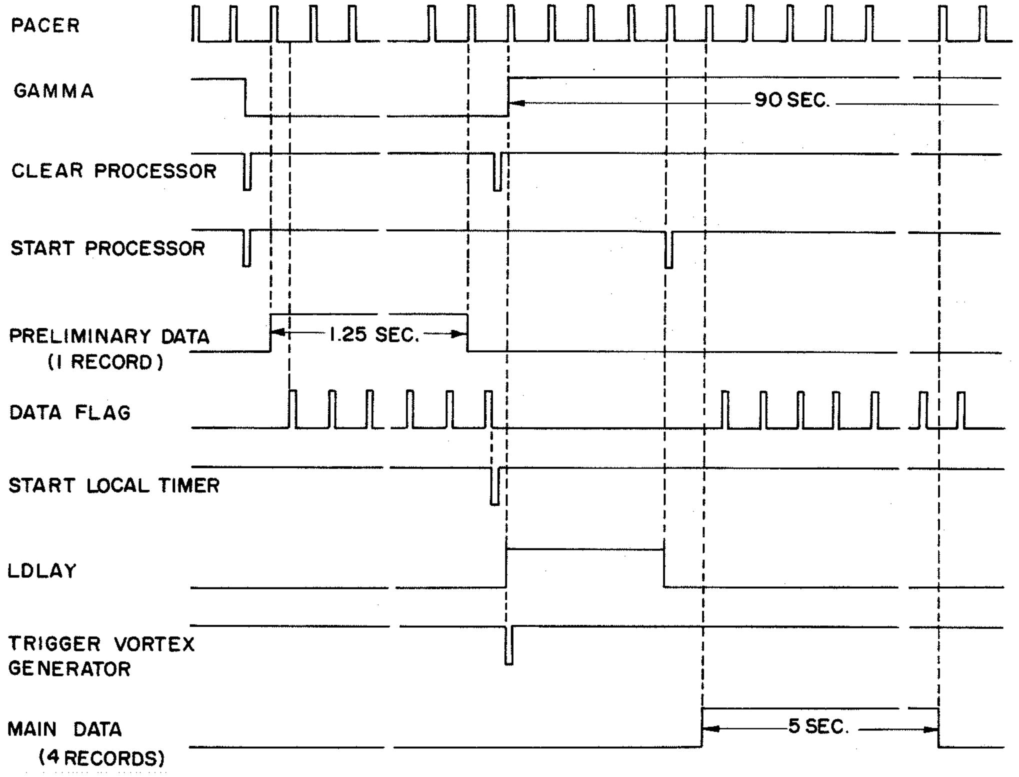

Figure 13

Timing of data acquisition, especially of the preliminary record used to determine grating noise.

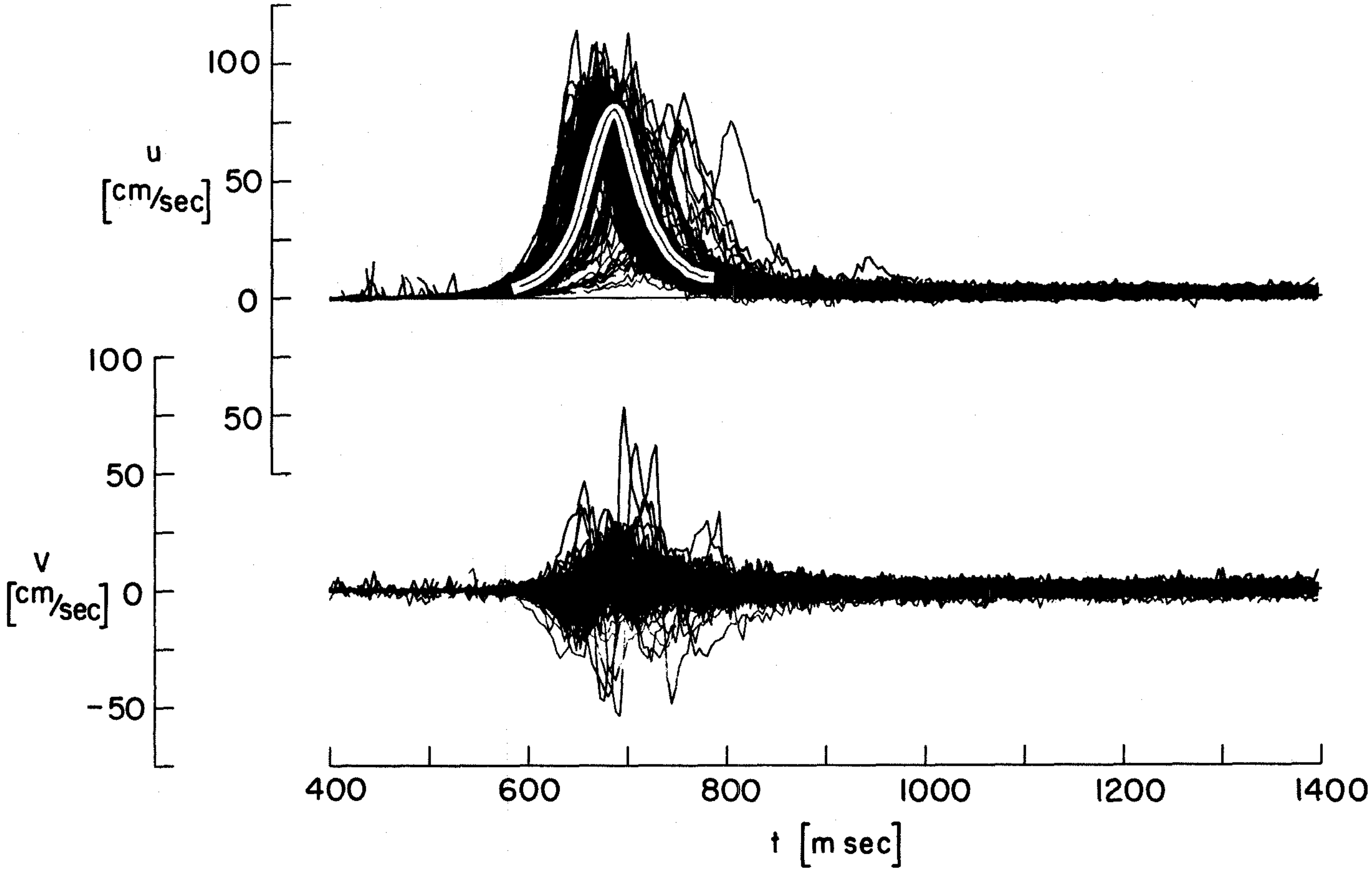

Figure 14

The raw ensemble of 100 velocity traces obtained at $x = 35$ cm, $r = 0$ (file 15). The upper traces are $u(t)$; the lower traces are $v(t)$. The total time is one second. The line superposed on the upper traces is the mean profile $\langle u(t) \rangle$ obtained by smoothing, shifting, and screening.

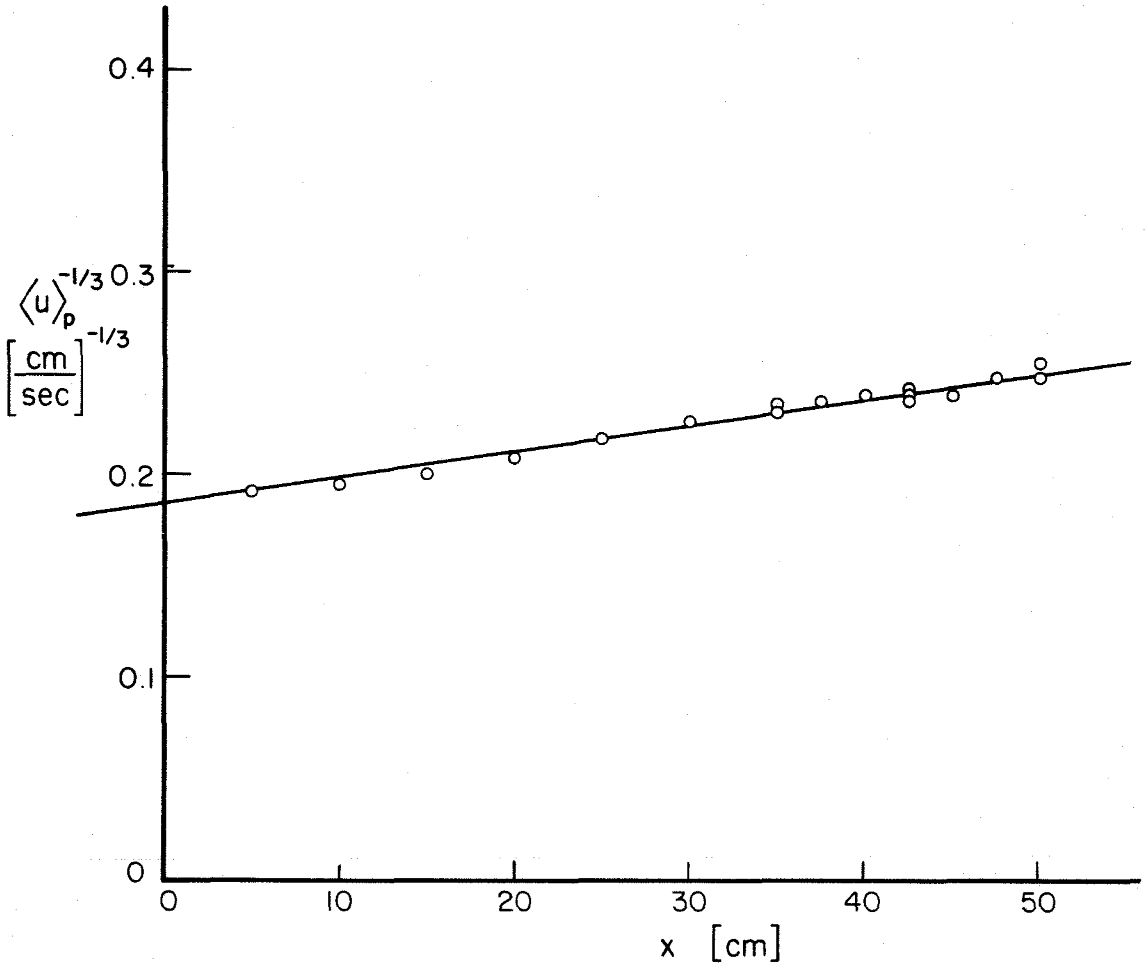

Figure 15

Determination of the apparent origin in space for the vortex ring. The fitted straight line intersects the axis at $x = x_0 = -145$ cm.

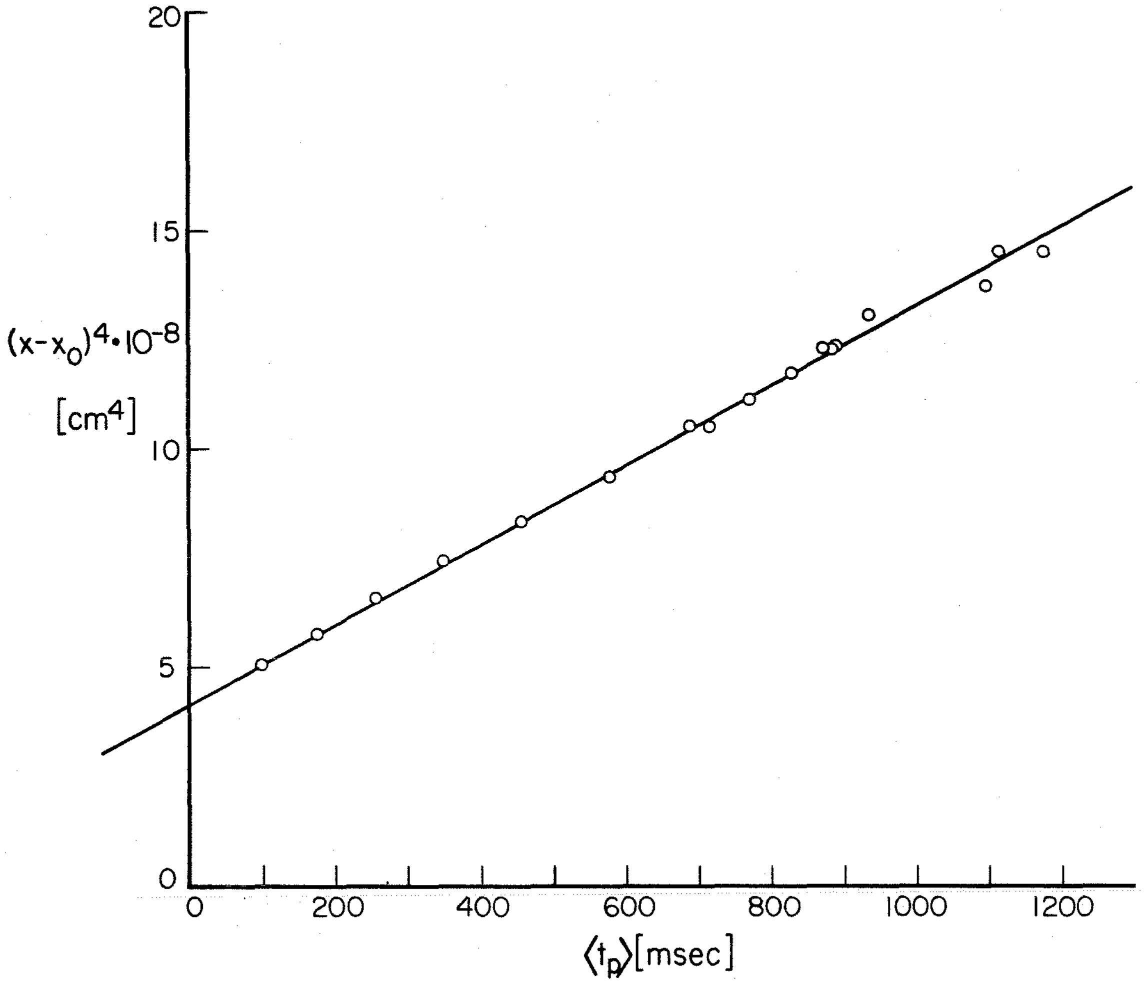

Figure 16

Determination of the apparent origin in time for the vortex ring. The fitted straight line intersects the axis at $t = t_0 = -440$ msec.

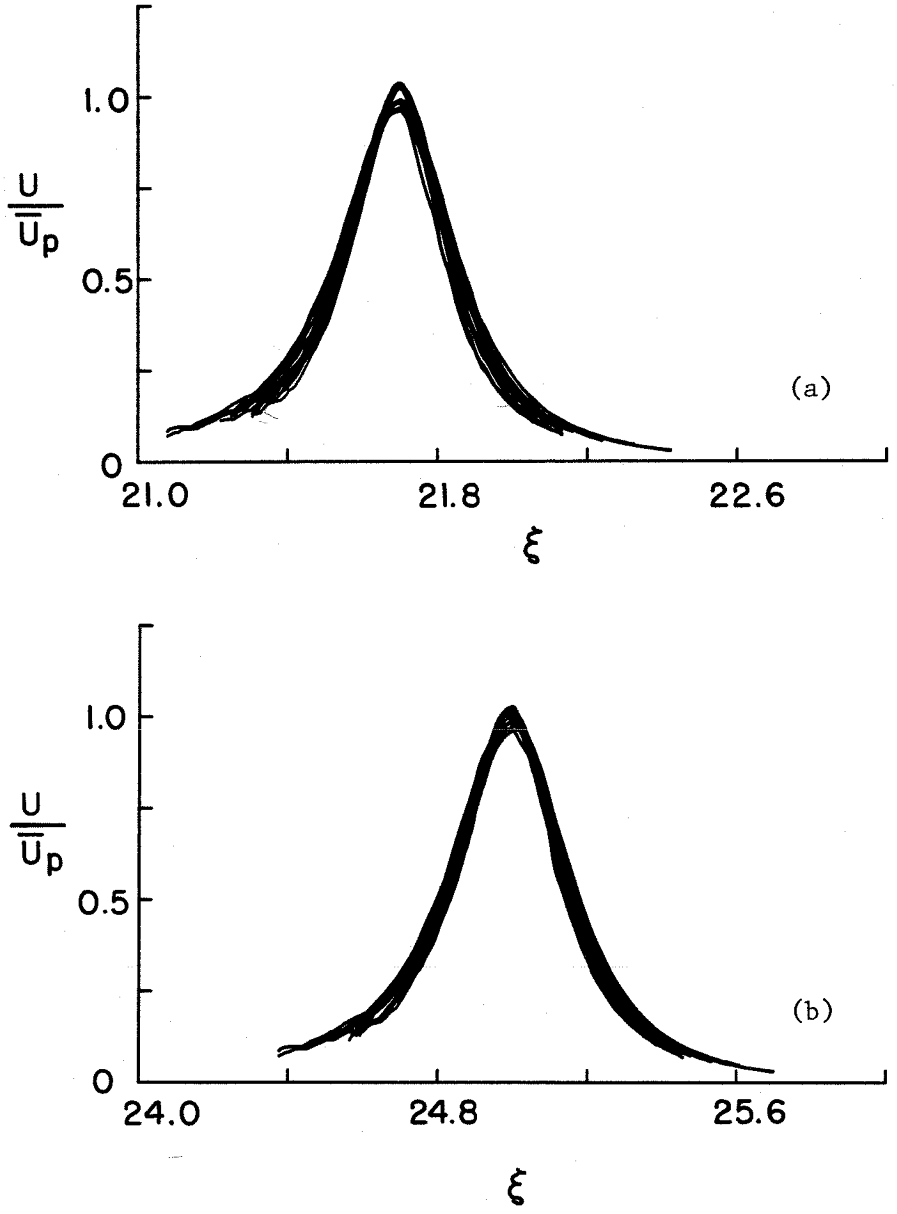

Figure 17

The quality of fit in similarity variables for mean axial-velocity profiles at various values of x. The ordinate is normalized to have a peak value of unity for the overall average profile.

(a) The initial visual fit; $x_0 = -117$ cm, $t_0 = -329$ msec.

(b) The final global fit; $x_0 = -145$ cm, $t_0 = -440$ msec.

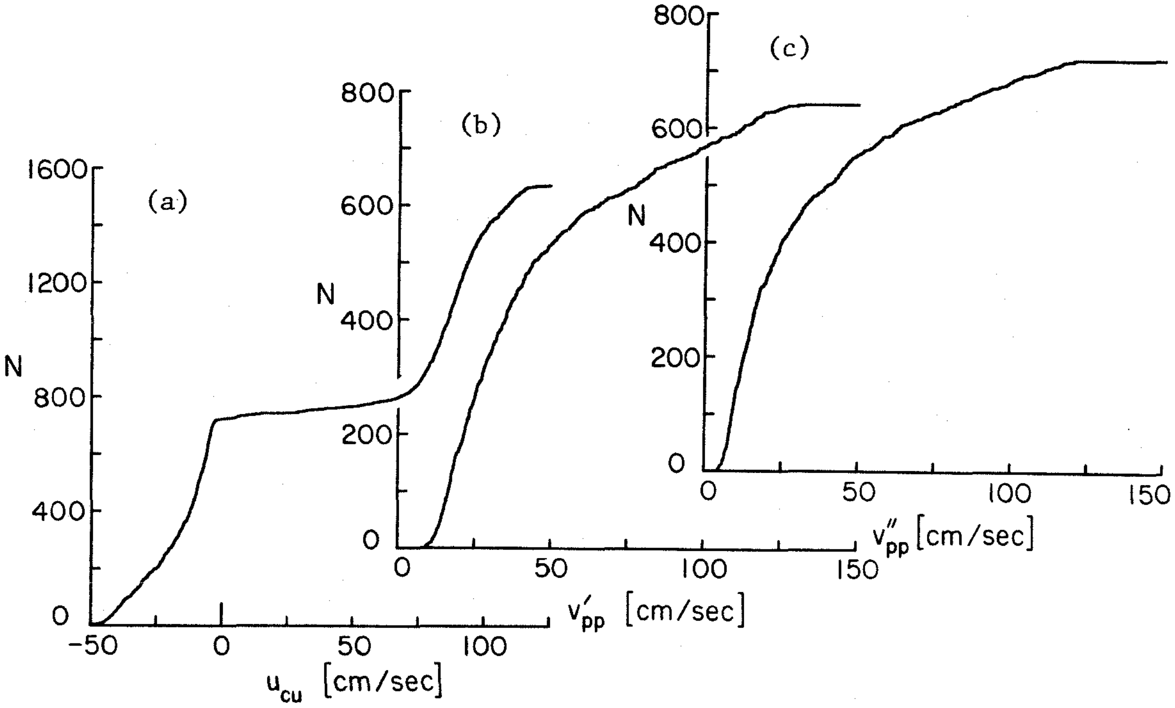

Figure 18

Distribution functions for the data obtained from the radial traverse at $x = 35$ cm.

(a) The cursor velocity u_{cu} for the 1542 vortex rings of the total population.

(b) The peak-to-peak excursion v'_{pp} for the 779 vortex rings of population (i).

(c) The peak-to-peak excursion v''_{pp} for the 722 vortex rings of population (ii)

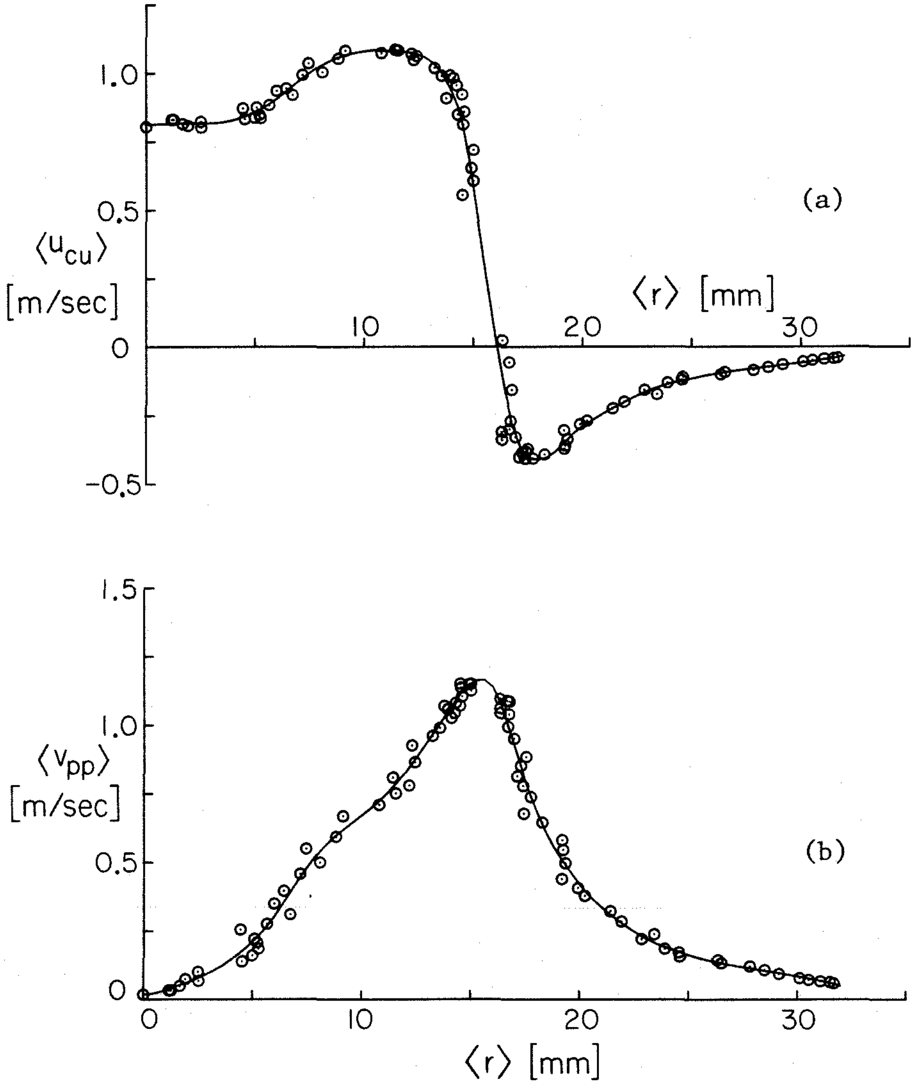

Figure 19

Two characteristic parameters for the set of 80 ensembles generated by the procedure of Section 7.3. The lines are fitted curves.

(a) The parameter $\langle u_{cu} \rangle$ is an extremum in $\langle u \rangle$ lying very nearly in the plane of the vortex core.

(b) The parameter $\langle v_{pp} \rangle$ is the peak-to-peak excursion in $\langle v \rangle$ across the vortex core.

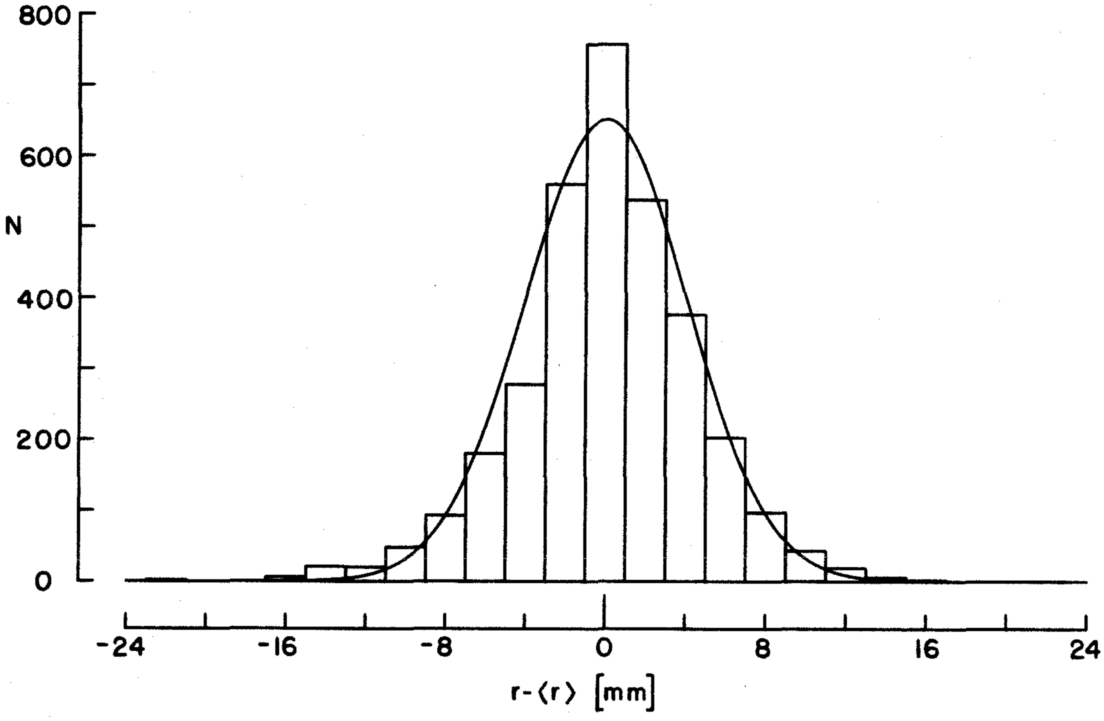

Figure 20

Probability density function showing dispersion in trajectory as observed for 1542 vortex rings. The abscissa is radial position in mm. The scale for the ordinate is arbitrary.

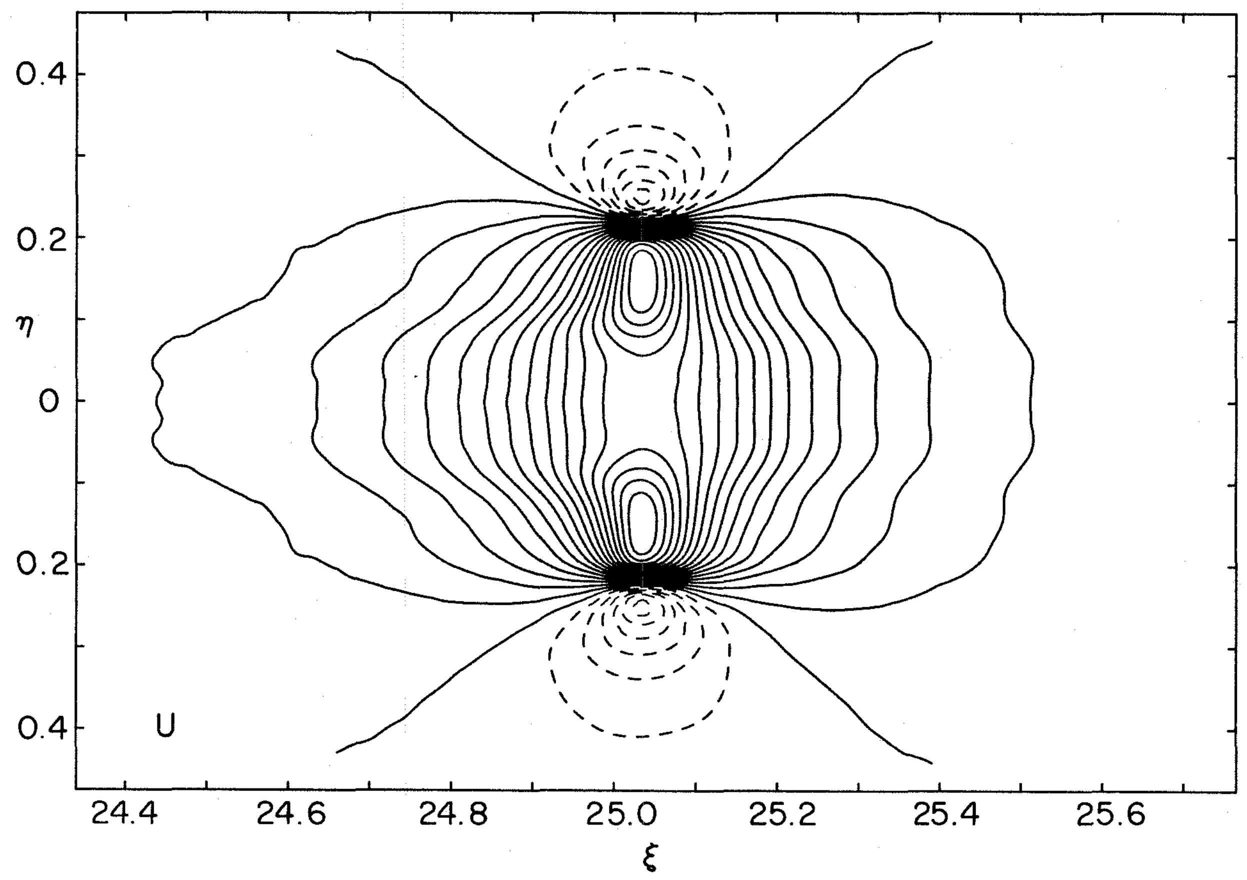

Figure 21

The velocity U in similarity coordinates. The contour interval is 1.0.

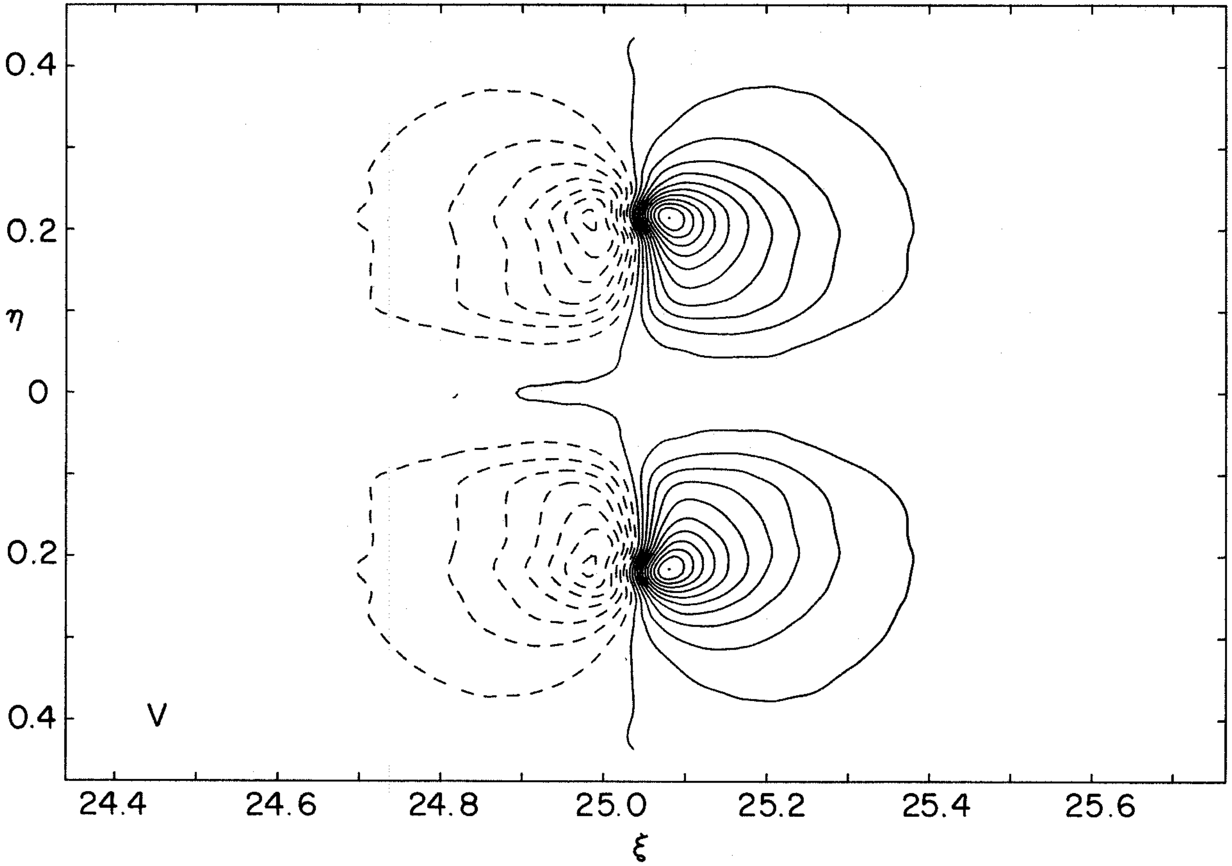

Figure 22

The velocity V in similarity coordinates. The contour interval is 1.0.

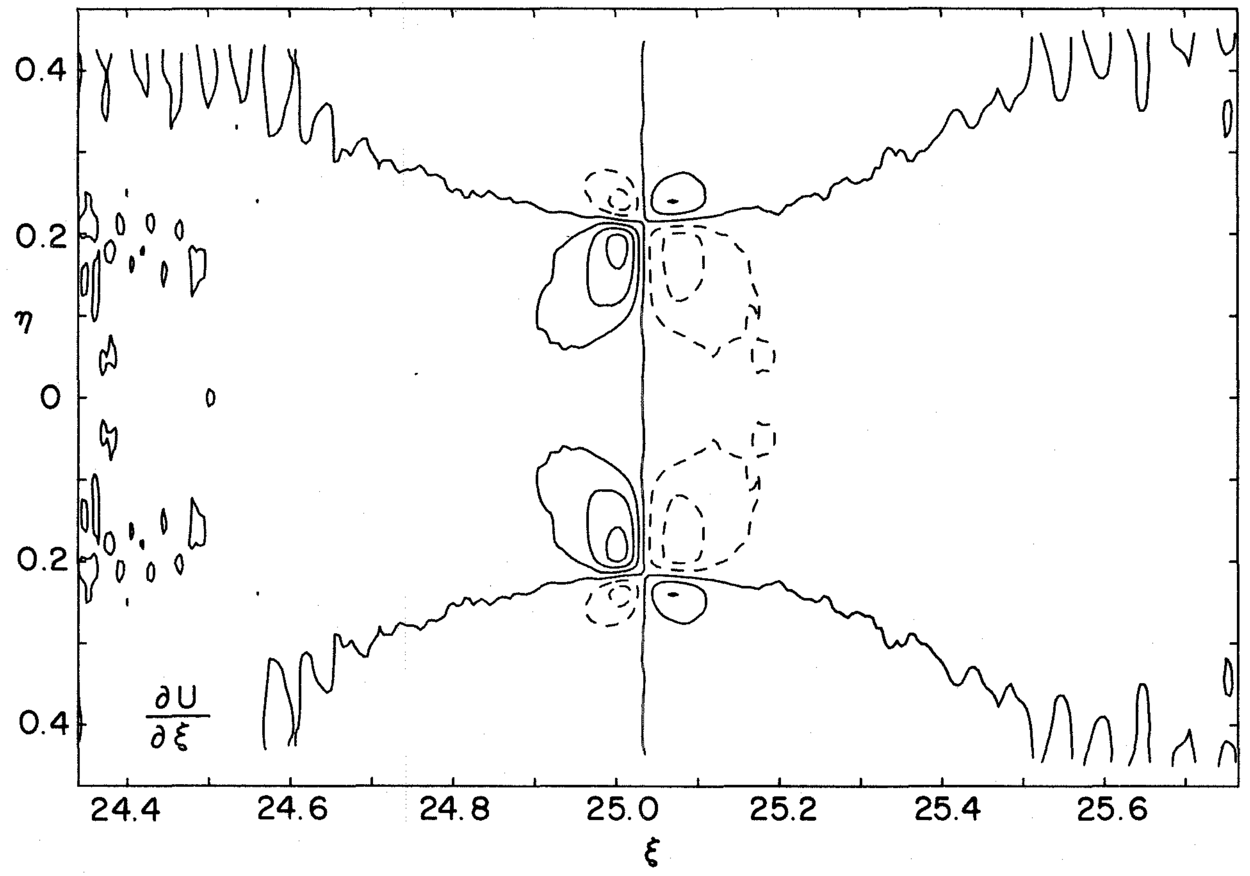

Figure 23

The derivative $\partial U/\partial \xi$ in similarity coordinates. The contour interval is 50.

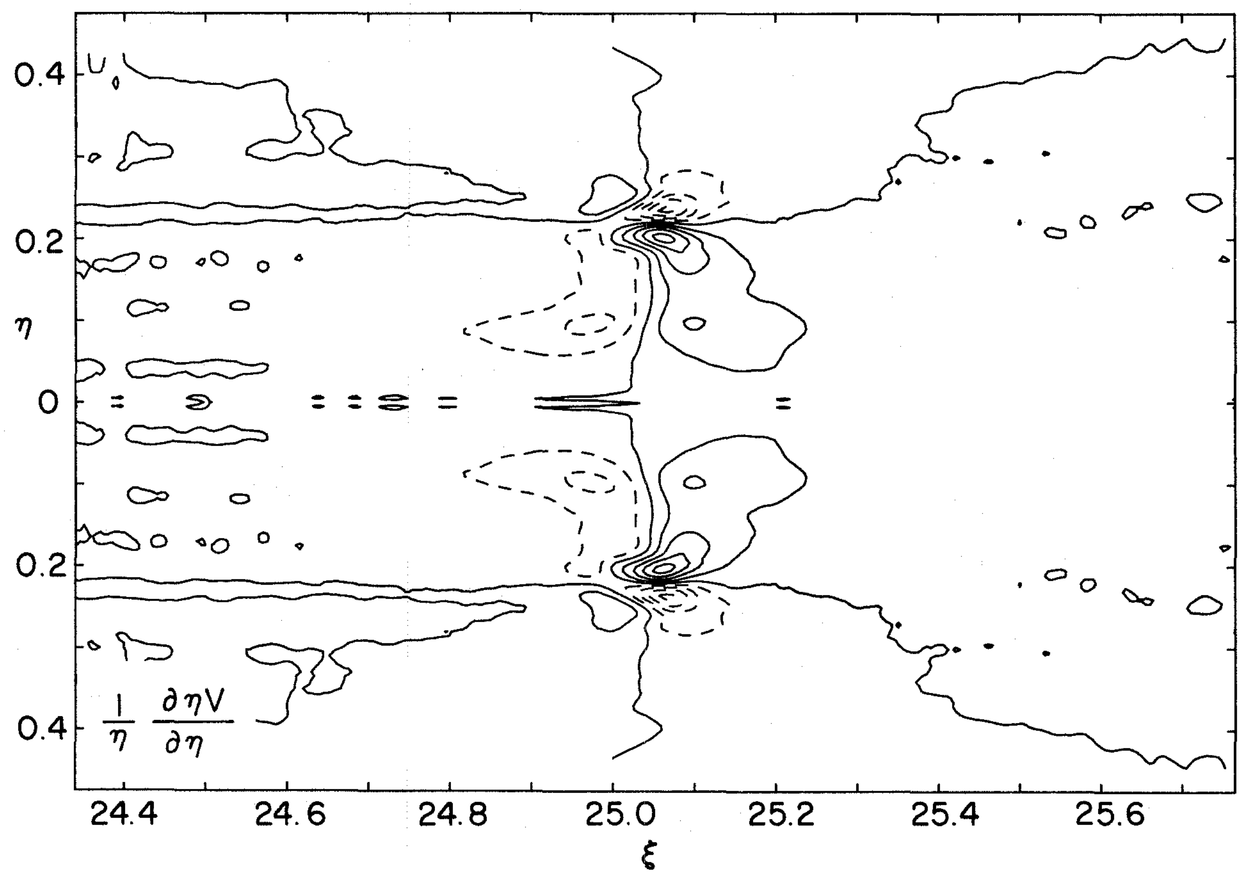

Figure 24

The derivative $\partial \eta V/\eta \partial \eta$ in similarity coordinates. The contour interval is 50.

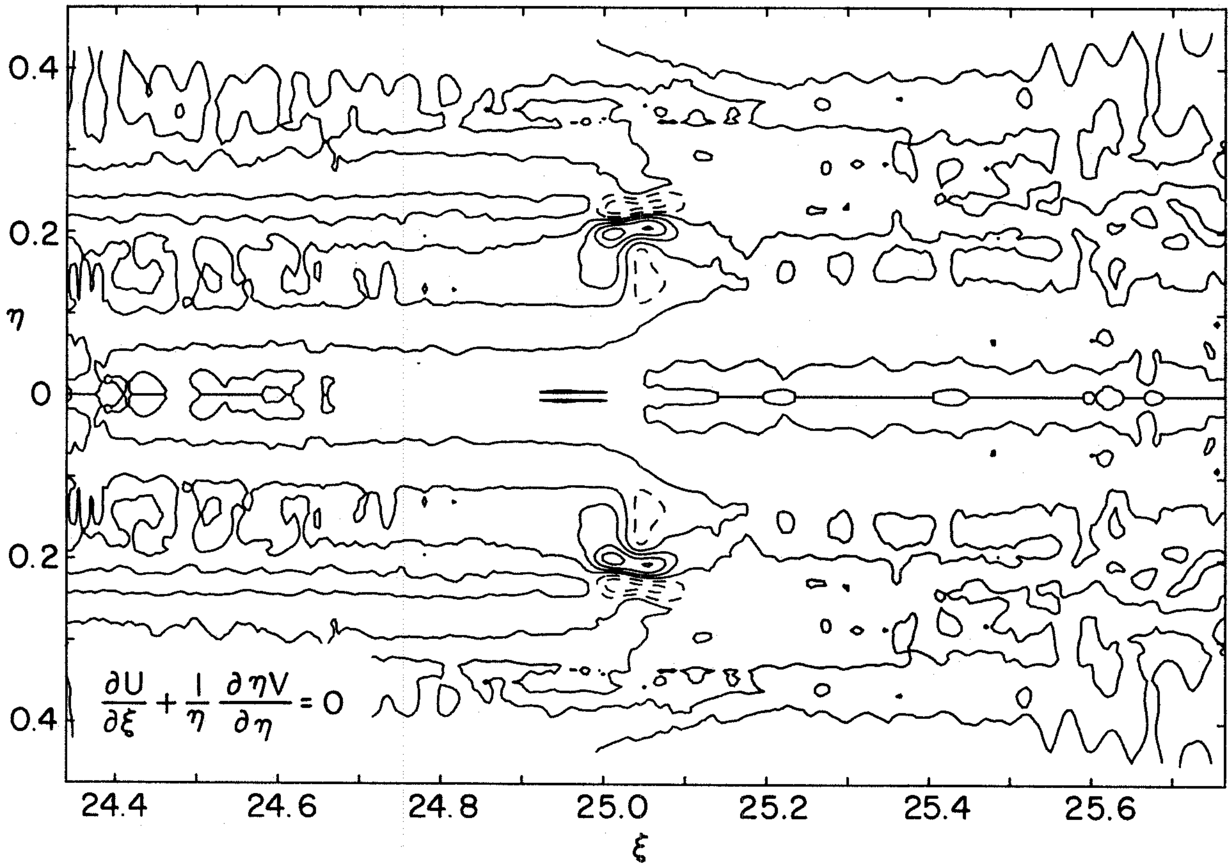

Figure 25

The sum $\partial U/\partial \xi + \partial \eta V/\eta \partial \eta$ (nominally zero) in similarity coordinates. The contour interval is 50.

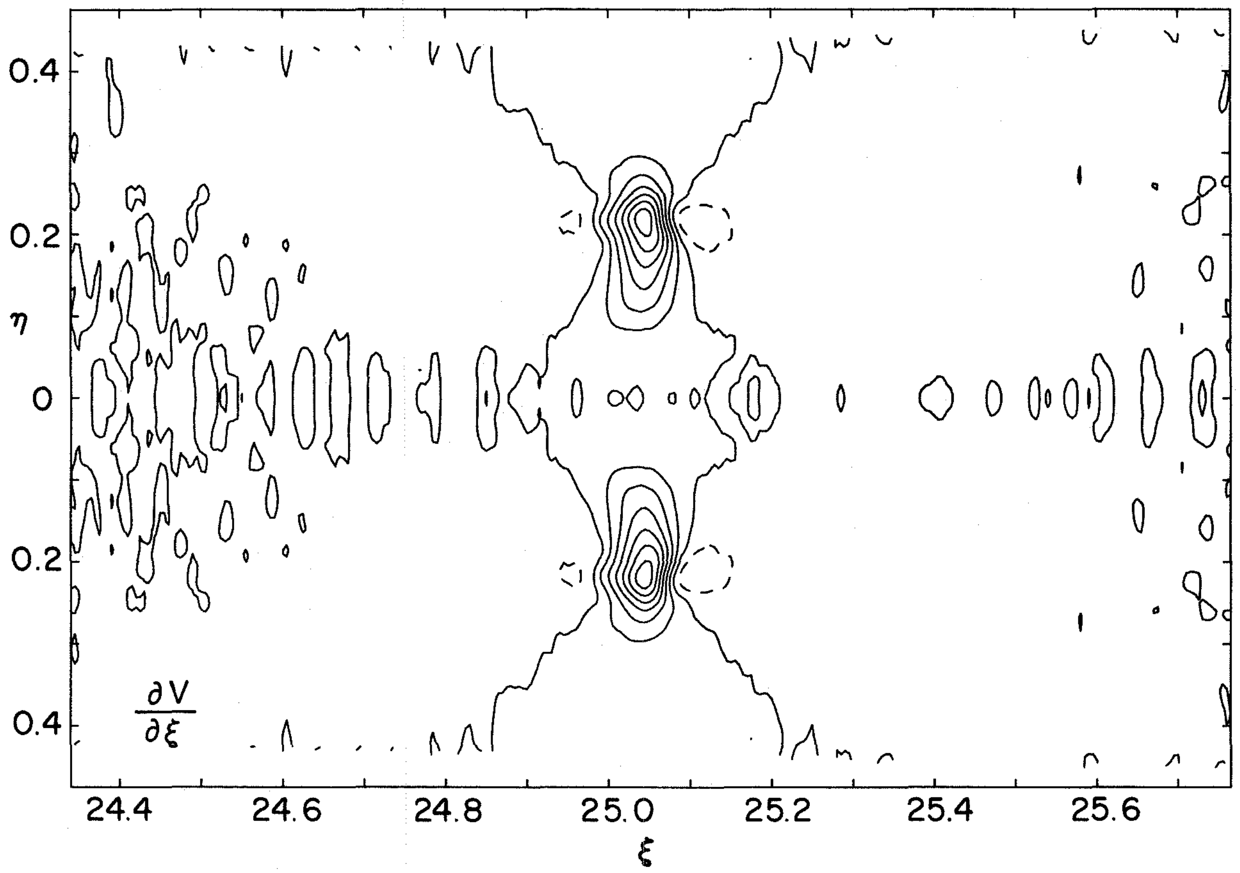

Figure 26

The derivative $\partial V/\partial \xi$ in similarity coordinates. The contour interval is 50.

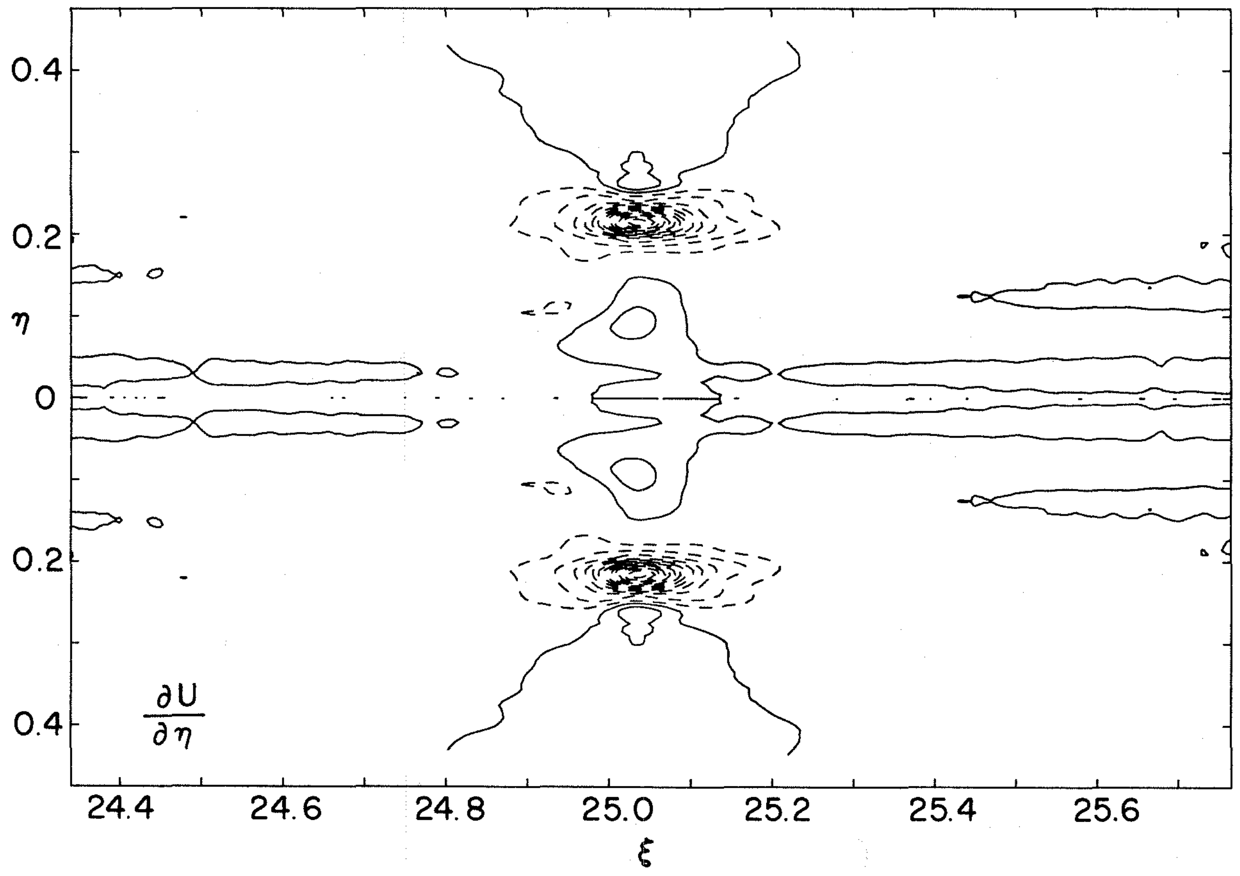

Figure 27

The derivative $\partial U/\partial \eta$ in similarity coordinates. The contour interval is 50.

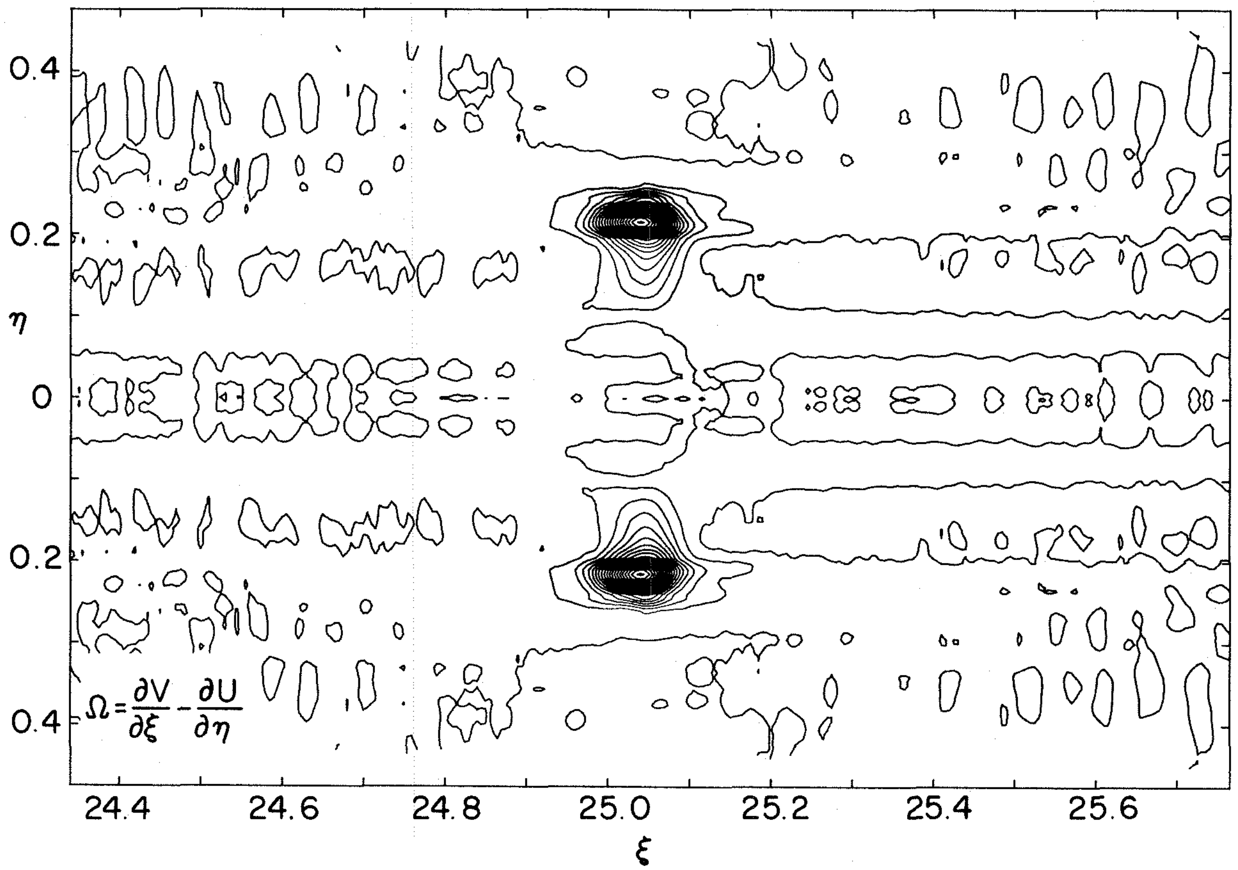

Figure 28

The vorticity Ω in similarity coordinates. The contour interval is 50.

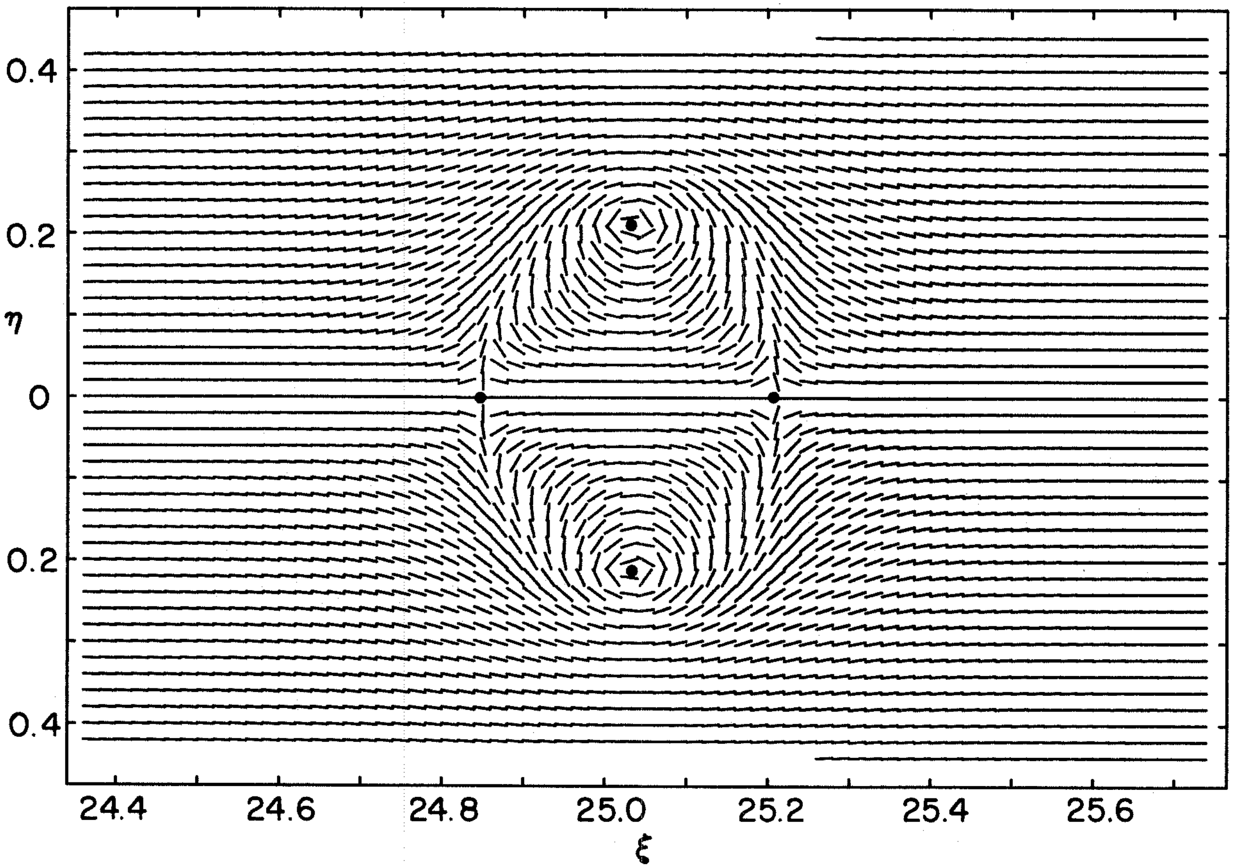

Figure 29

The slopes of the particle paths in similarity coordinates. The vortex ring is moving from left to right. The critical points are shown by filled circles.

Figure 30

A photograph of vortex interactions. Eight successive vortex rings are formed by pulses of 20-msec duration at 85-msec intervals. The orifice diameter is 2.54 cm and the discharge velocity is approximately 80 cm/sec.

TABLES

Table 1. Visual fit; see Fig. 17(a).

```
T0=-329.0 MSEC    X0=-117.0 CM

FILE   TP     U/U*     DT    EPSLNV    EPSLNU     XI1      XI2

 5.    443    .983    -11    .0105     .0490    21.079   22.422

 6.    443    .984    -12    .0081     .0391    21.079   22.422

 7.    558    .970    -19    .0086     .0320    21.154   22.322

 8.    685    .962    -27    .0120     .0349    21.219   22.239

15.    685    .993      0    .0091     .0287    21.219   22.239

 9.    753    .983    -12    .0092     .0227    21.247   22.203

10.    825    .990      0    .0060     .0099    21.274   22.170

11.    900   1.032     14    .0186     .0215    21.299   22.139

42.    900   1.031     35    .0069     .0314    21.299   22.139

61.    900    .985     19    .0150     .0510    21.299   22.139

12.    979   1.039     50    .0072     .0327    21.322   22.112

13.   1062   1.024    -28    .0109     .0220    21.344   22.086

14.   1149    .987    -18    .0078     .0292    21.364   22.062

33.   1149   1.038     37    .0061     .0545    21.364   22.062

RMS EPSLNV= .0103    RMS EPSLNU= .0349

RMS (1.-U/U*)= .0257    RMS DT= 24.813
```

Column (1) File number.
(2) TP = $\langle t_p \rangle$ in text; arrival time for peak velocity, msec.
(3) U/U* = $U_p/\overline{U}_p$ in text; ratio of peak values.
(4) DT = time shift for optimum fit, msec.
(5) EPSLNV = ε in text; rms deviation in $(V - \overline{V})/\overline{U}_p$.
(6) EPSLNU = ε in text; rms deviation in $(U - \overline{U})/\overline{U}_p$.
(7),(8) XI1, XI2 = start and stop points for $U(\xi)$ in units of ξ.

Table 2. Global fit; see Fig. 17(b).

```
T0=-440.0 MSEC   X0=-145.0 CM

FILE   TP     U/U*     DT    EPSLNV    EPSLNU     XI1      XI2

 5.    461   1.010      6    .0099     .0380    24.375   25.699

 6.    461   1.012      5    .0084     .0286    24.375   25.699

 7.    572    .985     -5    .0088     .0232    24.440   25.617

 8.    690    .966    -22    .0109     .0332    24.511   25.566

15.    695    .999      9    .0089     .0062    24.486   25.535

 9.    757    .984     -8    .0094     .0200    24.521   25.515

10.    824    .987     -1    .0061     .0104    24.545   25.486

11.    896   1.025     10    .0178     .0133    24.560   25.450

42.    895   1.026     30    .0070     .0286    24.564   25.455

61.    891    .979     10    .0157     .0312    24.581   25.475

12.    967   1.030     38    .0071     .0256    24.587   25.432

13.   1044   1.008    -46    .0108     .0180    24.601   25.402

14.   1121    .968    -46    .0075     .0273    24.627   25.389

33.   1120   1.022      8    .0059     .0435    24.628   25.390

RMS EPSLNV= .0102    RMS EPSLNU= .0268

RMS (1.-U/U*)= .0212    RMS DT= 23.661
```

Column (1) File number.
(2) TP = $<t_p>$ in text; arrival time for peak velocity, msec.
(3) U/U* = $U_p/\overline{U}_p$ in text; ratio of peak values.
(4) DT = time shift for optimum fit, msec.
(5) EPSLNV = ε in text; rms deviation in $(V - \overline{V})/\overline{U}_p$.
(6) EPSLNU = ε in text; rms deviation in $(U - \overline{U})/\overline{U}_p$.
(7),(8) XI1, XI2 = start and stop points for $U(\xi)$ in units of ξ.